UC Berkeley
UC Berkeley Electronic Theses and Dissertations

Title

Transient Thermal, Hydraulic, and Mechanical Analysis of a Counter Flow Offset Strip Fin Intermediate Heat Exchanger using an Effective Porous Media Approach

Permalink

https://escholarship.org/uc/item/3wj6r88c

Author

Urquiza, Eugenio

Publication Date

2009

Peer reviewed|Thesis/dissertation

eScholarship.org
Powered by the California Digital Library
University of California

Transient Thermal, Hydraulic, and Mechanical Analysis of a Counter Flow Offset Strip Fin Intermediate Heat Exchanger using an Effective Porous Media Approach

by

Eugenio Urquiza

B.S. (Texas A&M University) 2002

M.S. (University of California, Berkeley) 2006

A dissertation submitted in partial satisfaction
of the requirements for the degree of

Doctor of Philosophy

in

Engineering-Mechanical Engineering

in the

Graduate Division

of the

University of California, Berkeley

Committee in Charge

Professor Per F. Peterson, Co-chair
Professor Ralph Greif, Co-chair
Professor Van P. Carey
Professor Tadeusz Patzek

Fall 2009

Transient Thermal, Hydraulic, and Mechanical Analysis
of a Counter Flow Offset Strip Fin Intermediate Heat Exchanger
using an Effective Porous Media Approach

© 2009

by Eugenio Urquiza

Abstract

Transient Thermal, Hydraulic, and Mechanical Stress Analysis
of a Counter Flow Offset Strip Fin Intermediate Heat Exchanger
using an Effective Porous Media Approach

by

Eugenio Urquiza

Doctor of Philosophy in Engineering-Mechanical Engineering

University of California, Berkeley

Professor Per F. Peterson, Co-chair

Professor Ralph Greif, Co-chair

This work presents a comprehensive thermal hydraulic analysis of a compact heat exchanger using offset strip fins. The thermal hydraulics analysis in this work is followed by a finite element analysis (FEA) to predict the mechanical stresses experienced by an intermediate heat exchanger (IHX) during steady-state operation and selected flow transients. In particular, the scenario analyzed involves a gas-to-liquid IHX operating between high pressure helium and liquid or molten salt.

In order to estimate the stresses in compact heat exchangers a comprehensive thermal and hydraulic analysis is needed. Compact heat exchangers require very small flow

channels and fins to achieve high heat transfer rates and thermal effectiveness. However, studying such small features computationally contributes little to the understanding of component level phenomena and requires prohibitive computational effort using computational fluid dynamics (CFD).

To address this issue, the analysis developed here uses an effective porous media (EPM) approach; this greatly reduces the computation time and produces results with the appropriate resolution [1]. This EPM fluid dynamics and heat transfer computational code has been named the Compact Heat Exchanger Explicit Thermal and Hydraulics (CHEETAH) code. CHEETAH solves for the two-dimensional steady-state and transient temperature and flow distributions in the IHX including the complicating effects of temperature-dependent fluid thermo-physical properties. Temperature- and pressure-dependent fluid properties are evaluated by CHEETAH and the thermal effectiveness of the IHX is also calculated.

Furthermore, the temperature distribution can then be imported into a finite element analysis (FEA) code for mechanical stress analysis using the EPM methods developed earlier by the University of California, Berkeley, for global and local stress analysis [2]. These simulation tools will also allow the heat exchanger design to be improved through an iterative design process which will lead to a design with a reduced pressure drop, increased thermal effectiveness, and improved mechanical performance as it relates to creep deformation and transient thermal stresses.

To my parents, Guillermo and Margarita.

Table of Contents

Chapter 2 · Partitioning, Discretization, and Numerical Method 35

Chapter 3 · Thermal Hydraulic Results 54

Nomenclature

a'	surface area density, m^2/m^3
c	an empirical constant
C_1	hydraulic constant related to the offset strip fin geometry
c_p	the specific heat, $J/(kg\mathrm{K})$
CFL	Courant – Friedrichs – Levy Number, dimensionless
Co	Colburn Factor, $St\,\mathrm{Pr}^{2/3}$ or $Nu/(\mathrm{Re}\,\mathrm{Pr}^{1/3})$
D	diameter, m
D_h	hydraulic diameter, m
f_f	Fanning friction factor, dimensionless
Fo	Fourier Number, dimensionless
g	acceleration due to gravity, m/s^2
Gz	Graetz number, dimensionless
h	fin height, m
h	convective heat transfer coefficient, $w/(m^2\mathrm{K})$
j	Colburn factor, dimensionless
k	effective conductivity, $w/(m\mathrm{K})$
$\mathrm{k_f}$	conductivity of the fluid, $w/(m\mathrm{K})$
k	effective permeability, m^2
l	length of the fins in the offset strip fin arrangement, m
L	length of flow path, m
m	mass, kg
$\dot{m}$	mass flow rate, kg/s
n	iteration number (time)
Nu	Nusselt number, dimensionless
P	pressure, Pa
Pe	Peclet number, dimensionless
Pr	Prandtl number, dimensionless
Re	Reynolds number, dimensionless
St	Stanton number, dimensionless
t	thickness of the fins in the offset strip fin arrangement, m
T	temperature, K
$\bar{u}$	average velocity, m/s
u	velocity in the *x* direction, m/s
u_D	Darcy velocity in the *x* direction, m/s
u_{int}	interstitial velocity in the *x* direction, m/s
x	coordinate in the flow direction
w	velocity in the *z* direction, m/s
w_{int}	interstitial velocity in the *z* direction, m/s
z	coordinate in the cross-flow direction

Subscripts

c	constant
f	fluid
fc	cold fluid
fcs	between cold fluid and solid
fcx	cold fluid *x* direction
fcz	cold fluid *z* direction
fh	hot fluid
fhs	between hot fluid and solid
fhx	hot fluid *x* direction
fhz	hot fluid *z* direction
s	solid
sfc	between solid and cold fluid
x	*x* direction
z	*z* direction

Superscript

*	denotes non-dimensional

Greek Symbols

α	thermal diffusivity
Δ	discrete change
ϕ	phase fraction
Φ	flow potential, Pa
μ	dynamic viscosity, Pa*s
ρ	density, kg/m^3

Index Variables

i	index in the x direction (flow direction)
j	index in the y direction
k	index in the z direction (cross-flow direction)

Abbreviations

AHTR	Advanced High-Temperature Reactor
CFD	Computational Fluid Dynamics
CHEETAH	Compact Heat Exchanger Thermal and Hydraulic code
EPM	Effective Porous Media
FDM	Finite Difference Method
FEA	Finite Element Analysis
FVA	Finite Volume Analysis
IHX	Intermediate Heat Exchanger
NTU	Number of Transfer Units
OSF	Offset Strip Fin
PBMR	Pebble Bed Modular Reactor

List of Figures

Chapter 1 · Heat Exchanger Layout, Effective Porous Media (EPM) Approach, and Conservation Equations 1

Chapter 2 · Partitioning, Discretization, and Numerical Method 35

Chapter 3 · Thermal Hydraulic Results 54

Chapter 4 · Verification of Numerical Method 82

List of Tables

Preface

Thermal hydraulic analysis of compact heat exchangers is a well studied field. Seminal works in this area include those by Kays, London, and Shah. In the preface to their seminal work Compact Heat Exchangers, Kays and London briefly note the modern history of the need for rational optimization of heat exchangers. They explain that for a long period of time the only basic heat transfer and flow-friction design data available was that for circular tubes. As automobiles, ships, and aircraft developed, so did the need for heat transfer surfaces that could outperform what could be done with circular tubes. But in order to intelligently design and specify heat exchangers with more complex and superior heat transfer surfaces, a better understanding of existing surfaces was required.

The authors write that in the mid-to-late 1940's the U.S. Navy Bureau of Ships and Aeronautics, and later the Atomic Energy Commission, funded a research and testing program to produce and publish data on the performance of many then-existing heat exchanger surfaces. This work came in collaboration with heat exchanger manufacturers who donated cores to their research and testing program. The manufacturers in turn benefited from the published data and used it to improve the design of their hardware. Similarly, increased computational capability has allowed the current generation of engineers to characterize heat exchangers before they are built, thereby accelerating the iterative process of design, build, test, learn, and improve. The Compact Heat Exchanger Explicit Thermal and Hydraulics (CHEETAH) code follows in this tradition by contributing a research tool that allows the designer to modify and improve the manifold design of the heat exchanger in order to produce a flow distribution with increased uniformity before the heat exchanger is built. The CHEETAH code is a research tool that, when used in conjunction with a finite element analysis (FEA) code, allows a designer to test the strength of a heat exchanger so that it can be designed for higher temperatures, be built with less material, and take plants to higher efficiency than before. After all, a fractional improvement on the power plant scale can have a very meaningful impact.

Introduction

Currently, Earth faces potentially severe environmental consequences associated with the waste resulting from fossil fuel combustion. These energy sources fueled the industrial revolution and an era of innovation; it is now critical that humanity develop new sources of energy that avoid the atmospheric emissions of fossil sources. While there are many cleaner alternatives to fossil fuels, very few of them can provide power in a reliable and cost-effective fashion. The problem is partially related to energy flux. Some of the most discussed alternative energy sources are wind and solar. These sources already provide a small portion of our energy (in the United States, less than 1% total in 2009) and promise to expand significantly. However, both wind and solar power are not only intermittent, but also relatively diffuse when compared to what is obtained from fossil fuels. Geothermal, hydropower, and nuclear power address this issue, as these are alternatives that could replace the base load electricity that is currently supplied by coal and natural gas without operational atmospheric pollution.

The transportation sector, on the other hand, requires portable energy storage. This is currently provided by fuels such as diesel, gasoline, methane, ethanol, and kerosene. While many engineering challenges remain, hydrogen and biofuels (such as ethanol and bio-diesel) are both being explored as possible future replacements for petroleum-based liquid fuels. However, it is critical that any alternatives come from sources and processes that reduce environmental externalities relative to current petroleum-based alternatives.

Additionally, battery technology is beginning to compete with the liquid fuels in the transportation sector and may revolutionize the energy sector by allowing electric utilities to compete with petroleum companies as energy providers for modern transportation.

One possible method to produce hydrogen is to chemically separate hydrogen from oxygen in water via the sulfur iodine cycle. This would require an input of heat from a very high temperature source (between 800°C and 1000°C) to be transferred to the thermo-chemical plant. Alternatively, this heat could be used to produce electricity at high thermodynamic efficiency. One option would be to implement a multiple reheat helium Brayton cycle, which can provide upwards of 50% thermodynamic efficiency and could be significantly cheaper than comparable steam turbine cycles.

The source of this heat could be a high-temperature nuclear reactor, such as the Advanced High-Temperature Reactor (AHTR) being researched at the University of California, Berkeley, or a reactor such as the helium-cooled Pebble Bed Modular Reactor (PBMR) currently under construction in South Africa. Liquid salts and inert gases such as helium are being proposed as possible reactor coolants for various high-temperature reactor designs. One particularly interesting design involves using an intermediate heat transfer loop to transfer thermal energy at high temperature from a reactor to a power plant or thermo-chemical plant located a short distance (<1km) away as illustrated below.

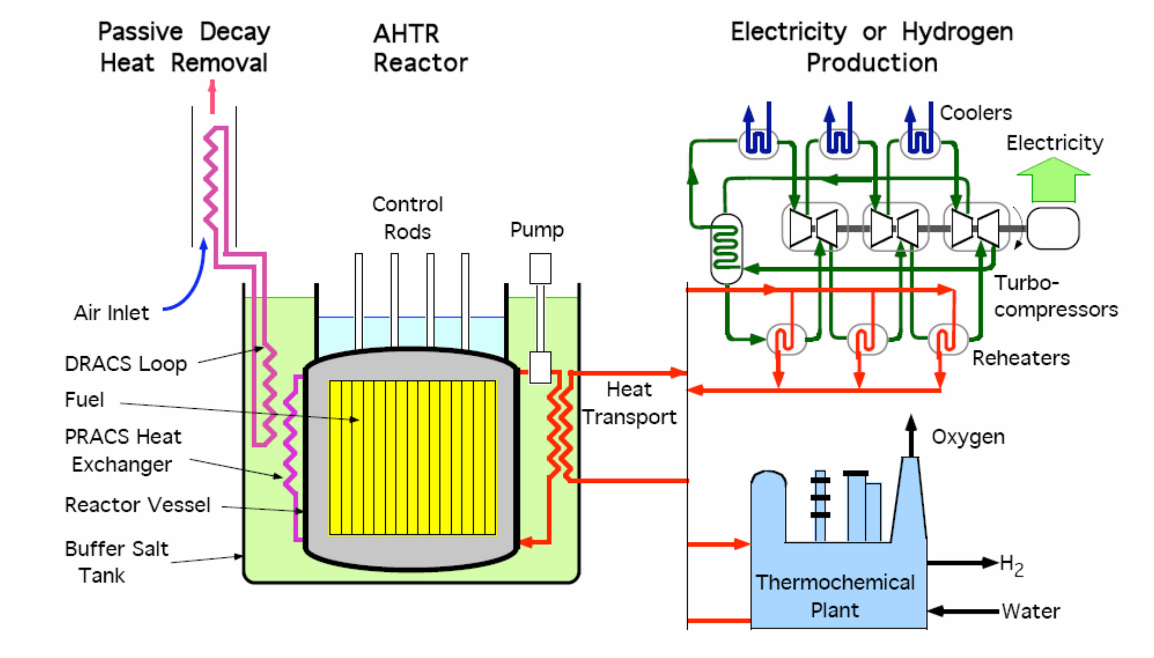

Figure 0-1: Schematic of the Advanced High-Temperature Reactor joined by an intermediate heat transfer loop (shown in red) to an adjoining power or process plant. [Image: Prof. Per F. Peterson - UC Berkeley]

An intermediate heat exchanger (IHX) is required to transfer thermal energy from high-temperature and high-pressure primary helium coolant to an intermediate loop. The intermediate fluid would then transfer the thermal energy to a power plant or hydrogen production process via another IHX near the application. In this analysis, a liquid salt is analyzed as the intermediate coolant. This intermediate liquid, or molten, salt loop acts as a buffer between the nuclear reactor and the hydrogen or chemical plant. This is intrinsically beneficial for overall system safety, because by increasing the thermal inertia in the system the intermediate loop also helps reduce the volatility of temperature transients.

The elevated temperatures in the intermediate loop require the implementation of a highly compact heat exchanger that retains its strength at high temperatures. Under these conditions, plate-type heat exchangers with small flow channels are major candidates because they can achieve high power densities with small amounts of material, and can be fabricated using a diffusion bonding process so that the entire heat exchanger has the strength of the base material [3]. Such a heat exchanger manufactured by Heatric is shown in Figure 0-2.

Figure 0-2: Photo of a cut-away model of a typical Heatric plate-type compact heat exchanger showing multiple inlet and outlet manifolds and slices across various plates and flow channels.

Although these types of heat exchangers can achieve high effectiveness, they can also be susceptible to very large stresses during thermal transients (for instance, when the flow of one fluid is interrupted). Accurate multi-scale analysis of the thermo-mechanical performance of these devices is needed to evaluate the reliability and safety of the heat exchanger. Therefore, the thermal hydraulics phenomena in the heat exchanger's complex geometry must be analyzed at the component scale, or plate scale, during steady-state operation as well as during flow transients. The work presented bridges between thermal, hydraulic, and mechanical phenomena at the plate and fin scales.

For the purpose of analyzing the fluid flow and temperature distributions at the plate scale, the Compact Heat Exchanger Explicit Thermal and Hydraulics (CHEETAH) code was formulated. Applying the resulting temperature and flow distributions from CHEETAH, which includes the complicating effects of temperature-dependent thermo-physical properties, allows for thermal optimization of the heat exchanger design. Furthermore, the temperature distribution of the IHX will serve as a starting point for the mechanical finite element analysis (FEA) on the plate scale using effective (volume-averaged) mechanical properties. With these principal (x, y, and z directional) component-scale stresses, it is possible to resolve the local stress state at various locations in the IHX plate. This stress state can then be imposed on unit cells representing the detailed local geometry [2]. Results from the fin- and component-scale stresses are shown in Figure 0-3. After recreating the stress state on the unit cells, the peak (Von Mises) stresses on detailed fin scale geometry can be analyzed in the context of failure criteria.

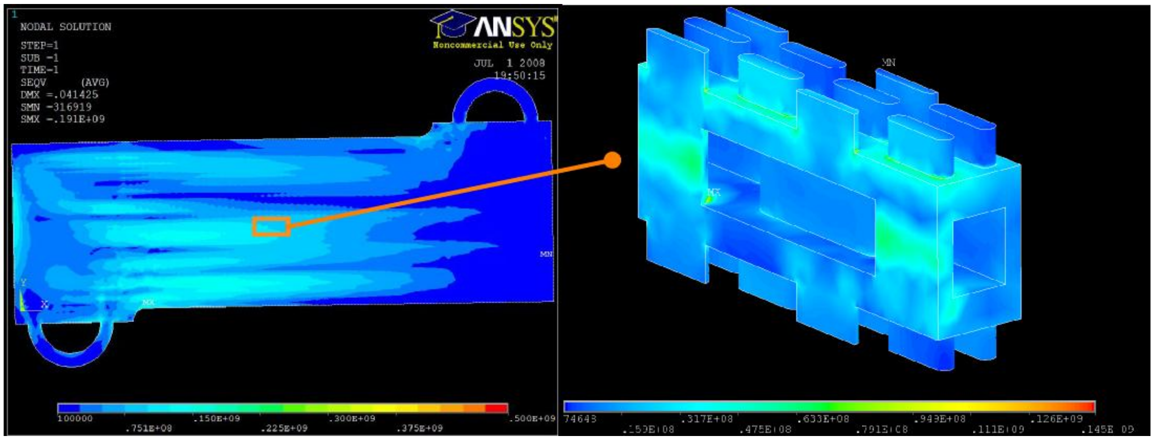

Figure 0-3: CHEETAH provides thermal hydraulic data that enables the analysis of component-level (plate-scale) thermal stresses on the composite plate of the IHX (left) and corresponding local (fin-scale) stresses shown on a unit cell (right).

The following chapters will cover various aspects of the thermal, hydraulic, and mechanical analysis of a gas-to-liquid offset strip fin heat exchanger for high-temperature applications. In particular, the work covers the theory used in the thermal hydraulic model, the implementation of the theory in a finite volume analysis (FVA), evaluation of mechanical integrity, results, and conclusions. Lastly, after careful thermal, hydraulic, and mechanical analysis, recommendations are given regarding the design and evaluation of offset strip fin heat exchangers in high-temperature applications.

Acknowledgements

I would like to acknowledge the support of my advisors, Professors Per F. Peterson and Ralph Greif; your vision and guidance was most essential.

I am grateful for the help of Kenneth Lee for his help in performing many mechanical stress analyses. Analyses and documentation passed on by David Huang and Dr. Hai Hua Zhao were also instrumental in this work.

To my wife, Columba, your endless help in editing and formatting the text and also in preparing figures made this daunting process manageable. I will always admire your discipline, patience, and understanding; you helped me focus and finish.

I would like to recognize my brother for his example and my sister for her perseverance and fortitude.

Most of all I would like to thank my parents for your selfless investment in your children. Your love and encouragement were fundamental.

Chapter 1

Heat Exchanger Layout, Effective Porous Media (EPM) Approach, and Conservation Equations

Compact heat exchangers achieve high heat transfer rates by employing advanced internal geometries that increase the heat transfer surface density and create high average convection coefficients. The offset strip fin (OSF) design is one of the most effective in this regard because it creates a new thermal boundary layer on each fin and destroys it in the mixed flow that occurs in its wake. Many OSF heat exchanger designs use brazing to bond surfaces such as fins onto plates and plates onto other plates. In brazing, a material with a lower melting point is used to fill spaces and adhere to parts made of another material with a higher melting temperature. While this process can be employed at low cost it significantly limits the temperature at which the brazed device can operate. For lower temperature heat exchangers such as those used in heating, ventilation, and air conditioning systems this may not be an issue but the lower temperature restriction of the brazing material encumbers the application of this method in high temperature devices. Heat exchangers with brazed joints are rarely used at temperatures over 200°C (473 K).

In high temperature applications diffusion bonded heat exchangers have the intrinsic advantage of being made entirely of refractory alloys and thus are not being limited by a weaker joining material. In diffusion bonding the refractory alloy plates are assembled and inserted into a high temperature environment while a load is applied for an extended period of time during which the plates fuse together. The bonded plates that make up the heat exchanger then behave as one large cohesive part rather than as a joined assembly.

The thermal, hydraulic, and mechanical modeling of a large heat exchanger with a complex internal geometry is challenging because important fluid dynamics, heat transfer, and mechanical stress arise fundamentally on two scales. The thermal and hydraulic boundary layers being created and destroyed in the fins are complex at a small scale. The plate's repetitive geometry of many small offset fins also creates intense mixing which homogenizes the flow and thermal fields. This homogenizing effect facilitates evaluation of the thermal hydraulic results on a larger scale such as that on the component or plate level. Analysis of this system on a larger scale is similar to the treatment of flow through a collection of small and similar particles as a collective porous media. Using some of the same analytical tools the offset strip fin heat exchanger will be analyzed in an effective porous media (EPM) model utilizing local volume averaged parameters to analyze larger scale phenomena.

The EPM model is implemented computationally in the Compact Heat Exchanger Explicit Thermal and Hydraulics (CHEETAH) code which can be used to analyze many compact heat exchanger designs. In this work the EPM model is developed and is then applied to a diffusion-bonded counter-flow compact intermediate heat exchanger as an illustrative and useful example. The method and code developed can also be applied to a parallel-flow or a cross-flow compact heat exchanger. In particular, a gas-to-liquid intermediate heat exchanger (IHX) is analyzed as an illustrative example for the methodology because it presents unique mechanical challenges associated with a large pressure drop between the fluids and a large temperature change in the gas due to its low volumetric heat capacity. More broadly, the system parameters in CHEETAH can be changed to simulate other single phase fluids, flow rates, and geometries.

1.1 Intermediate Heat Exchanger Geometry

The IHX being studied is built from a diffusion-bonded stack of plates with alternating geometry. With arrays of small offset strip fins on each side, the plates are designed to enhance heat transfer between fluids carried in counter-flow in spaces above and below it. In this case the heat exchanger is gas-to-liquid; when stacked, the plates alternate between those designed to carry gas and referred to as the gas plate and the other designed to carry liquid and referred to as the liquid plate. Furthermore, helium at 7 MPa is assumed to be the primary reactor coolant, meaning that it will be the hot fluid in the IHX. The liquid is assumed to be a liquid or 'molten' salt called FLiNaK, whose major constituents include lithium, sodium and potassium fluorides [4]. The salt has a high volumetric heat capacity making it a very effective high-temperature heat transfer fluid in the intermediate loop. FLiNaK is therefore the cold fluid in this intermediate heat exchanger.

The gas and liquid plates physically separate the two fluids and enhance heat transfer between them. Most of the heat transfer occurs in the OSF region of each plate while most of the pressure drop occurs in the liquid plate's pressure distribution channels leading to and from the OSF. The two plates share their overall bounding dimensions, allowing them to assemble; however, their manifolds, fin, and channel dimensions are unique. Schematics of the gas and liquid salt plate showing the fluid flow directions can be seen in Figure 1-1.

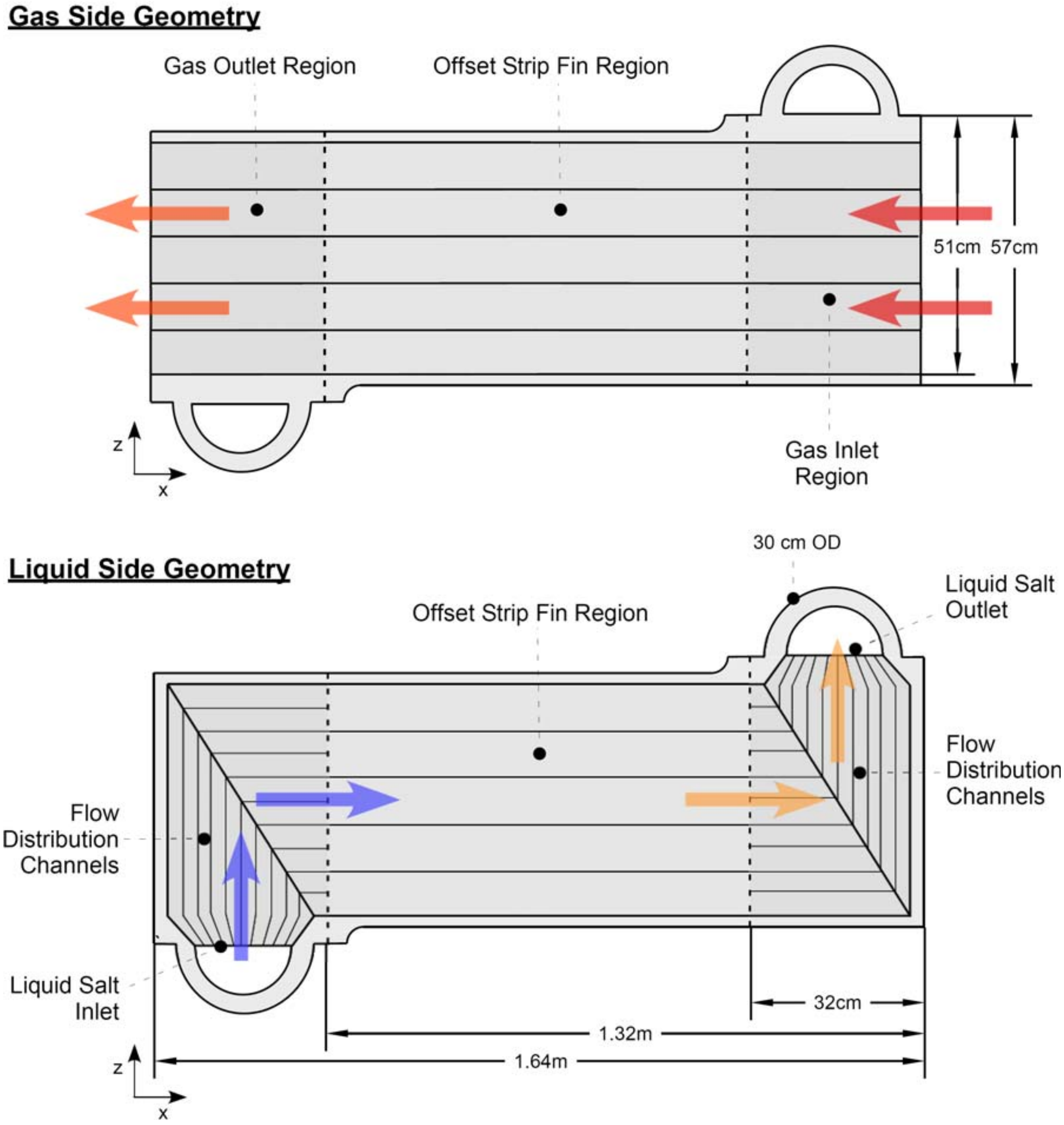

Figure 1-1: Schematic of gas and liquid plate geometries and flow in the IHX.

Detailed views of the manifolds and offset strip fin regions can be seen in the isometric views from the solid models of these plates provided in Figure 1-2.

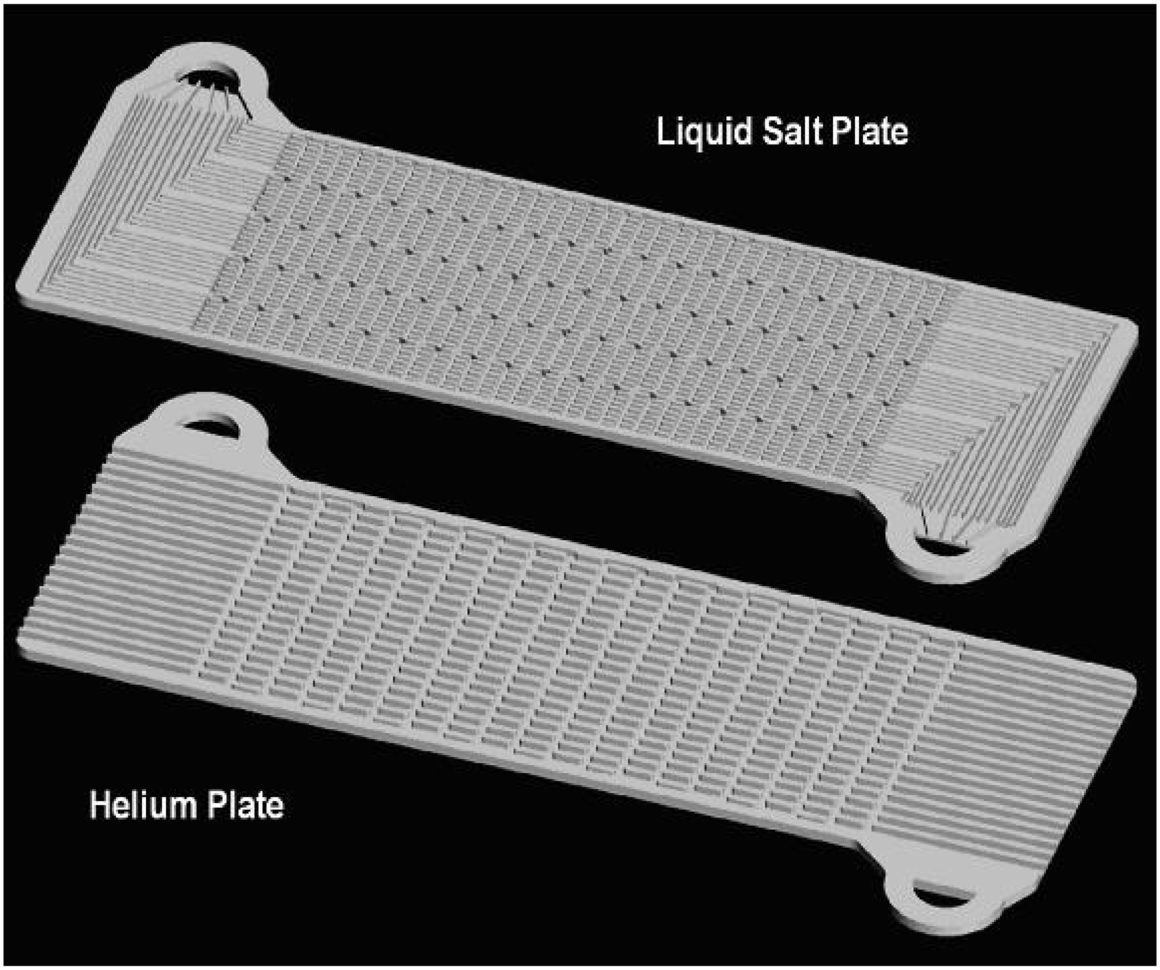

Figure 1-2: Solid models of liquid salt and helium plates in the IHX.

Detailed sizing calculations for the design of the IHX have been performed. Initially, this analysis was done by Dr. Haihua Zhao at the University of California, Berkeley. Later, the author of this work modified the previous analysis for slightly larger heat exchanger dimensions to those that were currently more feasible to manufacture.

The complete sizing analysis is executed in a MathCad worksheet and can be found in Appendix A.

The objective of this work lies in developing a method and associated tools to design and improve a 50 MW heat exchanger consisting of multiple modules, testing for viability at high temperature and with a significant (7 MPa) pressure difference between the fluids. The heat exchanger studied here would be one of roughly 15 modules that would make up the IHX for a 600 MW (thermal, or roughly 286 MW electric) modular helium reactor. The device would take advantage of small fins and channels to create hydraulic diameters that achieve high convection coefficients in the offset strip fin regions. This is particularly useful on the liquid side where, to achieve the desired heat transfer, the high volumetric heat capacity ($\rho * c_p$) of the liquid salt permits very low Reynolds number flows, low pumping power, and a moderate pressure drop along the length of the heat exchanger.

In fact, in the manifolds and offset strip fin region of the liquid plate the slow flow of liquid salt can be analyzed using the Darcy formulation [5,6]. Established friction factor correlations can be used to find an effective permeability so that Darcy's transport equation provides a linear relationship between the mass flow rate and gradient of the flow potential. The constant in this linear relation is called the hydraulic conductivity in groundwater hydrology because the equation is analogous to Fourier's law for conduction. This hydraulic conductivity is a function of the effective permeability, viscosity and density of the fluid. In the gas flow region the flow has Reynolds numbers is in the hundreds meaning that the regime is not Darcian. However, by knowing the steady state flow rates, density, and viscosity, an effective permeability can be calculated using a technique presented later when the volume averaged effective permeability of the media is presented.

1.2 Volume-Averaged Properties

One of the main advantages of the effective porous media (EPM) model being presented here is the ability to focus on component scale flow distribution, pressure losses, and heat transfer via volume averaging. This allows the user to pursue solutions at the scale of the composite plate, using information from previous work that focused on the local scale or fin scale phenomena. It is critical that the correlations used to find volume-averaged properties be used within their established range of validity. Correlations are chosen based on average flow rates calculated from general sizing calculations for the heat exchanger that can be found in Appendix A. This approach allows the user to avoid having to discretize and analyze flow and heat transfer simultaneously at both the largest and smallest geometric scales, something that would require a prohibitive grid resolution.

A more detailed analysis on the fin scale would involve looking at phenomena in the periodic thermal-boundary layers created in the interrupted flow by the offset strip fins. This type of analysis could focus on the flow through a single channel over a row of fins. In this scenario, the variation of the convection coefficient over the length of the fin row could be examined. The fluid temperature profile as a function of distance beginning at the leading edge of the first fin until the trailing edge of the second fin could also be studied to improve fin shape and spacing. A study investigating phenomena at this scale has been performed using a computational fluid dynamics (CFD) code by collaborators, Subramanian et al. at UNLV. Temperature profiles from that work illustrate fin-scale phenomena and are shown below in Figure 1-3.

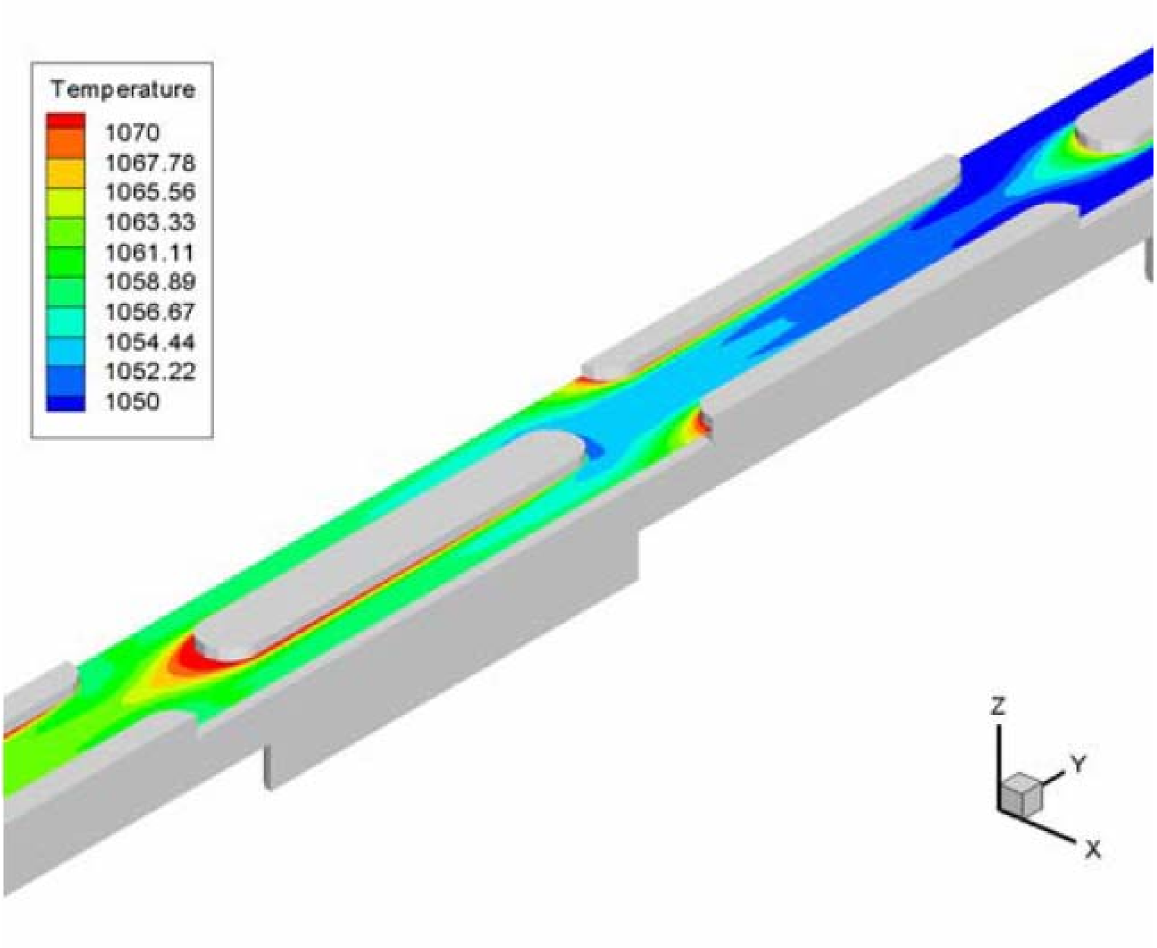

Figure 1-3: Temperature contours in the flow direction of the liquid salt in a high temperature heat exchanger – Ponyavin et al. [7]

In the case shown above, the temperature variation over the set of fins is the matter of interest, as it aids in understanding fin scale phenomena. Hu and Herold have also published work examining the effects of Prandtl number on pressure drop, on heat transfer and on the length of the developing region [8].

However, the primary interest in this work involves thermal analysis on the heat exchanger module level, in order to determine thermal expansion and stresses under steady state and transient conditions. These phenomena will not be dominated by what happens at the fin scale, but rather by the large temperature variation over a long and flat plate-type offset strip fin heat exchanger plate. It is important to point out that examining this plate at the fin scale would be computationally prohibitive. Instead, at the system scale one focuses on system scale phenomena and uses Nusselt correlations evaluated from well established experimental sources for these geometries.

These heat transfer correlations are well documented in classic sources such as Kays and London [9]. For the case of interest here, a correlation submitted by Manglik and Bergles [10] fits for the offset strip fin heat exchanger arrangement and range of Reynolds numbers. This work by Manglik and Bergles is a good overview of work done on the offset strip fin geometry. It includes results published by Kays and London, Joshi and Webb, Weiting, Manson, and Mochizuki et al. Applying Nusselt numbers rooted in correlations defined for periodic fully-developed flow such as those by Manglik and Bergles allows the EPM model to discretize with a significantly coarser grid (100 times coarser than would be used in a traditional analysis using CFD). Since decreasing the grid size causes a quadratic increase in the number of computations required, increasing the grid size greatly reduces the computational resources required to analyze transient behavior in a large and complex heat exchanger module.

In the thermal hydraulic model there are many local volume-averaged properties that are important. These properties include the hydraulic diameter D_h, phase fraction ϕ, medium permeability, k, surface area density, and the convective heat transfer coefficient, h. With the exception of the temperature dependent fluid properties, all of the above mentioned local volume-averaged properties are geometry specific. This means that it is the local detailed geometry of the plates that determines these local volume averages.

In order to calculate local volume averages, it is important to first specify the medium in which these properties will be defined. In this case, the medium will be the ‘composite plate’. Because the liquid and gas plates form an alternating stack, it is logical to treat the assembly of a gas and liquid plate as a uniform and repeating geometry. But if this assembly of the gas and liquid plate is used, an opportunity to achieve mechanical symmetry is lost. Since the composite plate geometry does provide mechanical symmetry it is used instead to define unit cells. This mechanical symmetry will become important later in the mechanical stress analysis. More importantly, by selecting this composite plate instead of the simple gas and liquid plate assembly, a repeating geometry is selected that is also symmetric on more planes. This technique simplifies the thermal hydraulic analysis. The selection of the composite plate from the assembled heat exchanger plate stack can be seen in Figure 1-4 below.

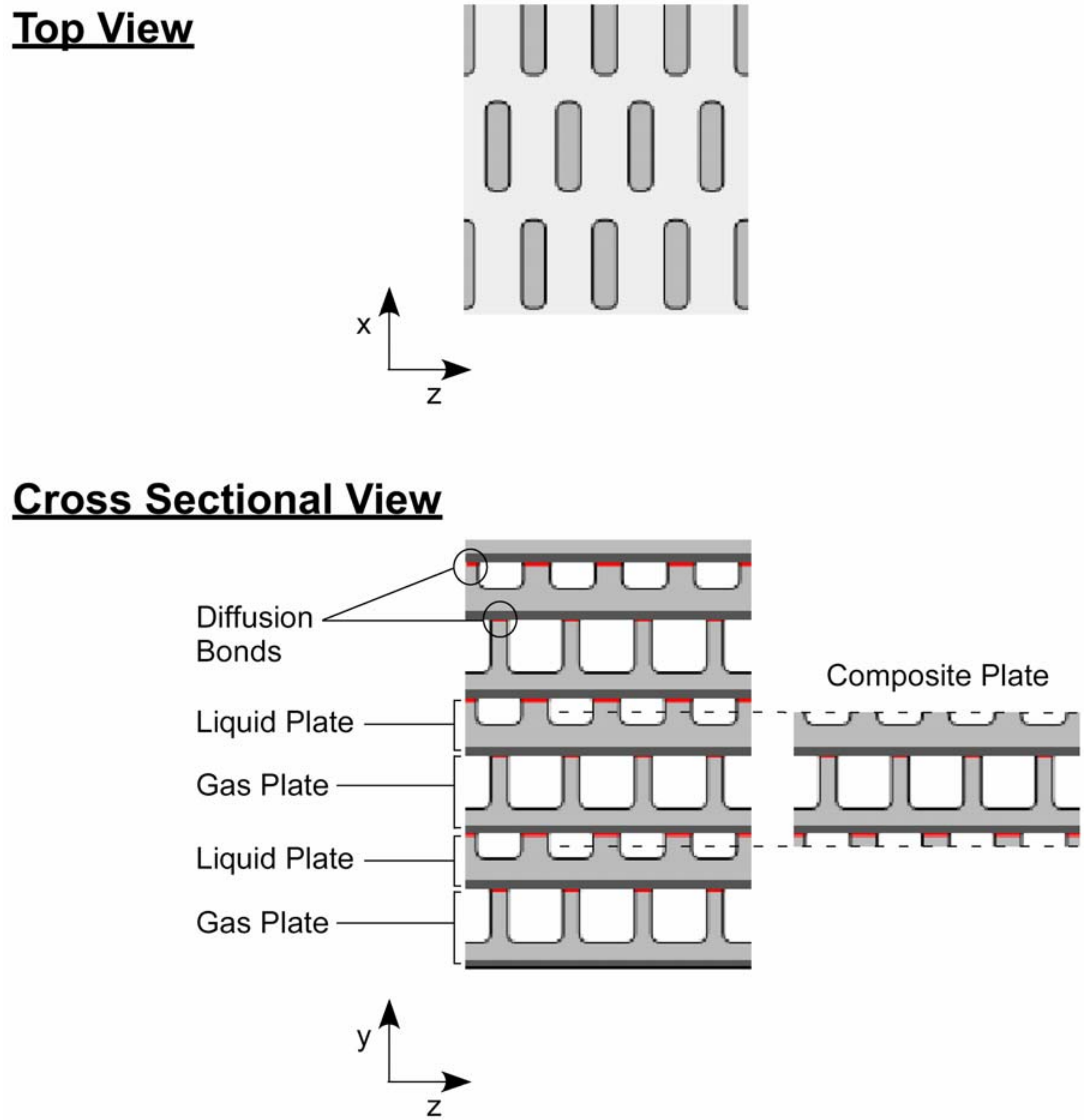

Figure 1-4: Cut-away view through the offset strip fin (OSF) section showing alternating liquid and gas flow channels. Dark bands at the top of each fin indicate the location of diffusion-bonded joints between the plates.

From the top view, this composite plate can be analyzed as having four fundamentally different regions that can each be characterized by a small volume that is repeated to yield the entire region. That characteristic volume will be referred to as the unit cell for that region and each unit cell will be analyzed for several pertinent volume-averaged properties. The four unit cells that make up the composite plate are shown in Figure 1-5.

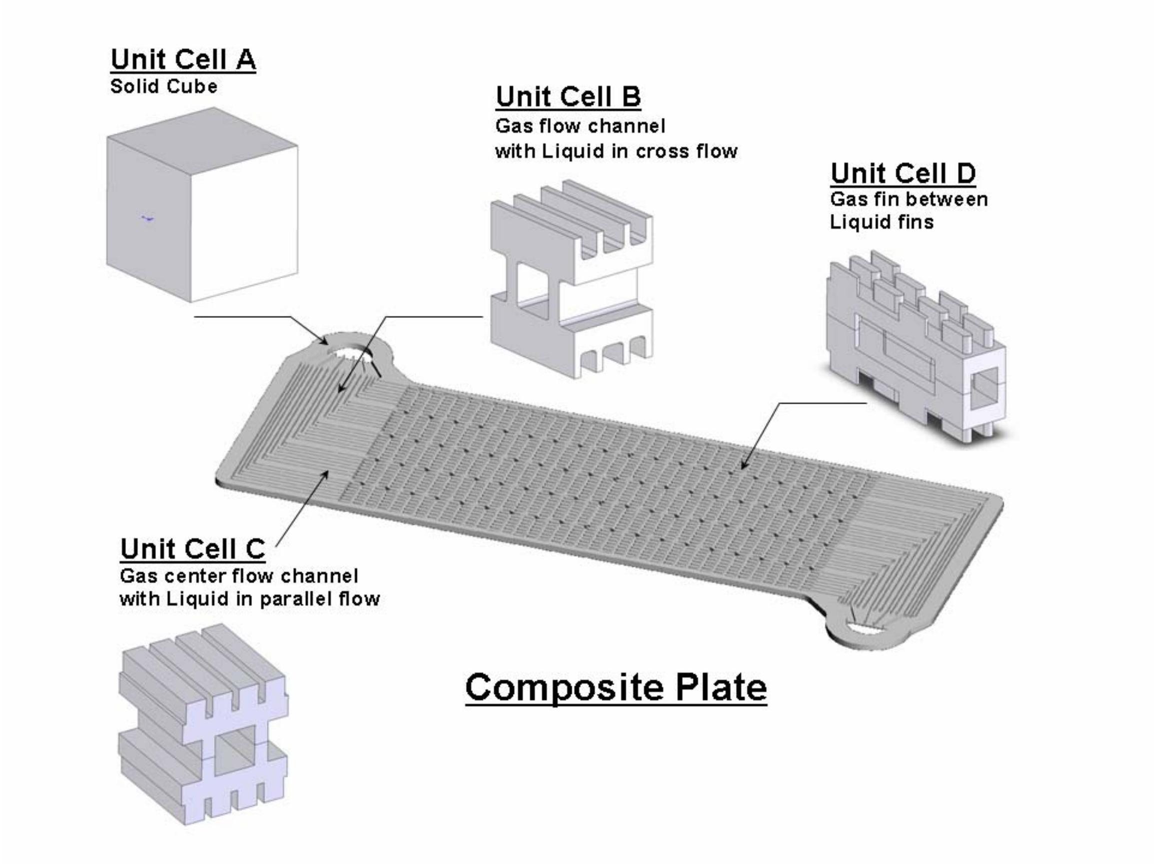

Figure 1-5: The four unit cells characterizing the complex geometry of the composite plate.

1.3 Phase Fraction

The phase fraction represents the ratio of the volume of a particular phase to the volume denoted by the largest dimensions of each unit cell in each of the principal directions. In Figure 1-6 below, the volume of the solid phase in unit cell C is shown on the left, while the volume of the box needed to contain it is shown bordered in red to the right. The ratio of solid phase volume to the box volume is referred to as the phase fraction. This is a local volume-averaged property within the zone of the IHX where unit cell C describes the local geometry.

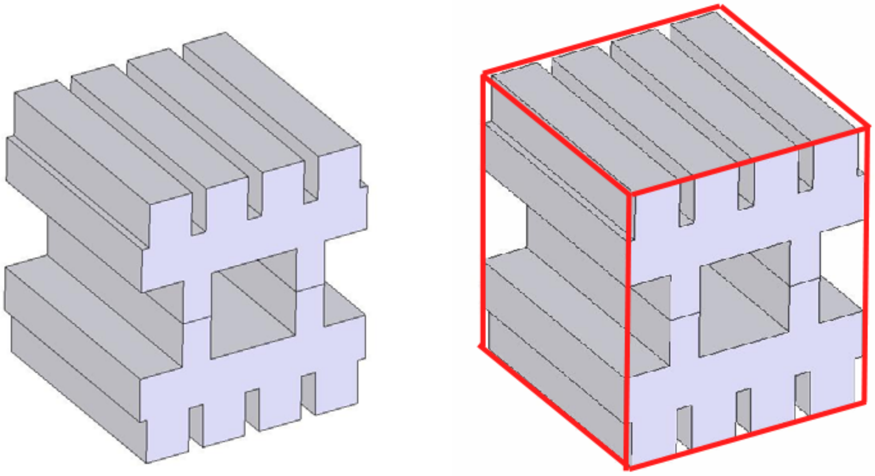

Figure 1-6: Solid phase fraction illustration for unit cell C (67%).

1.4 Media Permeability

The medium permeability is also obtained via a local volume average. Extensive analytical and experimental work has been done to characterize the heat transfer properties of many offset strip fin geometries. Kays and London, Shah, Webb and others have published a large body of correlations for the heat transfer characteristics of heat exchangers. Kays and London in particular published many correlations specifically for compact heat exchangers. While this subject is of great importance it is also one of great complexity because the phenomena influencing the fluid mechanics and heat transfer vary with fin geometry, flow regime, and with manufacturing methods used in making the fins for the compact heat exchanger.

Many correlations exist for widely varying conditions. Most often, however, the Fanning friction factor is used to quantify the pressure losses due to friction in the flow. The correlations for the Fanning friction factor very often have the following form:

$$f_f \propto C_1 \bullet \mathrm{Re}^c$$

Equation 1-1

where C_1 is a function of various parameters relevant to the fin and channel geometry and c is an empirical constant. Since these correlations are developed for flow over the length of an offset strip fin channel, the friction factor is a volume average over the entire length, width, and height of the flow path. This Fanning friction factor then allows the researcher to determine the permeability of the medium via a method explained in following section.

1.5 Determining the Effective Permeability

For one-dimensional, fully developed steady state laminar flow in a pipe, the axial component of the momentum equation can be solved for the average axial (x-direction) velocity $\bar{u}$ shown in Equation 1-2 [11].

$$\bar{u} = \frac{-D^2}{32\mu}\frac{d\Phi}{dx} \quad or \quad \bar{u}^2 = \bar{u} * \frac{-D^2}{32\mu}\frac{d\Phi}{dx} = -\mathrm{Re}\frac{D}{32\rho}\frac{d\Phi}{dx}$$

Equation 1-2

Here it can be clearly seen that $\frac{D^2}{32}$ serves as the geometry-dependent correction factor similar to the permeability, which has the same units.

This is also commonly expressed as:

$$\bar{u}^2 = -\frac{D}{2f_f\rho}\frac{d\Phi}{dx}$$

Equation 1-3

whereby the Fanning friction factor for laminar flow in a pipe is thus

$$f_f = \frac{16}{\mathrm{Re}}$$

Equation 1-4

Now dividing Equation 1-3 by the average fluid velocity gives the following equation for flow in a pipe.

$$\bar{u} = -\frac{D\mu}{2f_f\rho\bar{u}}\frac{1}{\mu}\frac{d\Phi}{dx}$$

Equation 1-5

Applying this to the effective porous medium for laminar, fully developed steady state flow, the diameter D is replaced by the hydraulic diameter D_h and the average velocity is represented as $\bar{u}$ (average velocity in a pipe or analogous to the interstitial velocity in the effective porous medium). The Darcy velocity u_D is the interstitial velocity divided by the phase fraction, ϕ, (conventionally referred to as the porosity), as follows:

$$\bar{u} = u_{\mathrm{int}} = \frac{u_D}{\phi} \qquad \textit{Equation 1-6}$$

Thus Equation 1-5 becomes

$$u_D = -\frac{D_h \mu \phi_x{}^2}{2 f_f \rho u_D} \frac{1}{\mu} \frac{d\Phi}{dx} \qquad \textit{Equation 1-7}$$

This finally determines the relationship between the Fanning friction factor and the effective permeability as:

$$k_x = \frac{D_h \mu \phi^2}{2 f_f \rho u_D} \qquad \textit{Equation 1-8}$$

Because the Fanning friction factor and thus the permeability are function of fluid velocity (especially at higher Reynolds numbers) the average velocity of the fluid flow must be known in order to calculate the permeability. In this case, the average velocity comes from mass flow rates determined from component sizing calculations that can be found in Appendix A. With the permeability known, the velocities at the fin-scale can be calculated. An array of fin-scale velocities forms a velocity field inside of the heat exchanger.

Naturally, all correlations for offset strip fin geometries will show terms that are specific to the fin and channel geometry and a term or terms that reflect the flow regime via a Reynolds number dependence to some power. Because of its simplicity Kays' correlation for the Fanning friction factor in an offset strip fin array serves as a good illustrative example of the relevant terms in these correlations. In Kay's correlation, *t* denotes the thickness of the fins and *l* represents the length of a fin in the offset strip fin arrangement [12].

$$f_f = 0.44\left(\frac{t}{l}\right) + 1.328\,\mathrm{Re}_l^{-0.5}$$

Equation 1-9

The CHEETAH code uses the following Manglik and Bergles correlation for the Fanning friction factor in an offset strip fin core [10]:

$$f_f = 9.6243\,\mathrm{Re}^{-0.7422}\,\alpha^{-0.1856}\delta^{0.3053}\lambda^{-0.2659}(1+7.669*10^{-8}\,\mathrm{Re}^{4.429}\,\alpha^{0.920}\delta^{3.767}\lambda^{0.236})^{0.1}$$

Equation 1-10

Equation 1-10 is valid over a very wide range of Reynolds numbers. The published results show that it exhibits proper asymptotic behavior at extremely high and low Reynolds number values conforming to experimental data for a wide variety of cores. The authors point out that friction factor data (as well as Colburn factor data for heat transfer) is accurate to ± 20% [10]. It is well known that manufacturing variations such as burred edges and surface roughness will have a significant effect on pressure drop. In

Equation 1-10 α, δ, and λ are variables that characterize the fin and channel geometry inside of the offset strip fin core. The above correlation from Manglik and Bergles is implemented in the CHEETAH code.

This result plays a very important role in the implementation of the fluid dynamics of the CHEETAH Code. It allows the script to evaluate an effective permeability from the Fanning friction factor. It is important to note that both the permeability and the Fanning friction factor are functions of velocity through the Reynolds number. At very low flow rates such as the creeping flows that characterize the Darcy flow regime, the permeability is largely a medium-dependent property; this is the case for most hydrology and petroleum engineering applications.

A real advantage of this technique is the fact that the fluid potential distribution is found with the same equation in core flow zones, the boundary conditions, and the no-flow areas, provided that the permeability distribution is correctly specified. This also implies that the best correlations giving the Fanning friction factor for any complex geometry can be used to generate an effective permeability, which will accommodate the flow rates in the range of validity of the Fanning friction factor correlation.

From a programming standpoint this makes the CHEETAH Code very versatile and easy to adjust for different fin arrangements and geometries or dimensions, because only the Fanning friction factor correlation in the code must be changed. This is a very significant advantage because it takes the complicated correlation out of the iterative processes in the code by first using the correlation to calculate a spatially varying distribution of direction permeabilities. This saves much computation time and makes the effective porous media (EPM) treatment advantageous. For some heat transfer surface geometries tested correlations may not exist. For such cases it would be necessary measure flow resistance experimentally and use these measurements to establish the effective permeability.

1.6 Fully Developed Flow

For this approach, it is important to show that the flow has reached a hydrodynamically fully developed condition. The offset fin studies of Hu and Harold, Sparrow et al, and Kelkar and Patankar show that for Graetz number, Gz<200 the flow has effectively reached a periodic hydrodynamic fully developed condition [8, 13, 14].

$$Gz = \frac{\mathrm{Re}^* D_h}{x} \qquad \textit{Equation 1-11}$$

For the IHX being analyzed here, on the liquid-side the Reynolds number varies between 20 and 50 with a hydraulic diameter near 4 mm. This makes the hydro-dynamic entry length is just a fraction of a millimeter on a 1 meter core section making it less than 1% of the core length on the fluid side. Similarly, on the gas-side of the IHX the Reynolds number is near 2600 with a hydraulic diameter of 6 mm. The hydrodynamic entry length is therefore larger on the gas plate at around 6.0 cm in length or 6% of the core length on the gas side. In this analysis for both cases the flow is treated entirely as fully developed.

1.7 Convection Coefficient

Offset strip fins are widely used due to their compact nature and high effectiveness in enhancing heat transfer. The enhancement to heat transfer stems from the periodic starting of a new boundary layer on each fin and its subsequent elimination in the wake following the fin. The fin spacing is most often uniform with roughly half-fin spacing in between fins [10]. Manufacturing processes can also influence heat transfer enhancement by producing burred edges and affecting surface roughness. The heat transfer enhancement comes with increased pressure drop as the finite fin thickness produces form drag and enhanced viscous shear.

The Colburn factor, j, is related to the Nusselt number as follows:

$$j = Co = St \cdot \mathrm{Pr}^{2/3} = Nu/(\mathrm{Re} \cdot \mathrm{Pr}^{1/3})$$ *Equation 1-12*

Or

$$Nu = j \cdot (\mathrm{Re} \cdot \mathrm{Pr}^{1/3})$$ *Equation 1-13*

and therefore

$$h = j \cdot (\mathrm{Re} \cdot \mathrm{Pr}^{1/3}) \frac{k_f}{D_h}$$ *Equation 1-14*

As an illustrative example of a simple correlation for the Colburn factor, j, Kays used the following correlation for a laminar boundary layer over an interrupted plate geometry.

$$j = 0.665\,\mathrm{Re}_l^{-0.5}$$

Equation 1-15

The Colburn factor is a function of fluid velocity; in order to specify the convection coefficient distribution in the CHEETAH code, the average velocities were initially used. These velocities came from mass flow rates determined from component sizing calculations that can be found in Appendix A. Later versions of the code use velocities solved at the fin-scale to calculate local Reynolds numbers from which the convection coefficients are calculated at the fin-scale.

As with the Fanning friction factor, in the offset strip fin region the CHEETAH code uses a more complicated Colburn factor correlation by Manglik and Bergles (Equation 1-16) that is valid over a large range of Reynolds numbers and includes the correct asymptotic behavior. The authors point out that the Colburn factor data are accurate to ±20% due to variability of many relevant factors including surface roughness and manufacturing methods [10].

$$j = 0.6522\,\mathrm{Re}^{-0.5403}\,\alpha^{-0.1541}\delta^{0.1499}\lambda^{-0.0678}(1+5.269*10^{-5}\,\mathrm{Re}^{1.340}\,\alpha^{0.504}\delta^{0.456}\lambda^{-1.055})^{0.1}$$

Equation 1-16

1.8 Surface Area Density

Finding the surface area density of each unit cell is straight forward. It involves finding the ratio of the surface area in contact with the liquid and dividing by the volume found by multiplying the largest dimensions of each unit cell in each of the principal directions. More concisely, it is the surface area in contact with the fluid divided by the volume of the box needed to enclose the unit cell (see Figure 1-6). A surface area density exists for each fluid and each unit cell.

1.9 Effective Conductivity

Due to the stacked assembly, the flow areas on the liquid and gas plates overlap in many regions of the composite plate creating zones in the solid material with complex geometry and complex mechanical and thermal unit-cell properties. One of these properties is the directional conductivity in each unit cell that makes up the composite plate seen in Figure 1-5. In order to find the directional conductivity of each of these unit cells, the conductivity of the material is inserted into a FEA code. In this case both ANSYS and COMSOL were used. With the material conductivity specified, a temperature is imposed on opposite planes of the unit cell and the FEA is then able to find the steady state temperature gradient through the material. Clearly some areas will be thicker than others and will thus have a lower effective conductivity. The FEA code can readily solve for the conduction heat transfer through the complex geometry of the solid material in the unit cell. This heat transfer rate, divided by the area of the entire face (not just the solid fraction) will give the effective conductivity of the unit cell in that direction.

1.10 Fluid Dynamics

Initially, thermophysical constants such as density and viscosity were treated as constants to facilitate the creation of the initial thermal hydraulic model presented here. In later versions of the model these properties were made temperature-dependent to increase accuracy. Including the temperature-dependent thermophysical properties better reflects flow maldistribution phenomena that would result from complex temperature distributions in the heat exchanger. This was particularly important when investigating the feasibility of gas-cooled reactors, because the relatively low volumetric heat capacity (relative to liquid-cooled reactors) of the gases requires both high volumetric flow rates and results in considerable changes in temperature from inlet to outlet for a given heat input.

1.11 Fluid Dynamics Equations

In all cases involving steady flow, mass must be conserved in any representative control volume in the field of flow along a plate. Two-dimensional mass conservation can be expressed in the equation of continuity while assuming constant density in both fluids as follows:

$$\frac{\partial u}{\partial x}+\frac{\partial w}{\partial z}=0$$

Equation 1-17

Darcy's transport equation serves as a modified momentum equation relating pressure gradients to fluid velocities. The effective permeability, k_x and k_z are functions of the geometry and Reynolds numbers.

Darcy's transport equation for one-dimensional flow in porous media is:

$$u_D=u_{\text{int}}\cdot\phi_x=-\frac{k_x\rho g}{\mu}\frac{dh}{dx}\quad or\quad u_D=-\frac{k_x}{\mu}\frac{d\Phi}{dx}$$

Equation 1-18

$$w_D=w_{\text{int}}\cdot\phi_z=-\frac{k_z\rho g}{\mu}\frac{dh}{dz}\quad or\quad w_D=-\frac{k_z}{\mu}\frac{d\Phi}{dz}$$

Equation 1-19

Here, Φ is the flow potential (Pa) and u is the Darcy velocity such that $\Phi= P+\rho gz$. More information on the application of Darcy's transport equations to porous media can be found in references by Peaceman [5] and Domenico [3].

In order to find the velocity distribution in the IHX it is necessary to first find the pressure distribution. The following equation shows one way to accomplish this.

Due to spatially-varying viscosity μ and permeability k (density is assumed constant), the partial derivative of the x and z components of the fluid velocity gives:

$$\frac{du_D}{dx}=-\frac{1}{\mu}\frac{dk}{dx}\frac{d\Phi}{dx}+\frac{k}{\mu^2}\frac{d\mu}{dx}\frac{\partial\Phi}{\partial x}-\frac{k}{\mu}\frac{d^2\Phi}{dx^2}$$

Equation 1-20

$$\frac{dw_D}{dz} = -\frac{1}{\mu}\frac{dk}{dz}\frac{d\Phi}{dz} + \frac{k}{\mu^2}\frac{d\mu}{dz}\frac{d\Phi}{dz} - \frac{k}{\mu}\frac{d^2\Phi}{dz^2}$$ *Equation 1-21*

Combining Equation 1-20 and Equation 1-21 gives the following elliptic differential equation:

$$-\frac{1}{\mu}\frac{\partial k_x}{\partial x}\frac{\partial \Phi}{\partial x} + \frac{k_x}{\mu^2}\frac{\partial \mu}{\partial x}\frac{\partial \Phi}{\partial x} - \frac{k_x}{\mu}\frac{\partial^2\Phi}{\partial x^2} - \frac{1}{\mu}\frac{\partial k_z}{\partial z}\frac{\partial \Phi}{\partial z} + \frac{k_z}{\mu^2}\frac{\partial \mu}{\partial z}\frac{\partial \Phi}{\partial z} - \frac{k_z}{\mu}\frac{\partial^2\Phi}{\partial z^2} = 0$$

Equation 1-22

Initially, this equation was solved only within certain zones with constant *x* and *z* permeability, under the assumption of constant thermophysical properties. For this case, Equation 1-22 is reduced to the following elliptic equation:

$$\frac{k_x}{\mu}\frac{\partial^2\Phi}{\partial x^2} + \frac{k_z}{\mu}\frac{\partial^2\Phi}{\partial z^2} = 0$$ *Equation 1-23*

This equation was solved with appropriate boundary conditions using finite differencing for each phase, and it provided the steady state pressure fields for each fluid for constant thermophysical properties. This pressure field readily gave the velocity field for the areas of constant properties. This set of assumptions worked well within the offset strip fin portion of the IHX due to its constant permeability. As expected, the same technique was unstable when applied to the inlet and outlet manifolds where the geometry changes frequently and abruptly.

In order to more accurately determine the velocity field in these areas, the more complicated Equation 1-22 had to be solved. However, the finite difference scheme resulted in large instabilities in the zones where the permeability varies from node to node such as in the diffuser, reducer, and at the interface between two zones of different permeability, such as between the OSF region and the inlet and outlet manifolds. The instabilities arose from the first derivatives of permeability with respect to space, $\frac{\partial k_x}{\partial x}$ and $\frac{\partial k_z}{\partial z}$ because these values are undefined at the interface between two zones where there is a step change in the permeability.

This instability was overcome by using a finite volume analysis (FVA), commonly called the control volume approach. In this approach, the conservation equations are applied over a discrete area, volume, or grid from the outset. The velocities are obtained from the pressure relationships given in Darcy's transport equation. The FVA or control volume formulation involves performing a mass, momentum, and energy balance on a volume of predetermined size. Unlike the Taylor-series based approaches in the finite difference formulation, the FVA does not take the limit by reducing the control volume down to a point (differential region) but rather to a predetermined size [15]. This provides a significantly more stable solution that can tolerate step changes in conductivity, permeability, viscosity, and pressure since the conservation equation is asserted on each discrete area or volume in the grid over the discretized time. Of course, for explicit solutions certain stability criteria must be obeyed, such as the Fourier and Courant numbers; which are discussed in the following chapter.

1.12 Heat Transfer

After performing an energy balance on a differential element of each phase, the following differential equations can be solved to obtain the transient temperature of each phase. The equations that follow describe the phenomena included in the thermal hydraulic model.

1.13 Heat Transfer Equations

Hot Fluid (fh):

$$-u_{fh}\rho_{fh}c_{pfh}\frac{\partial T_{fh}}{\partial x}-w_{fh}\rho_{fh}c_{pfh}\frac{\partial T_{fh}}{\partial z}+k_{fh}a'_{fhx}\frac{\partial^2 T_{fh}}{\partial x^2}+k_{fh}a'_{fhz}\frac{\partial^2 T_{fh}}{\partial z^2}-h_{fhs}a'_{fhs}(T_{fh}-T_s)=\phi_{fh}\rho_{fh}c_{pfh}\frac{\partial T_{fh}}{\partial t}$$

Equation 1-24

In non-dimensional form:

$$-u_{fh}^{*}\frac{\partial T_{fh}^{*}}{\partial x^{*}}-w_{fh}\frac{\partial T_{fh}^{*}}{\partial z^{*}}+\frac{1}{Pe_x}\phi_{fhx}\frac{\partial^2 T_{fh}^{*}}{\partial x^{*2}}+\frac{1}{Pe_z}\phi_{fhz}\frac{\partial^2 T_{fh}^{*}}{\partial z^{*2}}-St_x\cdot a'_{fhs}L(T_{fh}^{*}-T_s^{*})=\phi_{fh}\frac{\partial T_{fh}^{*}}{\partial t^{*}}$$

Equation 1-25

In this case, it is important to consider the dimensionless Peclet number, which provides the ratio of the advective energy transport (thermal energy transport due to convective transport) and the conduction thermal energy transport. The Peclet number is defined as:

$$Pe = \frac{u * \Delta x}{\alpha} = \frac{u * \Delta x * \rho * c_p}{k}$$

Equation 1-26

The Peclet number for the helium flow is approximately 500, while the Peclet number for the liquid salt flow in the composite plate is near 165. In both cases, this means that the energy balance is dominated by the advective contribution to the point that the conductive contribution in the flow direction can be ignored with a negligible effect on accuracy.

Neglecting conduction in the hot fluid the energy balance is reduced to:

$$-u_{fh}\rho_{fh}c_{pfh}\frac{\partial T_{fh}}{\partial x} - w_{fh}\rho_{fh}c_{pfh}\frac{\partial T_{fh}}{\partial z} - h_{fhs}a'_{fhs}(T_{fh} - T_s) = \phi_{fh}\rho_{fh}c_{pfh}\frac{\partial T_{fh}}{\partial t}$$

Equation 1-27

Solid (s):

$$h_{fhs}a'_{fhs}(T_{fh} - T_s) - h_{sfc}a'_{sfc}(T_s - T_{fc}) + k_s a'_k \frac{\partial^2 T_s}{\partial x^2} + k_s a'_k \frac{\partial^2 T_s}{\partial z^2} = \phi_s \rho_s c_{ps}\frac{\partial T_s}{\partial t}$$

Equation 1-28

In non-dimensional form:

$$Fo_x \cdot \phi_{fhx}\frac{\partial^2 T_{fc}^{\ *}}{\partial x^{*2}} - Fo_z \cdot \phi_{fhz}\frac{\partial^2 T_{fc}^{\ *}}{\partial z^{*2}} + St_x \cdot a'_{fcs}L(T_{fh}^{\ *} - T_s^{*}) - St_x \cdot a'_{fcs}L(T_s^{*} - T_{fc}^{\ *}) = \phi_s \frac{\partial T_s^{*}}{\partial t^{*}}$$

Equation 1-29

Cold Fluid (fc):

$$-u_{fc}\rho_{fc}c_{pfc}\frac{\partial T_{fc}}{\partial x}-w_{fc}\rho_{fc}c_{pfc}\frac{\partial T_{fc}}{\partial z}+k_{fc}a'_{fcx}\frac{\partial^2 T_{fc}}{\partial x^2}+k_{fc}a'_{fcz}\frac{\partial^2 T_{fc}}{\partial z^2}+h_{sfc}a'_{sfc}(T_s-T_{fc})=\phi_{fc}\rho_{fc}c_{pfc}\frac{\partial T_{fc}}{\partial t}$$

Equation 1-30

In non-dimensional form:

$$-u_{fc}{}^{*}\frac{\partial T_{fc}{}^{*}}{\partial x^{*}}-w_{fc}\frac{\partial T_{fc}{}^{*}}{\partial z^{*}}+\frac{1}{Pe_x}\phi_{fhx}\frac{\partial^2 T_{fc}{}^{*}}{\partial x^{*2}}+\frac{1}{Pe_z}\phi_{fcz}\frac{\partial^2 T_{fc}{}^{*}}{\partial z^{*2}}+St_x\cdot a'_{fcs}L(T_s{}^{*}-T_{fc}{}^{*})=\phi_{fc}\frac{\partial T_{fc}{}^{*}}{\partial t^{*}}$$

Equation 1-31

Again, the Peclet number for the liquid salt flow rate is high, so the conduction effect is negligible in the flow direction.

Neglecting conduction in the cold fluid, the energy balance is reduced to:

$$-u_{fc}\rho_{fc}c_{pfc}\frac{\partial T_{fc}}{\partial x}-w_{fc}\rho_{fc}c_{pfc}\frac{\partial T_{fc}}{\partial z}+h_{sfc}a'_{sfc}(T_s-T_{fc})=\phi_{fc}\rho_{fc}c_{pfc}\frac{\partial T_{fc}}{\partial t}$$

Equation 1-32

Lastly, the CHEETAH code solves the energy equations at every control volume by balancing the energy transfer between phases over discrete steps in time. This energy balance on each finite volume for each phase is similar to the mass balance performed in the fluid dynamics portion. A combination of fluid flow, conductivity, and convective heat transfer between the phases result in an increase or decrease in sensible thermal energy for each control volume during each time step. This change in sensible energy manifests itself as a change in temperature of the finite volume for each phase. These energy balances are analyzed in greater detail in the following chapter.

1.14 Temperature-Dependent Fluid Properties

Solving for the fluid flow and temperature distribution using temperature-dependent thermophysical properties is particularly important for this case because of the large change in temperature in the fluids. Furthermore, the primary coolant (helium at 7 MPa for this reactor design) in particular experiences a large temperature change in the heat exchanger, because like all gases it has a volumetric heat capacity that is low compared to that of liquids. Among the thermophysical properties of both fluids, viscosity is by far the most sensitive to changes in temperature; however, the density of the helium also varies considerably over this large temperature change.

In this case, analyses are conducted using both constant and variable thermophysical properties; the temperature distribution found with constant thermophysical properties is used as the initial condition for the analysis using variable thermophysical properties. This initial temperature distribution is critical because it will determine the initial viscosity distribution, which will in turn allow the determination of the mass flow distribution after solving the equations presented in the previous section on fluid mechanics. Because it would be computationally expensive to calculate viscosity and density distributions for every time step, CHEETAH allows the user to adjust the time interval (number of time steps) with which the thermophysical properties are adjusted to the current temperature field.

Including the influence of temperature in CHEETAH was a priority primarily for the liquid salt because its viscosity is highly sensitive to temperature. This sensitivity is quite pronounced over the temperatures of interest and is shown in Figure 1-7.

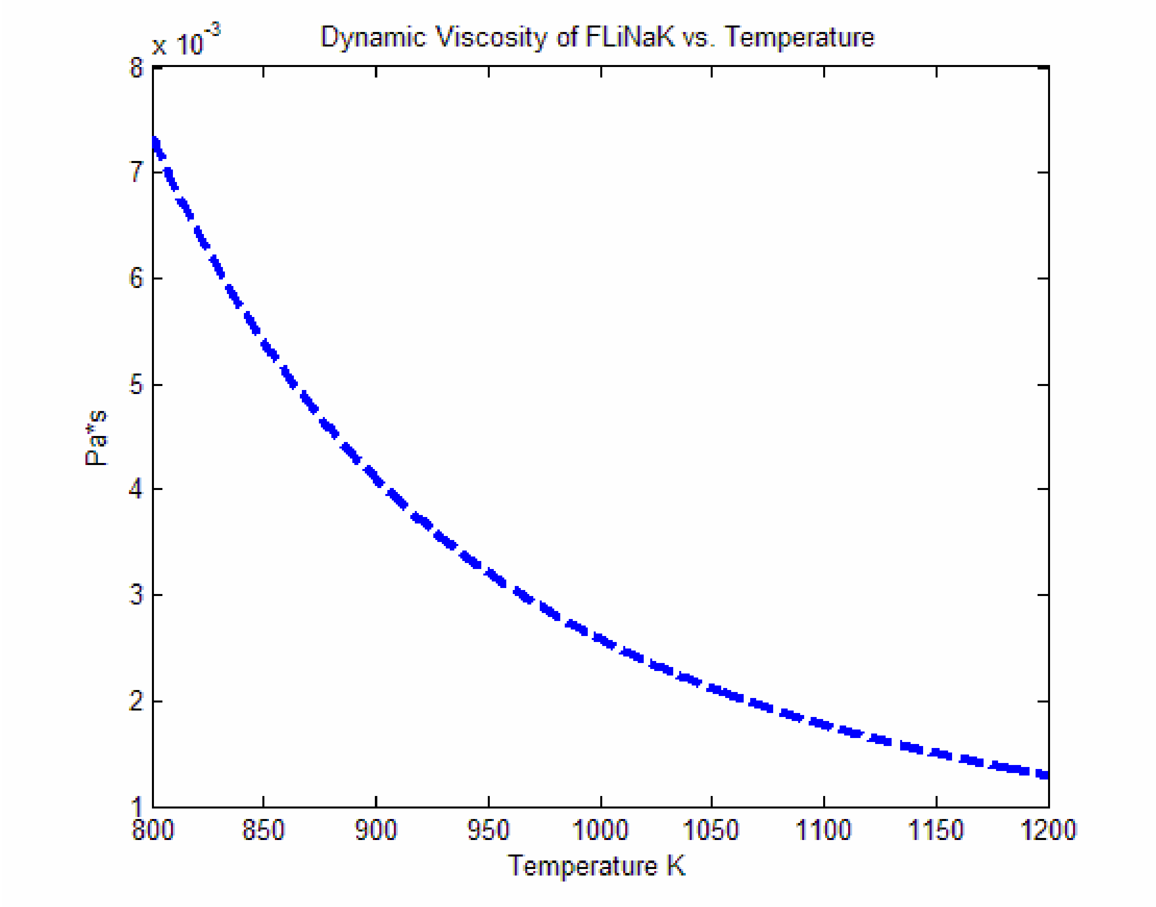

Figure 1-7: Dynamic viscosity of the liquid salt FLiNaK over temperature range set by fluid inlet temperatures to the IHX.

Viscosity correlations for liquid salts have been reported by Oak Ridge National Lab [ORNL]. The viscosity dependence is illustrated in Figure 1-8 below. LIF-NaF-KF (commonly referred to as FLiNaK) is of particular interest. A curve fit shows that the dynamic viscosity varies with temperature (K) as follows:

$$\mu(T) = 0.04e^{\frac{4170}{T}} \text{ [cP]} \qquad \mu(T) = \left(4\cdot 10^{-5}\right)\cdot e^{\frac{4170}{T}} \text{ [Pa*s]} \qquad \textit{Equation 1-33}$$

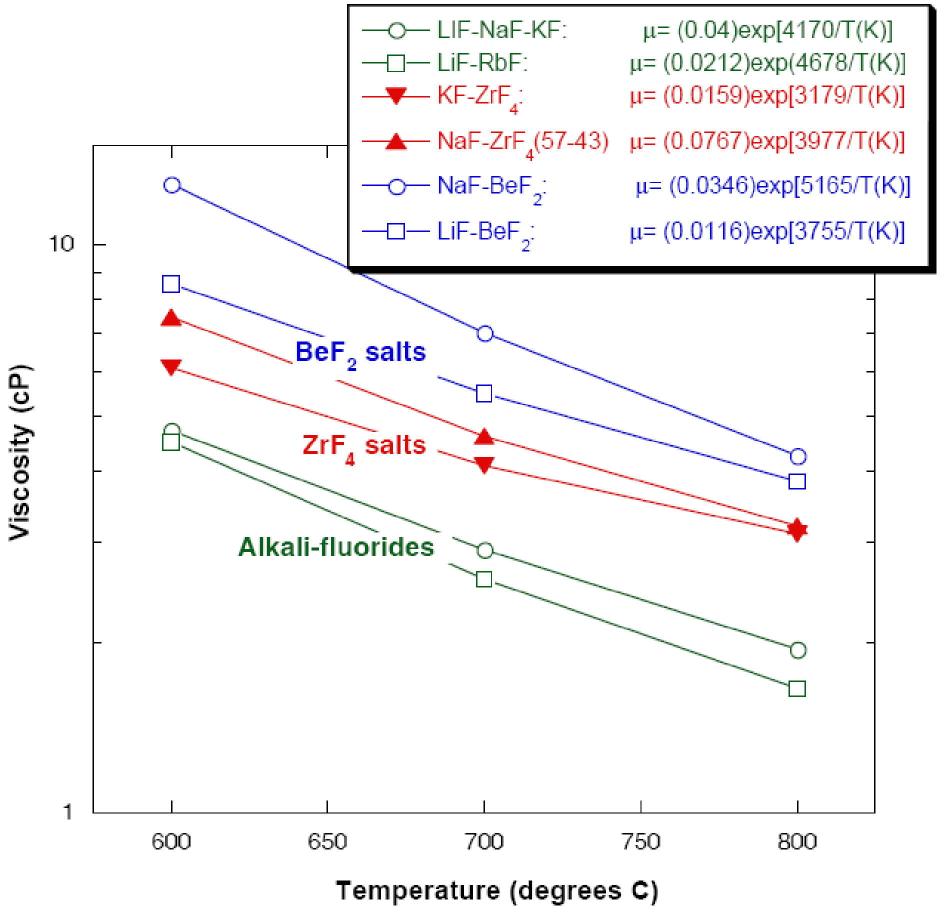

Figure 1-8: Liquid salt viscosity versus temperature plots from a candidate salt assessment report from Oak Ridge National Lab [4].

The temperature dependency of viscosity, specific heat, and density are graphed for helium at 7 MPa using values obtained from a NIST web book [16] in Figure 1-9 below. From these charts it is clear that the variation in specific heat is insignificant (.01%) compared with those for viscosity and density over the heat exchanger's temperature range. The viscosity of helium increases nearly linearly with temperature in this range and density varies inversely with temperature as dictated by the ideal gas law. The helium density can be found by applying the ideal gas law with an error less than 1%, when compared to the values tabulated in NIST. The table of thermophysical properties for high pressure helium is available in Appendix B.

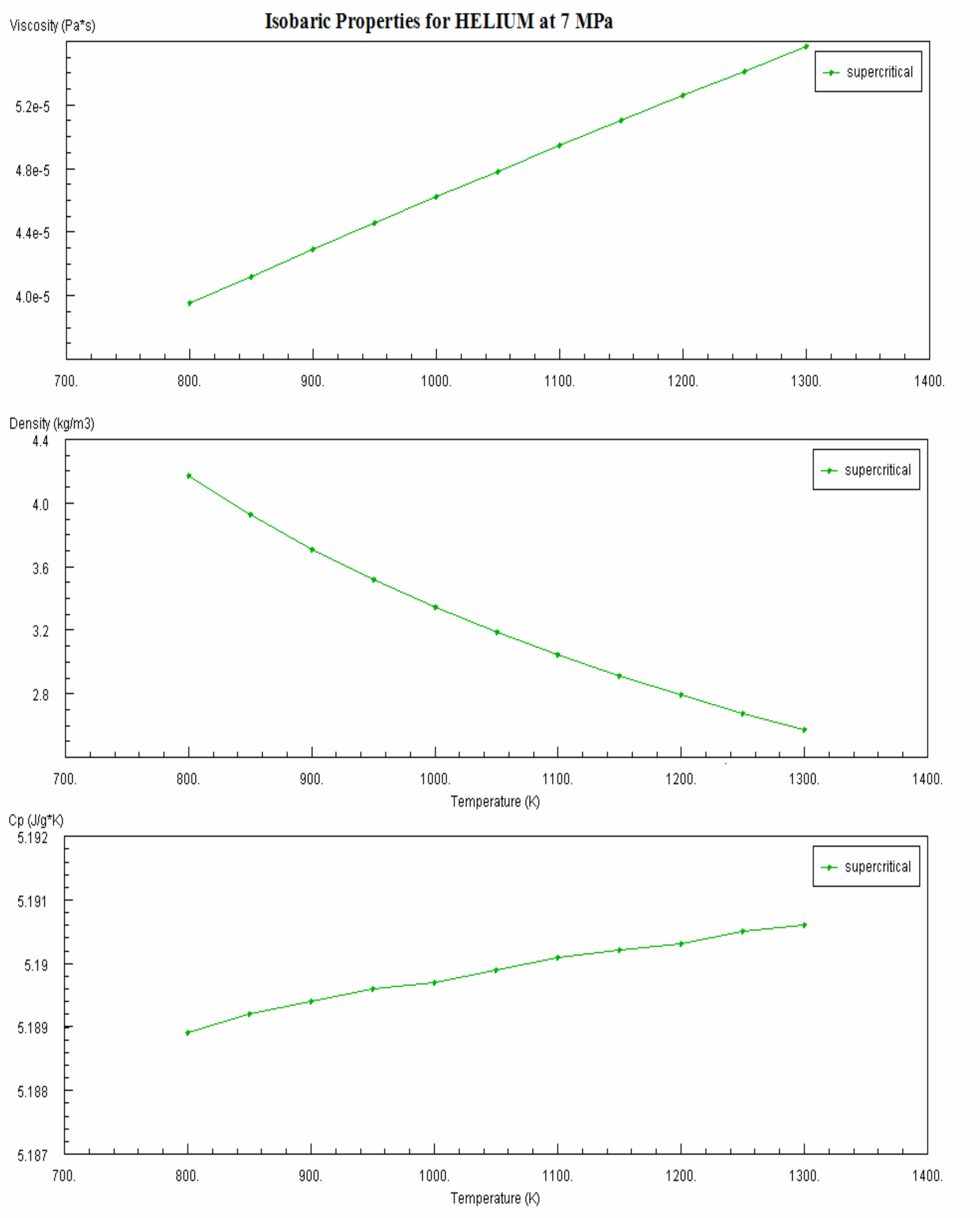

Figure 1-9: Isobaric thermophysical properties for helium at 7MPa from NIST.

Chapter 2

Partitioning, Discretization, and Numerical Method

In modeling the IHX, the actual material properties can be set and changed with great ease, as they are simply represented by a series of constants assigned in the input file (Systems Properties module) of the CHEETAH code. However, the fluidic, thermal, and mechanical response of the solid media comes from geometric effects that are central to the model's validity. This is where the EPM model simplifies the problem by creating mass and energy balances at a scale that will both include the complexity of the thermal hydraulics in the IHX and also yield results in a reasonable time period to permit fluidic, thermal, and mechanical improvements to the IHX design over various iterations.

Calculating the effective conductivities, permeabilities, phase fractions, surface area densities, convection coefficients, effective elastic moduli, shear moduli, and Poisson's ratios is very labor intensive because it takes over 20 unique zones with different media properties to fully describe the hydraulic, thermal, and mechanical properties of a typical compact heat exchanger. Some of these properties are calculated with correlations within the CHEETAH code, but others must be calculated on separate software (such as FEA and design software) and added to the input files. The nodal assignment of the above mentioned properties onto the array representing the IHX geometry is entirely automated and executed with various scripts within the CHEETAH code.

2.1 Zoning the IHX

The pressure and velocity distributions in the IHX are solved for both fluid phases by breaking up the IHX into over 20 flow zones. Each of these zones has unique physical properties that govern the flow for each of the two phases. Figure 2-1 shows the zoning for the composite plate.

For the case of an IHX that transfers heat between a liquid and a gas, it is representative to take the case of liquid salt for the liquid and helium as the gas. This is particularly relevant as they are among the fluid choices being considered by the U.S. Department of Energy’s Next Generation Nuclear Plant (NGNP).

The heat transfer analysis has been developed progressively starting with one-dimensional models that neglected longitudinal (main flow direction, *x*) conduction to two-dimensional models that include cross-flow in the fluids as well as spatially varying longitudinal and latitudinal (cross-flow direction, *z*) conduction. Early models used constant convection coefficients and surface area densities; the current analysis includes the spatial variation of all thermal and hydraulic parameters including temperature-dependent fluid properties.

The assignment of the geometry-dependent property distributions is a complex and essential function within the EPM model implemented in the CHEETAH code. The central purpose of the CHEETAH code is to enable the designer to simulate the performance of the IHX for a given geometry and set of dimensions; the heat exchanger design can then be improved in an iterative fashion based on the results of the simulation. Changing the dimensions of the IHX, fins, channels, and size of distributor channels in CHEETAH is accomplished by changing values in the input parameters file; however, significant changes to the shape of the IHX or manifolds require coding.

The CHEETAH code contains a long set of system parameters that define the external and internal geometry. The code will automatically change the zone boundaries so that the user does not have to modify the code with every dimensional variation. Manual modification of the code may be necessary if any of the dimensions approach the grid size or if the shape of the IHX is modified. A schematic drawing of the IHX's composite plate, Figure 2-1, shows the layout of zones where different thermal hydraulic parameters are defined. These zones apply the spatially varying phase fractions, surface area densities, convection coefficients, directional permeability, and directional effective conductivities in the IHX.

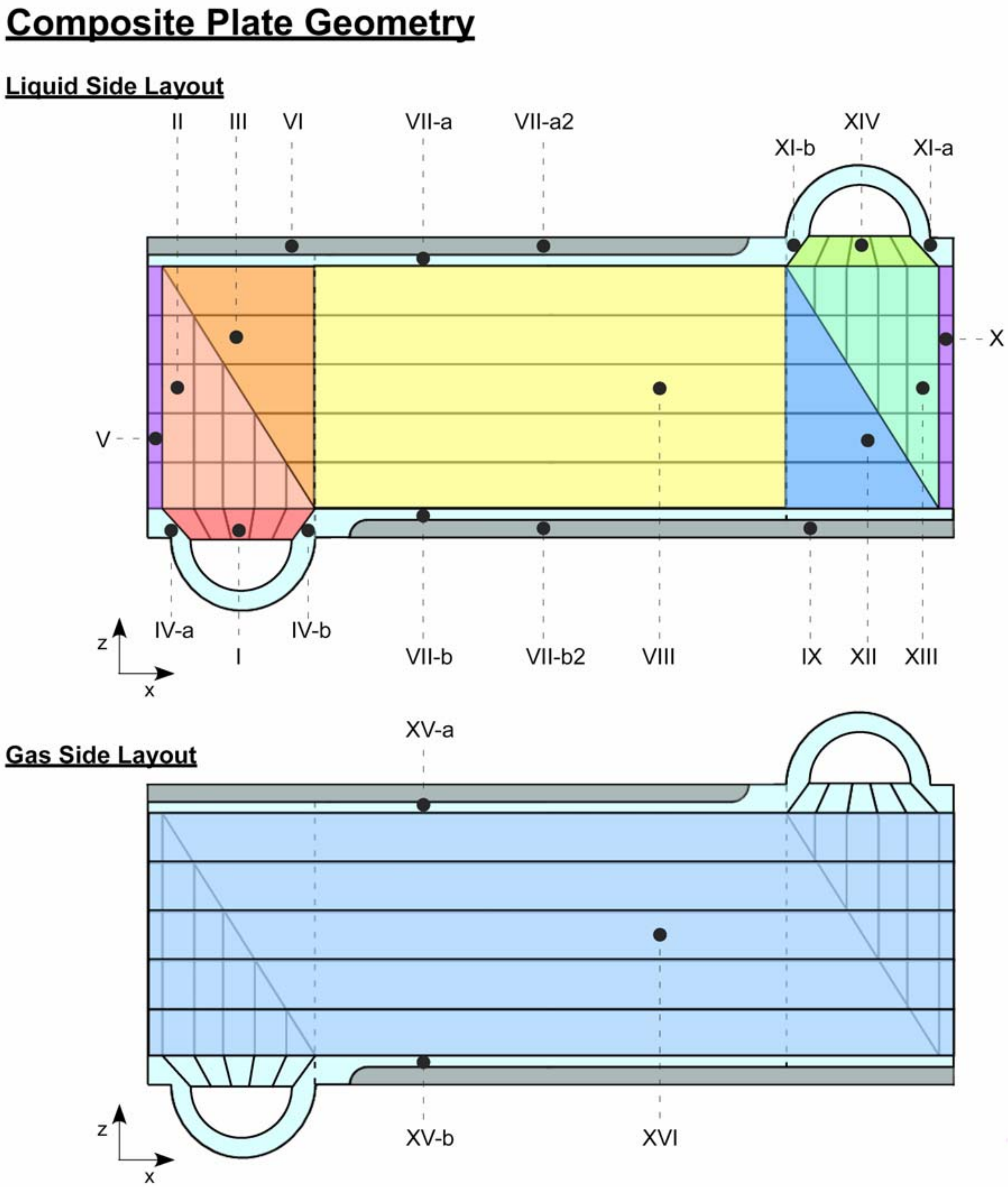

Figure 2-1: A schematic of the IHX's zoning distribution for thermal and hydraulic parameters in the CHEETAH code.

Zones IV-a, IV-b, VII-a, VII-b, XI-a, XI-b, XV-a, and XV-b, shown in light turquoise in Figure 2-1, represent a structural area where no fluid flows. For this reason, the areas have a phase fraction of 100% (ϕ=1), no surface density, and no convection coefficient. These zones will have a greater thermal inertia and will in general take longer to equilibrate during thermal transients. These zones will also have higher effective conductivity in all directions because the entire cross-section is available for heat flow, which reduces thermal resistance.

2.2 Diffuser and Reducer Permeability

The schematic drawing above is also simplified in the diffuser (zone I) and reducer (zone XIV) areas, which are shown as trapezoids. In these zones, every control volume has unique effective properties assigned to it depending on the local channel geometry being represented by the EPM. In order to accurately represent the local geometry, the assigned EPM uses the angle and spacing of the channels nearest to the node in the actual IHX. The CHEETAH code accomplishes this by finding the position of each node and the slope of the line connecting the node point to a central fictitious point to which the flow distribution channels align. Using the point and slope information for each node and the line equation from adjacent channels, the CHEETAH code finds the normal distance between channels at that node point and uses this to calculate a multiplier for the directional permeability so that the effective flow and cross-flow permeabilities at that node take into consideration not only the alignment of the channel but also the local channel density. These zones are shown in a uniform color here for simplicity, but each also includes other parameters that allow the CHEETAH code user to manipulate the flow distribution. This will be discussed further in the next section. Schematic drawings similar to Figure 2-1 would illustrate the layout of other effective property values such as effective conductivities, permeabilities, porosities, surface area densities, convection coefficients, effective elastic moduli, shear moduli, and Poisson’s ratios for the IHX.

2.3 Adjustable Flow Distribution

Improving the thermal design of a heat exchanger involves designing the device in such a way as to increase its thermal effectiveness. The thermal effectiveness is a ratio of heat actually exchanged between the hot and cold fluids to the maximum amount of heat that can be transferred between them given fluid inlet temperatures, specific heats, and flow rates. More generally, it is a number between zero and one that quantifies the performance of a thermal device. More detailed explanation on thermal effectiveness is available in texts by Mills [17], Incropera [18], and Çengel [19].

To increase the thermal effectiveness, it is crucial to create and maintain uniform flow in the heat exchanger in order to utilize the heat transfer surface area as uniformly as possible. Uniform flow increases the average residency of the fluid in the heat exchanger, which in turn increases total heat transfer. This is more obvious when considering that the convection coefficient is proportional to the square root of the Reynolds number. Therefore, flow maldistribution will create areas with higher flow speeds and therefore with higher heat transfer rates, but this comes at the more significant detriment of flow in other areas and therefore at the detriment of total heat transfer.

In order to create and maintain uniform flow though the IHX, the CHEETAH code accommodates the channel orientation and channel density in the nodal permeability assignment of the liquid plate. The distributors are in the liquid salt plate because that is where flow maldistribution is most likely to occur since the liquid salt viscosity is significantly more temperature-dependent [4]. The code also allows the designer to manually tune a multiplier coefficient for distinct zones in the sections containing the flow distribution channels. The adjustable permeability in these zones allows the user to quickly and directly manipulate the flow distribution as if controlling independent and parallel valves leading into and out of the OSF section. Shown in varying shades of yellow, the distributor channels in the liquid inlet can be seen in the liquid plate schematic drawing in Figure 2-2. The flow distributors for the liquid outlet can be seen in varying shades of green in Figure 2-2.

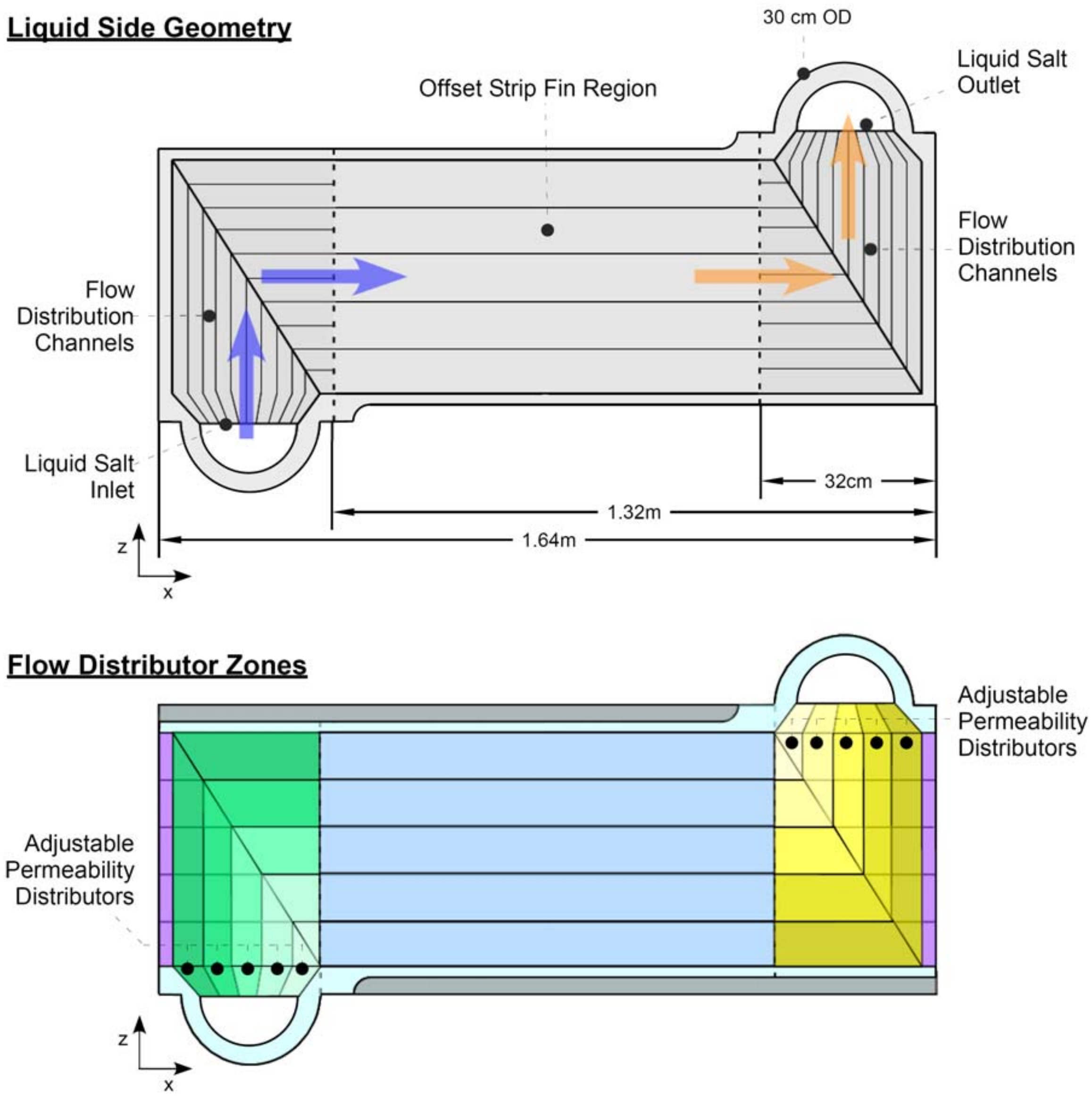

Figure 2-2: Adjustable permeability distributors in the liquid salt inlet and outlet zones.

The dimensions of these narrow passages can be independently specified in a manufactured heat exchanger. Likewise, the hydrodynamic parameters module in CHEETAH allows the designer to independently control the dimensions of these passages. From these specified dimensions, CHEETAH then evaluates the hydraulic diameter for each of these zones and uses it to calculate the effective permeability in each zone. The zones representing the distribution channels in the EPM model can be seen in Figure 2-1. These features in CHEETAH enable the control the flow distribution in the offset strip fin region where most of heat transfer takes place. In this region a small maldistribution of flow can significantly influence total heat exchanger effectiveness.

The lower flow resistance associated with the shortest flow path in the inlet manifold is already balanced by a higher flow resistance created by the corresponding longer flow path in the outlet manifold, so that the total flow resistance is roughly equal regardless of the path followed. However, there are still issues with flow maldistribution in the IHX. Among the factors that affect the flow distribution are the temperature-dependent viscosity effects (discussed in the next chapter) and the fact that the paths nearest the inner corners of each region are shortest and therefore have higher flow rates than the outside corners in each flow region.

Each inlet region is separated into several flow regions representing the flow distribution channels. The number of flow regions is specified by the assignment of a constant in CHEETAH's System Parameters module. The manifolds can be divided into any number of flow regions, but it is important to maintain a region width of at least three cells across to avoid discretization errors such as stair-casing, where the coarse mesh creates abrupt reductions in flow area and therefore peak velocities that can lead to instabilities by way of excessive CFL (Courant – Friedrichs – Levy = $u*\Delta t/\Delta x$) numbers.

2.4 Specifying the Grid

The CHEETAH code is written in Matlab and uses a rectangular mesh which fits the rectangular geometry of the IHX. The code was originally written with a typical rectangular grid, such that each node point lay in the center of the control surface and was identified by four coordinates (*x*-position, *y*-position, *z*-position, iteration number) with the following indexes (*i,j,k,n*), as is shown in Figure 2-3. The *y*-position (*j* index) in the rectangular grid connotes the phase with index *1* and index *3* being the fluids and index *2* always representing the solid phase. The CHEETAH Code was later improved by replacing the simple rectangular grid with a more sophisticated staggered grid.

The *x* and *z*-position coordinates (indices) associated with every node provide a physical Cartesian dimension for the node's location on the IHX geometry (with respect to an origin) when they are multiplied by the corresponding spatial discretization (Δx and Δz, respectively). Those Cartesian dimensions place the node within one of the previously delineated zones which in turn leads to the assignment of the corresponding local physical properties such as effective conductivities, permeabilities, porosities, surface area densities, convection coefficients, effective elastic moduli, shear moduli, and Poisson's ratios according to the zoning described previously.

2.4.1 Rectangular Grid

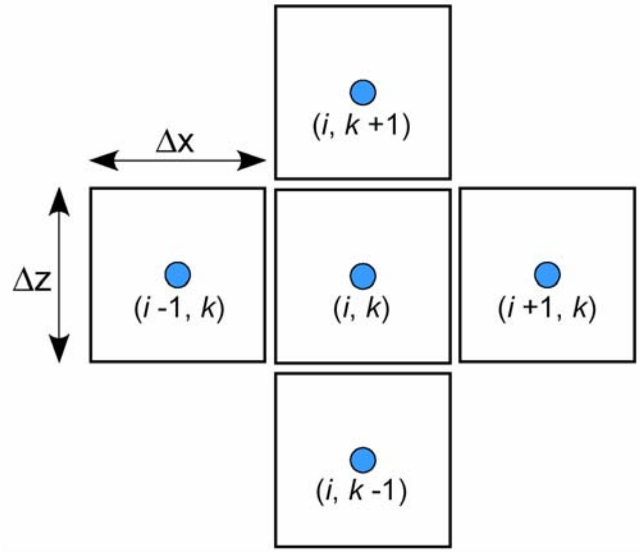

Figure 2-3: Rectangular grid discretization used in early versions of FVA code.

In this method of discretization all properties are assigned to the center of the control volume and mass conservation is checked at (*i,k*) by applying the following equation:

$$u(i-1,k)-u(i+1,k)+w(i,k-1)-w(i,k+1)=0 \qquad \textit{Equation 2-1}$$

However, this type of discretization uses a control volume four times larger than the actual grid spacing. This is because for continuity the velocities must be summed at the boundary of each cell, but since the velocities are defined at the center of each cell the code must calculate velocities from neighboring cells or must find an average velocity between two cells to approximate a boundary velocity. If neighboring cell velocities are used directly, this creates a much coarser grid than intended and significantly diminishes the accuracy of the results. If an average velocity is found then the computation time is increased. Furthermore, this method can also lend itself to 'zigzag' or 'checkerboard' pressure or temperature distributions since the continuity and momentum equations use information from alternating nodes to check for continuity [20]. Essentially, this means that a wavy pressure distribution will produce a wavy velocity distribution that can satisfy continuity, since it is information from alternating and not adjacent nodes that must satisfy continuity [20].

2.4.2 Staggered Grid

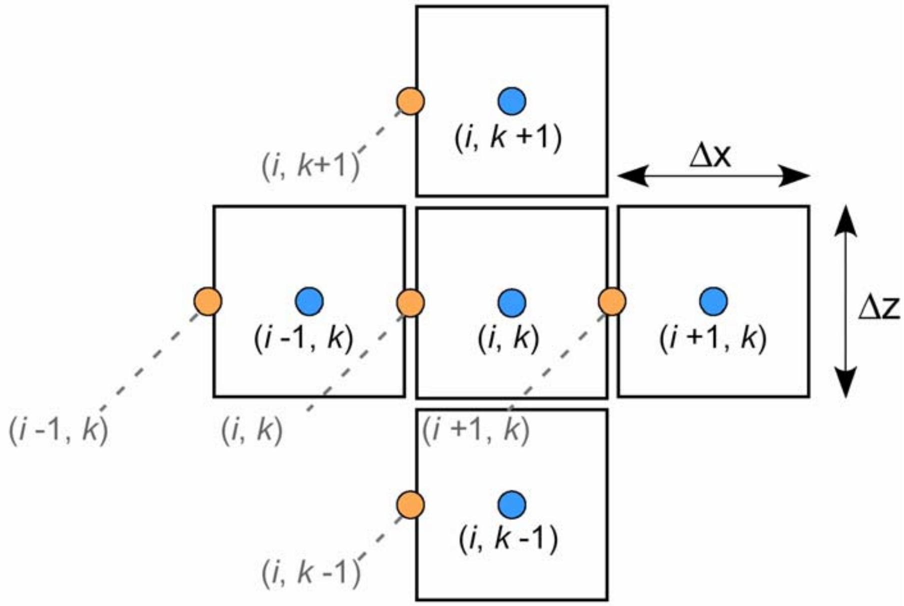

Figure 2-4: Staggered grid in x-direction illustrating indexing on left side of control volume.

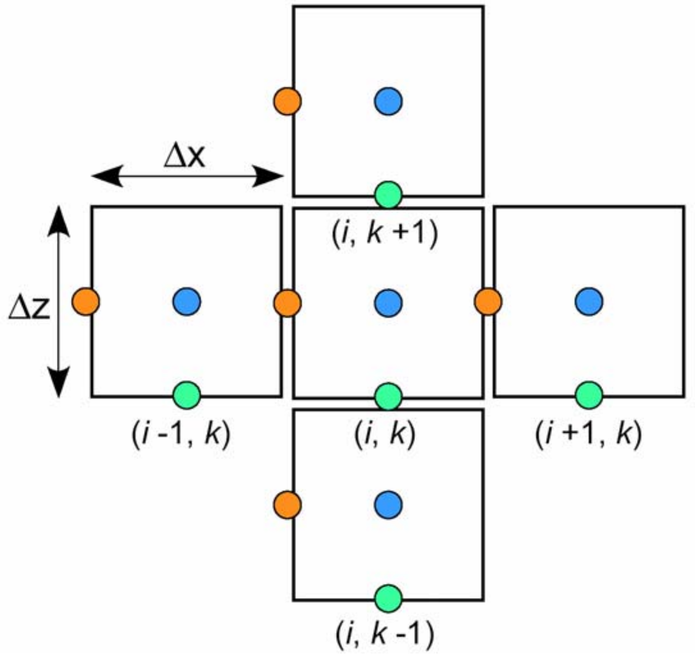

Figure 2-5: Staggered grid in x- and z- directions illustrating indexing on left side and bottom of control volume.

One alternative to the rectangular grid is the staggered grid shown in Figure 2-4 and Figure 2-5. This method involves several matrices to describe the properties previously assigned to the nodes in the center of the control volumes. Temperature, pressure, and phase fraction (defined with blue nodes) remain defined in the center of the control volume. However, those parameters that are best defined between pressure or temperature nodes at the left and right boundaries such as *x*-permeabilities, *x*-conductivities and *x*-velocities are defined on a new matrix that is shifted to the left by half a grid space (red nodes) so that they lie right on the *x* boundary. The same is true for the parameters that must be accounted for on the upper and lower boundaries of the control volume. This refers to the *z*-permeabilities, *z*-conductivities and *z*-velocities which are defined on a new matrix that is shifted down by half a grid space (green nodes) so that they lie right on the *x* boundary.

By using the staggered grid, the code is able to incorporate a much finer mesh and is able to ensure continuity at every control volume using velocity components from adjacent nodes. Also, the pressure drop between adjacent cells becomes the natural driving force for the velocity that is calculated between them at the face of the control volume of the adjacent cell [20].

2.5 Fluid Dynamics Discretization

By implementing the finite volume method instead of the finite difference method, the code is able to accept interfaces where medium properties undergo a step change. An example of this is the step transition from a channel in the manifold to the offset strip fin region of the heat exchanger. When analyzing the liquid side of the IHX the assumption of constant liquid density can be justified. For this case, conservation of mass in finite volume of fluid reduces to the very simple summation of liquid velocities at the boundaries of this finite volume as shown below:

$$u_{in} - u_{out} + w_{in} - w_{out} = 0$$

Equation 2-2

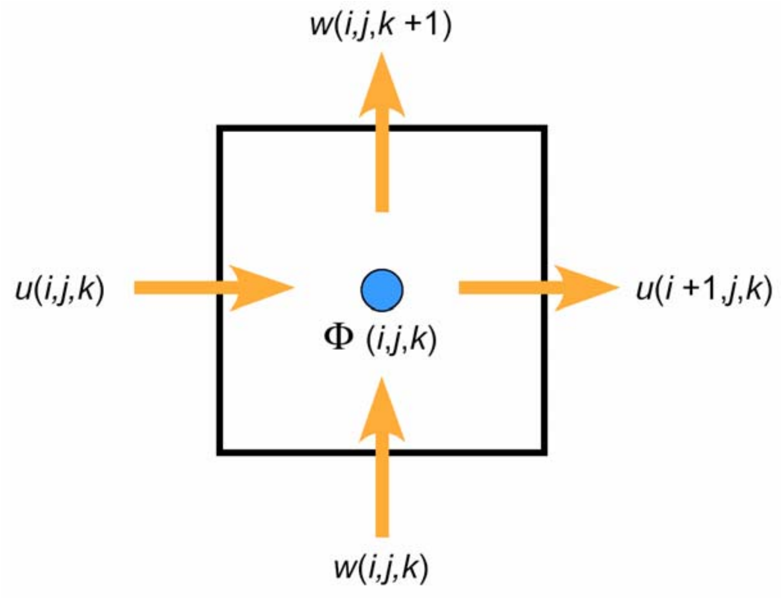

Figure 2-6: Continuity in a finite volume analysis for a fluid with constant density.

The case for temperature-dependent fluid properties is slightly more complicated, but important when dealing with a fluid that expands significantly when undergoing a significant temperature change. Accommodating the temperature-dependent helium density requires recalculating it at the local temperatures. The mass balance shown below in Equation 2-3 includes density.

$$\rho_{i-1,j,k}u_{i,j,k} - \rho_{i,j,k}u_{i+1,j,k} + \rho_{i,j,k-1}w_{i,j,k} - \rho_{i,j,k}w_{i,j,k+1} = 0$$

Equation 2-3

While the mass balance above depicts velocity, in CHEETAH the velocity is replaced by a discretized form of Darcy's transport equation such that the velocity terms actually introduce temperature-dependent viscosity, location-specific permeability and surrounding pressures as shown below in Equation 2-4:

$$-\frac{\rho_{i,j,k}k_{x\_i,j,k}}{\mu_{i,j,k}}\left(\frac{\Phi_{i,j,k}-\Phi_{i-1,j,k}}{\Delta x}\right)+\frac{\rho_{i+1,j,k}k_{x\_i+1,j,k}}{\mu_{i+1,j,k}}\left(\frac{\Phi_{i+1,j,k}-\Phi_{i,j,k}}{\Delta x}\right)\cdots$$

$$-\frac{\rho_{i,j,k}k_{z\_i,j,k}}{\mu_{i,j,k}}\left(\frac{\Phi_{i,j,k}-\Phi_{i,j,k-1}}{\Delta z}\right)+\frac{\rho_{i,j,k+1}k_{z\_i,j,k+1}}{\mu_{i,j,k+1}}\left(\frac{\Phi_{i,j,k+1}-\Phi_{i,j,k}}{\Delta z}\right)=0$$

Equation 2-4

Incorporating this into the discretization is complicated slightly by deciding which density values to use with each velocity. This is important both in the mass and energy balance in order to maintain stability. Unlike velocity, which is defined at the volume boundary, density is defined by the temperature of the cell which is in turn defined at the center or node. It is important that the mass entering the cell have the density of the cell from which it is departing. This is seemingly simple, but when fluid can be moving in any direction the code must be able to adapt and use the appropriate density depending on the sign of the velocity. The correct values have been assigned below in Figure 2-7.

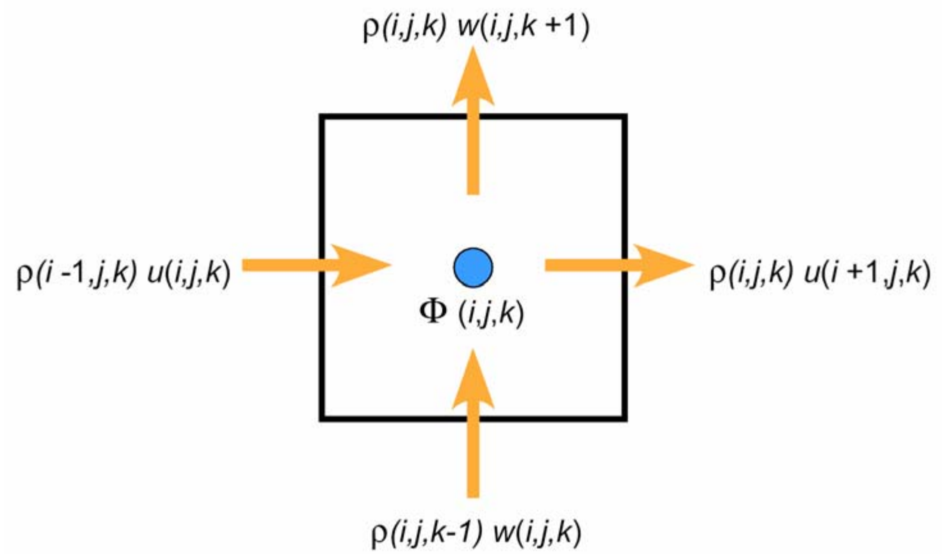

Figure 2-7: Continuity in a finite volume analysis for a fluid with variable density.

2.6 Heat Transfer Discretization

After the fluids module determines the velocity distributions in the axial (*x*) and cross-flow (*z*) directions, the thermal module of the IHX code applies an energy balance using a similar finite volume analysis (FVA) or control volume analysis as discussed previously in the fluid mechanics sections. Here too, the differential equations stemming from the energy equation were initially solved using the finite difference method (FDM) with Taylor-series approximations, until severe instabilities were encountered when modeling the consolidated IHX (manifolds and OSF section), which includes many zones with properties that vary spatially and abruptly. In fact, the energy balance was at first performed assuming constant thermophysical properties, but by using FVA the thermophysical properties are free to vary with local temperature and pressure, and the result is still highly stable.

The energy balances on a finite volume in each phase are presented below (Figure 2-8, Figure 2-9, and Figure 2-10) using pressure and temperature-dependent density for the gas.

2.6.1 Control Volume for Liquid Phase in the IHX

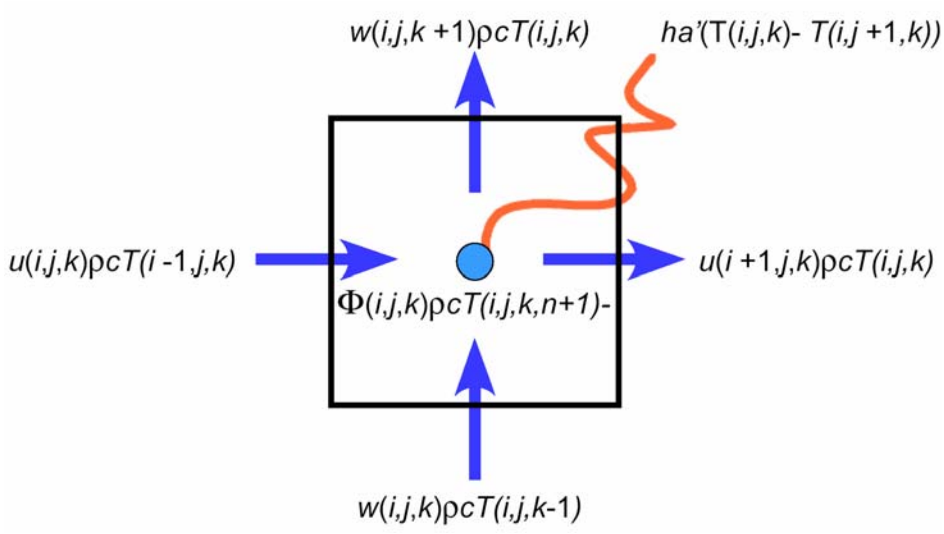

Figure 2-8: Energy balance in the finite volume analysis for a fluid with constant density.

2.6.2 Control Volume for Solid Phase in the IHX

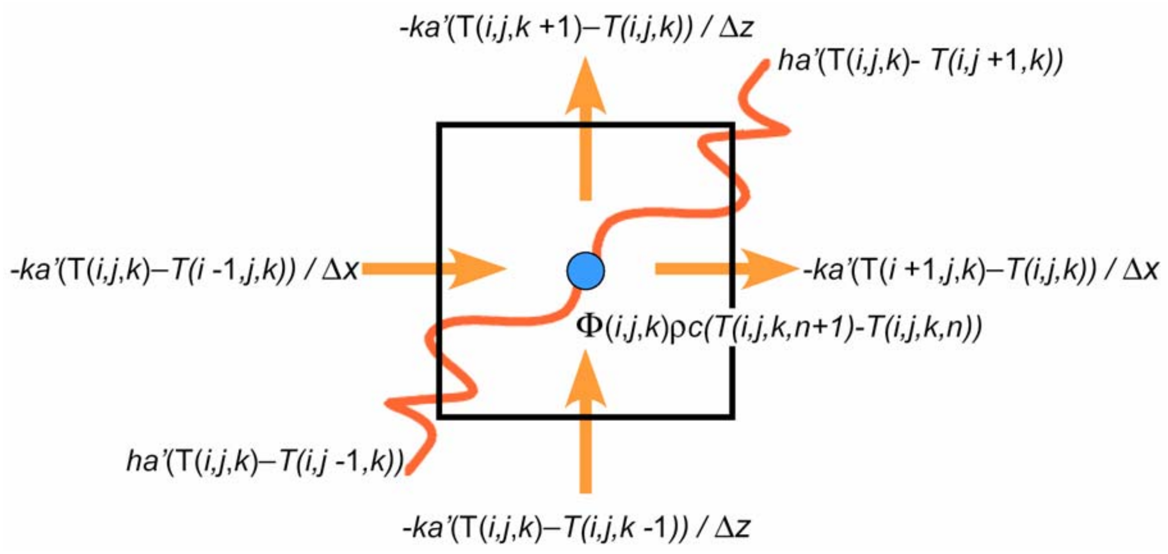

Figure 2-9: Energy balance in the finite volume analysis for the solid exchanging heat with separate fluids and conducting heat from its surroundings.

2.6.3 Control Volume for Gas Phase in the IHX

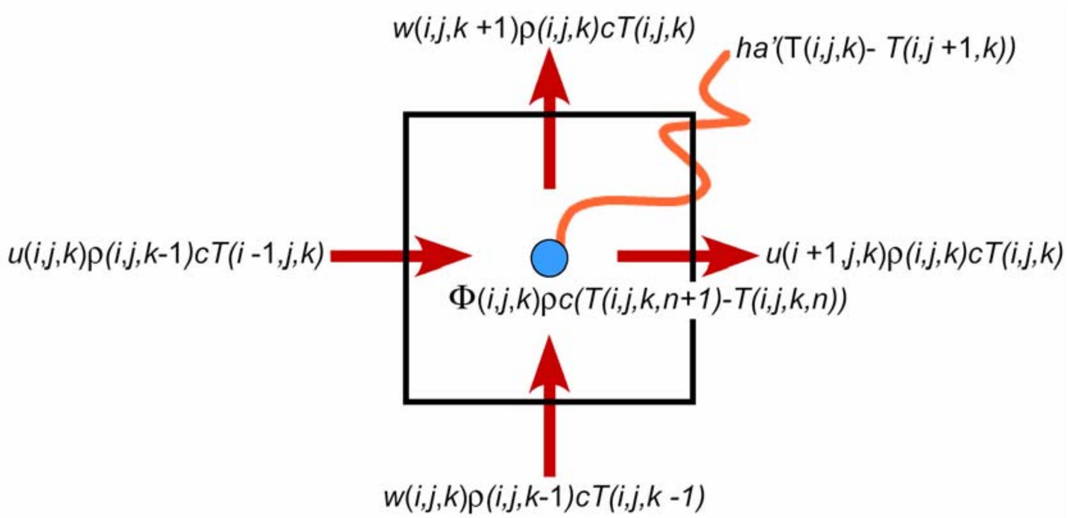

Figure 2-10: Energy balance in the finite volume analysis for a fluid with variable density.

Chapter 3

Thermal Hydraulic Results

This chapter presents thermal hydraulic results from analyses from the Compact Heat Exchanger Thermal and Hydraulic (CHEETAH) code using both constant and temperature-dependent thermophysical properties. The analysis includes steady-state plots of pressure, velocity, and temperature for both constant and temperature-dependent thermophysical properties for comparison. Transient thermal hydraulic results are also presented for the case of constant thermophysical properties.

3.1 CHEETAH Code Architecture

The CHEETAH code consists of five modules. Each module executes code that either assigns system characteristics, thermal hydraulics parameters, or performs the finite volume analyses presented in the previous chapter. The modules are described in Figure 3-1 below.

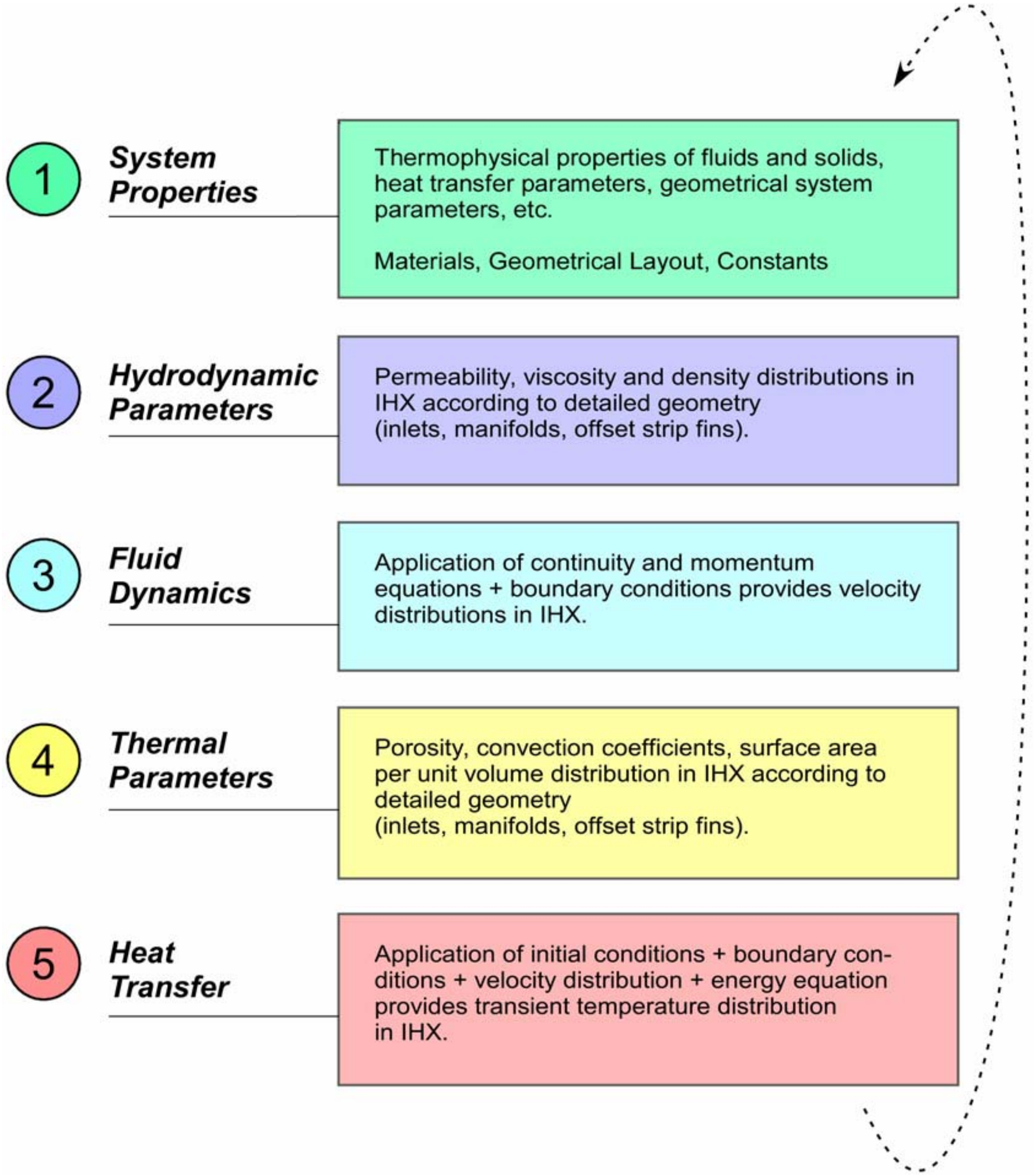

Figure 3-1: Five modules executed sequentially comprise the CHEETAH code.

For the case of constant thermophysical properties, CHEETAH proceeds with modules one through five in that order and yields results for the steady-state or transient temperature distribution. If the analysis includes temperature-dependent thermophysical fluid properties, then the steady-state temperature distribution is obtained by running modules one through five and the resulting temperature distribution used to find distributions in the thermophysical properties. Subsequently pressure and velocity distributions are again calculated by executing modules two through five with new thermophysical properties. In theory, the best solution would be obtained by implementing modules two through five at every time step in module five, since that would apply the most recent temperature data to the thermophysical properties, but the computational time would be exorbitant. The frequency with which thermophysical properties and fluid dynamics are updated is set by the user. In the analysis for temperature-dependent thermophysical properties presented later, the steady-state distribution is used to set thermophysical properties and fluid dynamics.

3.2 Thermal Hydraulic Results with Constant Thermophysical Properties

The thermal hydraulic results from CHEETAH using constant thermophysical properties are presented because they help benchmark the effect and importance of including temperature-dependent thermophysical properties in the finite volume analysis (FVA) used in CHEETAH. For the following results the viscosity of both fluids is evaluated at each fluid's median temperature (half-way through the OSF region) through the IHX. The change in density of the liquid salt is not significantly affected by temperature and thus will be treated as constant in this analysis. The density of helium will be evaluated at the fluid's median temperature and pressure through the IHX. An analysis where the thermophysical properties are allowed to vary locally with temperature is presented later in this chapter.

3.2.1 Liquid Pressure Distribution

The steady-state pressure distributions are solved using the fluid mechanics module of CHEETAH which applies the iterative FVA technique, presented in Chapter 2, to solve for the pressure distribution in the composite plate. The pressure distribution for the liquid side of the composite plate is shown in Figure 3-2.

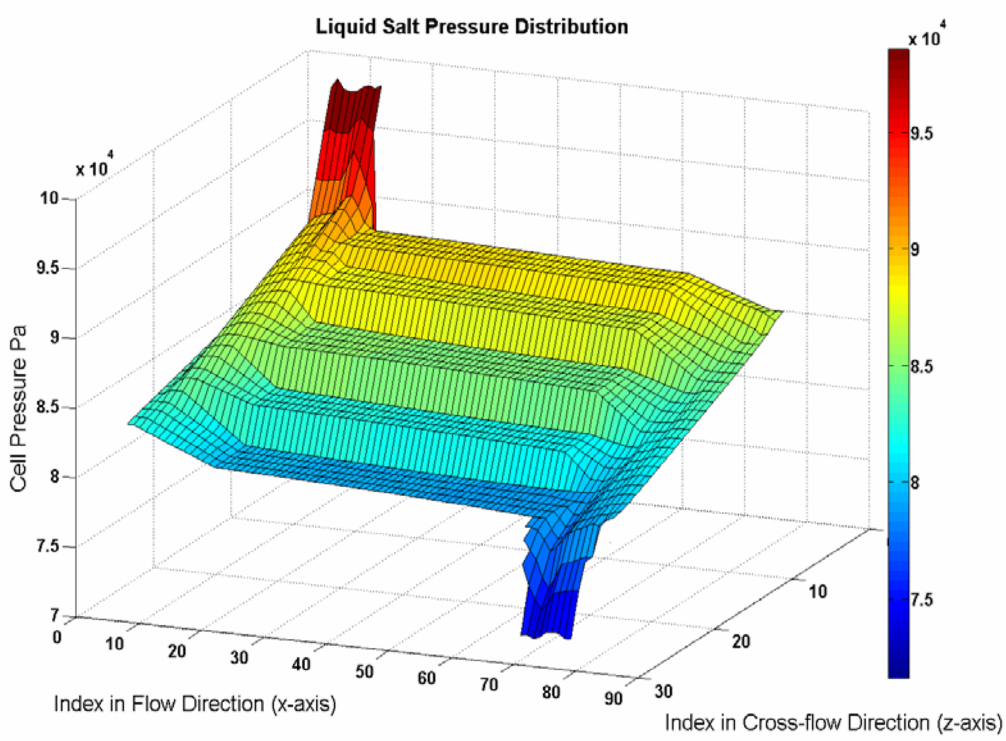

Figure 3-2: The steady-state liquid salt pressure distribution through the composite plate of the IHX.

The shape of the pressure gradient over the IHX clearly denotes areas with different permeabilities and delineates the interfaces where the permeability changes. Changes in the pressure gradient can be seen where the OSF sections meet the inlet and outlet manifold producing an edge in the distribution. This identifies the interface without the instabilities created when analyzed with the Taylor-series based finite difference techniques. The zones nearest the inlet and outlet ports in Figure 3-2 show that most of hydraulic head is depleted in the distribution channels between the inlet port and the offset strip fin (OSF) region. This configuration is specified because the higher flow resistance in the flow distributor channels allows the determination of the flow going into each zone within the OSF section and which may be altered by changing the flow resistance in the distribution channels leading to and following any zone in the OSF section. The index on the x and z axis represent the number of finite volumes with each index locating a finite volume cube that measures 2 cm on each side.

3.2.2 Gas Pressure Distribution

The pressure distribution in the gas side of the composite plate is readily obtained when using constant thermophysical properties. The permeabilities in both the flow and cross-flow directions through the center of the gas side of the composite plate are constant. The constant permeabilities in this region result in a linear helium pressure distribution through the plate. The helium pressure distribution for constant density and viscosity is shown in Figure 3-3.

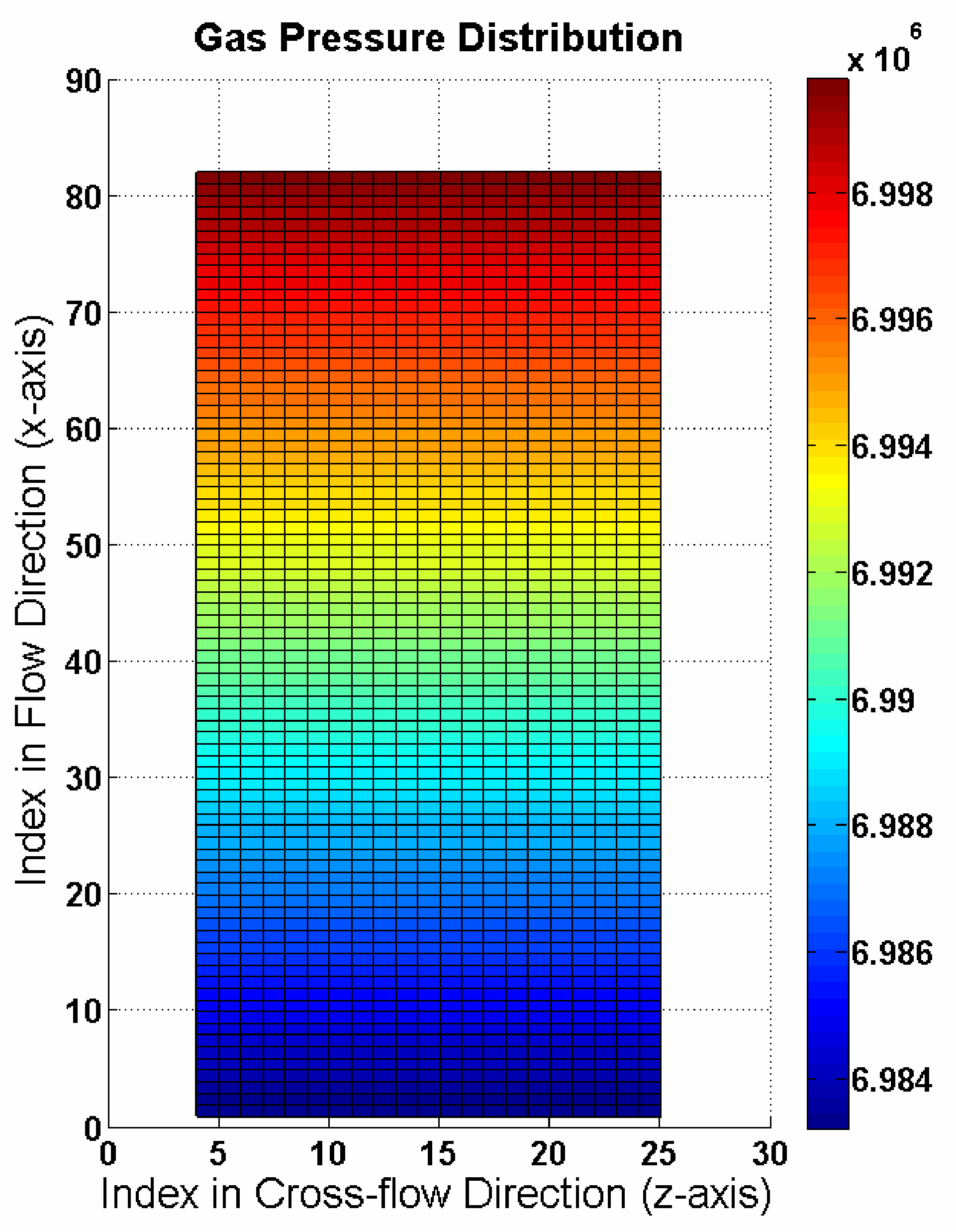

Figure 3-3: The steady-state helium pressure distribution through the composite plate of the IHX.

3.2.3 Liquid Speed Distribution

The complex liquid side pressure distribution drives flow through the different permeability zones on the liquid side of the composite plate. The square root of the sum of the squares of the velocity components in the *x*- and *z*-direction at every staggered grid provides a non-directional total fluid speed distribution in the liquid plate of the IHX. The liquid flow speed distribution is shown in Figure 3-4.

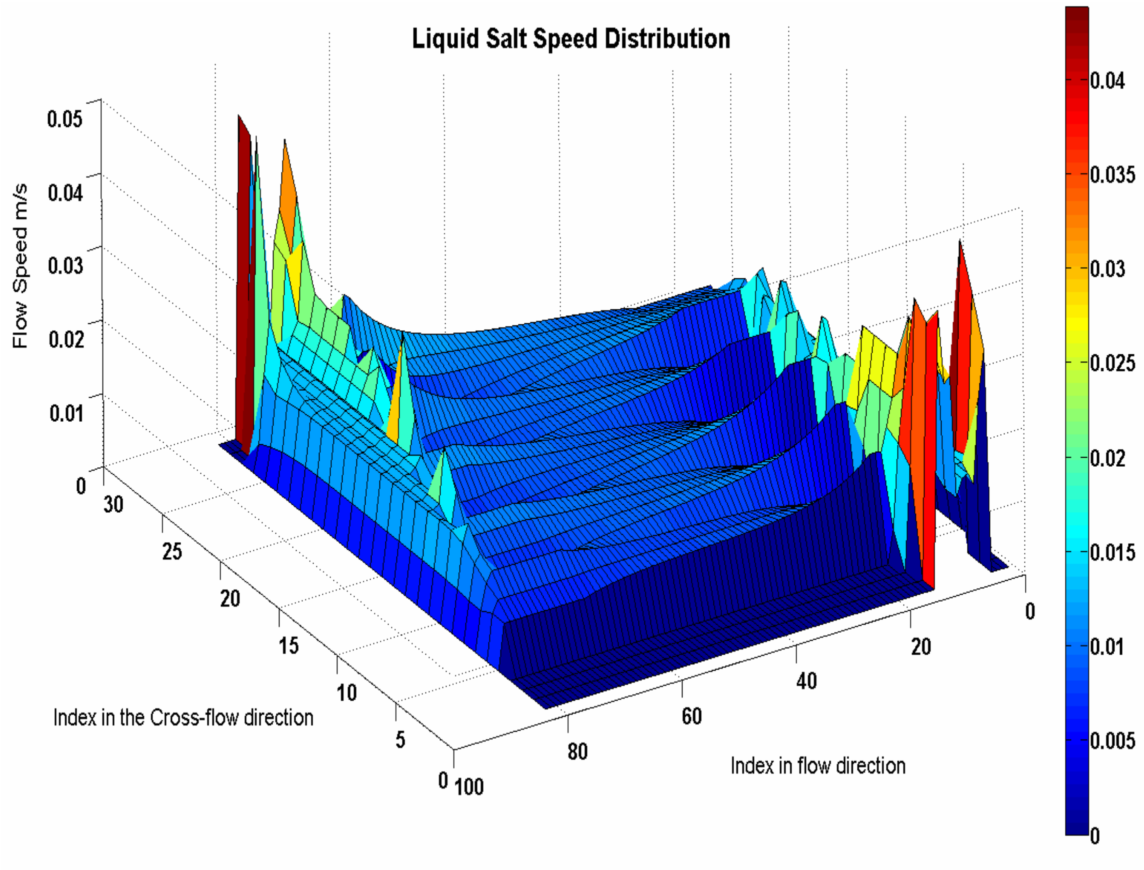

Figure 3-4: Flow speed distribution of liquid salt through the composite plate of the IHX.

Midway through the OSF region the flow rate is shown to be uniform across the width of each flow zone. However, near the entrance and exit of the OSF region the flow is skewed with higher flows on the inside of the turn in the distributor channels. This is expected since the inside turn in the distributor presents a shorter path and therefore less resistance to flow. Changes to the effective permeabilities of the various zones containing the distribution flow channels can be made to ensure the flow is symmetric and uniform through the OSF region. Outside the flow zones, the speed is flat at zero indicating that this is not a flow region.

3.2.4 Gas Speed Distribution

The flow distribution for the gas side of the complex plate is simple for the case of constant thermophysical properties. The fixed pressure gradient combined with constant permeability produces a uniform flow speed of helium across the OSF region of the IHX as is shown in Figure 3-5.

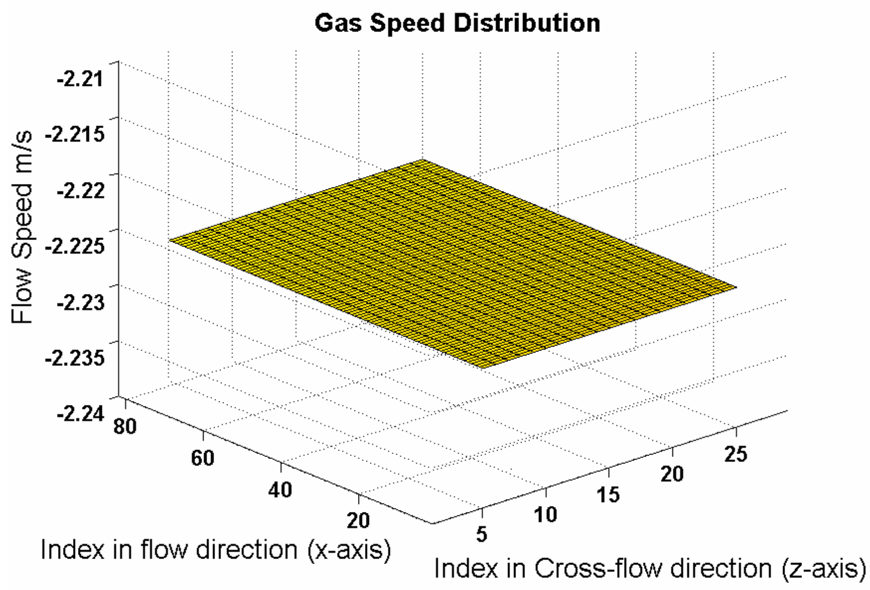

Figure 3-5: Flow speed distribution of gas through the composite plate of the IHX.

3.2.5 *Steady-State Temperature Distribution*

The liquid and gas flow fields through the composite plate provide the advective contributions to the energy balance of each cell in the IHX. When combined with initial distributions of temperature, directional conductivity, convection, porosity, and surface densities for each side of the composite plate, CHEETAH can solve for a steady-state temperature distribution and for the heat exchanger's thermal effectiveness. For constant thermophysical properties the steady-state temperature distribution for the composite plate is shown in Figure 3-6.

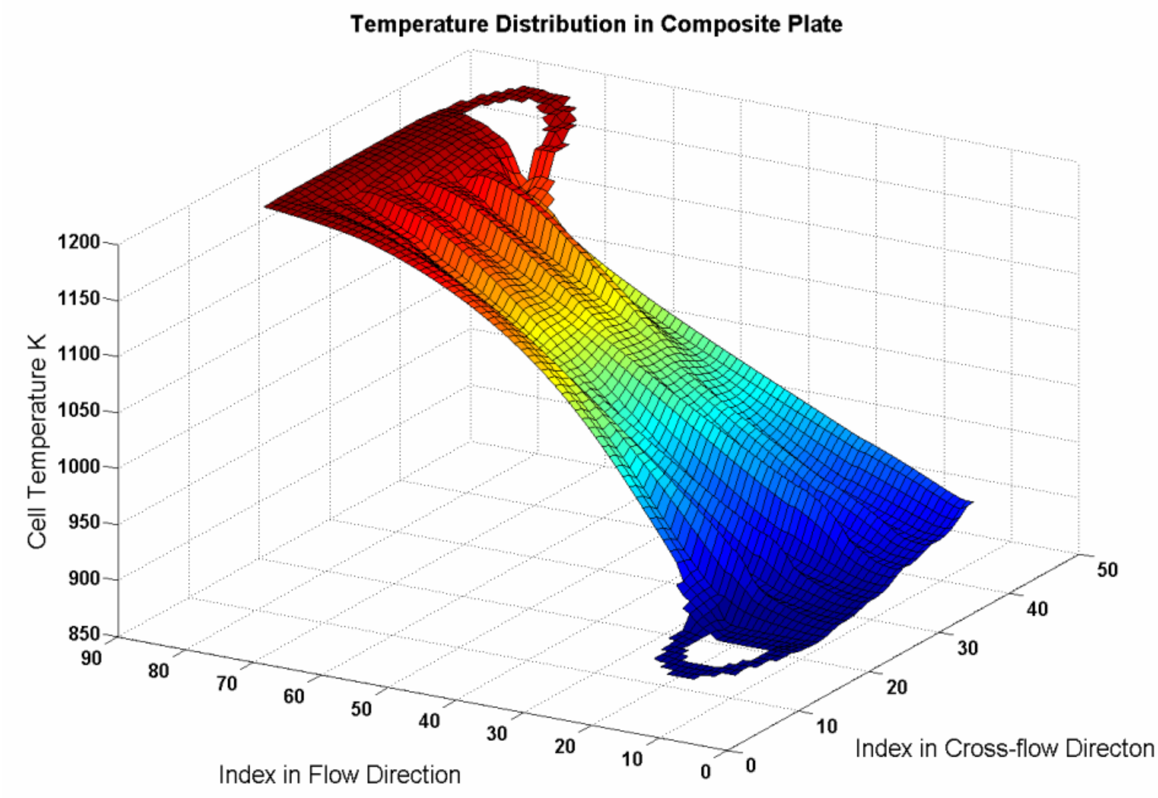

Figure 3-6: Steady-state temperature distribution solved by CHEETAH for the composite plate of the IHX.

Ridges in the temperature distribution can be seen in the OSF region of the IHX. These edges make the flow zone easy to identify in the OSF region. The sharp gradients in the temperature distribution are formed by discrepancies between the flow rates and flow paths in neighboring flow zones in the IHX. These are the same ridges that were discussed in Figure 3-4 showing the speed distribution; they help to demonstate the impact of minor variations in flow on heat exchanger performance.

3.2.6 Transient Temperature Distributions

Two thermal transients are considered in this analysis. One analyzes the transient temperature distributions that result from the interruption of liquid flow while the other concerns the interruption of gas flow to the IHX. In both cases the flow is instantaneously reduced to 2% of the steady-state mass flow rate. This reduced-flow value is arbitrary and is meant to put the IHX into a severe thermal transient. The simulation would be more representative of an operational scenario if it included a gradual pump coast down resulting in a ramped reduction of flow rather than a stepped reduction. The CHEETAH code is capable of executing any flow ramp down but doing so would require empirical pump coast-down data from a specific pump. A more severe transient results with a step change in flow.

The transient is assumed to begin from a steady-state operation condition and the temperature distribution of the composite plate of the IHX is examined. In both cases, a similar transient could occur from a severe pump or valve failure in a power plant. The transient analyses presented here were analyzed using CHEETAH using constant thermophysical properties where the IHX is assumed to be in a horizontal arrangement. If the IHX were to be modeled in a vertical arrangement the more complicated effects of natural circulation would need to be modeled as well. In each case it is assumed that one fluid experiences a step change in flow while the counter-flowing fluid continues to flow unhindered. This further increases the severity of the thermal transient on the resulting mechanical stresses. The CHEETAH code solves for the temperature profiles in the composite plate as a function of time and the results for both transients can be seen below.

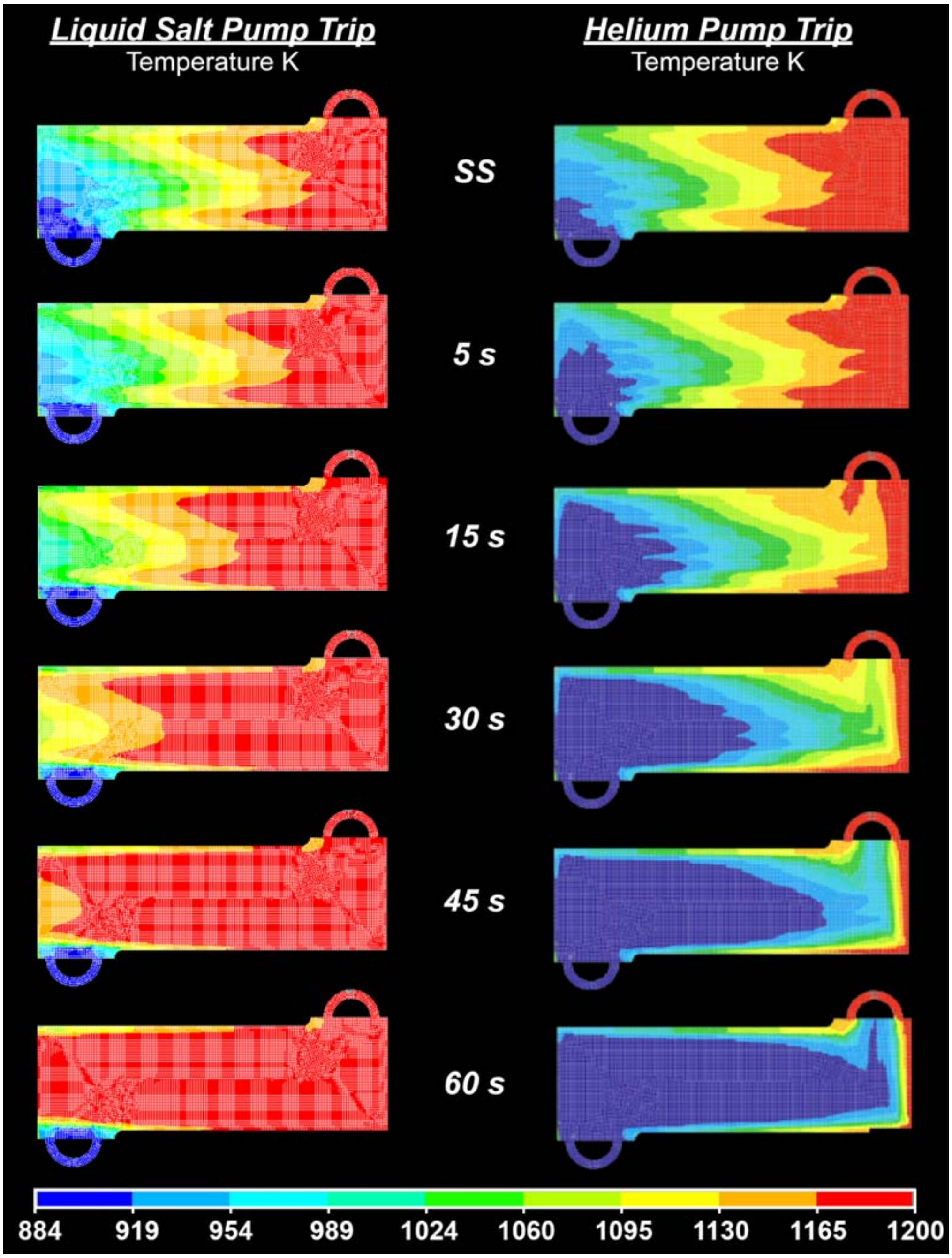

Figure 3-7: Transient temperature distributions solved by CHEETAH for the composite plate of the IHX after a step change in flow rate initiates a thermal hydraulic transient.

The thermal hydraulic transient begins from a steady-state temperature distribution in both cases. The steady-state temperature distribution is marked SS in Figure 3-7. The contours marking the temperature gradients show a lack of symmetry in the temperature distribution, which are shown clearly near the liquid salt (cold fluid) inlet on the bottom left of the heat exchanger in the plot marked SS. In the steady-state plots the temperature profiles follow the cold fluid (liquid salt) flow directions in the colder left-hand side of the IHX. The hotter (right-hand) side of the composite plate is clearly dominated by the ingress of hot helium to the point that temperature gradients are not visible near the liquid salt outlet port which is within 35 K of the inlet temperature.

In the liquid salt pump trip transient the colder liquid salt is instantaneously reduced to 2% of its original flow rate while the hotter helium flow continues. The five second graph (5 s) shows all temperature profiles for the liquid salt pump trip advance leftward; after 30 seconds (30 s) from the initiating liquid salt pump trip the shape of these temperature fronts change slightly as they encounter regions of the composite plate with varying temperatures. After roughly 60 seconds (60 s) the new steady-state profile is generally in place. The small cold region near the liquid salt inlet will remain within 35 K of the liquid salt inlet temperature due to the residual post-transient flow (2% of initial flow rate) entering the composite plate. The phenomena associated with this residual flow could be representative of buoyancy effects in other parts of the intermediate loop or in a vertically-oriented IHX.

The progression of the temperature fronts along the more complicated liquid salt flow paths in the composite plate is clear in the helium pump trip transient shown on the left side of Figure 3-7. In the temperature plot at 15 seconds after the initiation of the thermal hydraulic transient, the different flow sections through the OSF region can be seen as fingers (three are visible) in the temperature gradients moving through this region. After 60 seconds, the cold front can be seen turning left towards the outlet in the distribution channels of the composite plate. On the right-hand side of the composite plate, the edge can be seen to remain very hot as the residual 2% mass flow rate of helium continues to enter the composite plate. These temperature gradients will produce differential expansion in the plate which will in turn lead to transient mechanical stresses. The magnitude and repercussions of these stresses will be analyzed in the next chapter.

3.3 Thermal Hydraulic Results with Temperature-Dependent Thermophysical Properties

3.3.1 Temperature-Dependent Thermophysical Properties

To illustrate the variation of the temperature-dependent thermophysical properties over the composite plate, the spatial variation of several of these properties is plotted using the temperature distribution solved on the composite plate with constant thermophysical properties. The viscosity of liquid salt is a strong function of temperature, as shown in Equation 1-33, in Chapter 1. The resulting spatial variation for the liquid salt's viscosity based on the steady-state temperature distribution is shown in Figure 3-8.

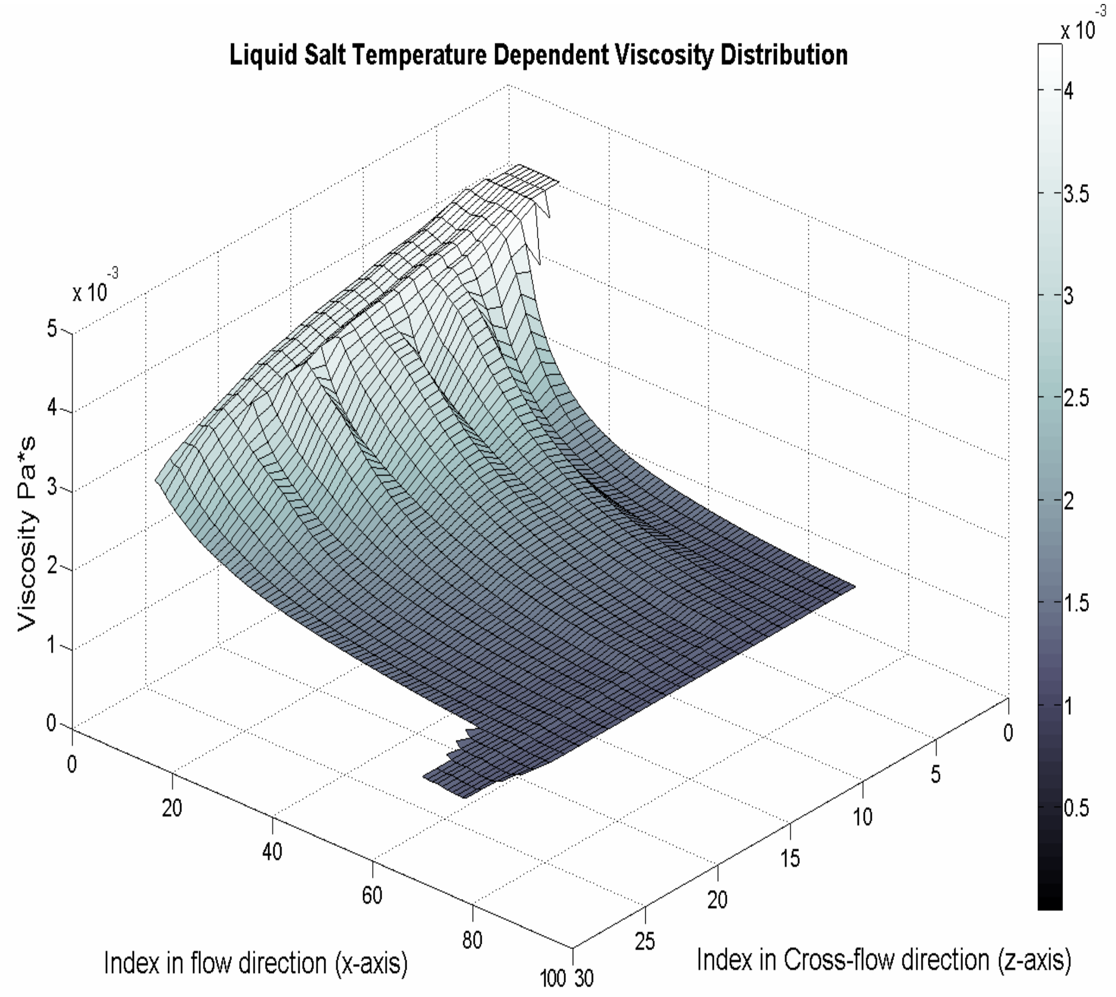

Figure 3-8: Liquid salt viscosity distribution solved from steady-state temperature distributions from the composite plate.

The viscosity of this liquid salt varies by a factor of six from inlet to outlet. A variation of this magnitude will have significant effects on flow distribution, making it important to include the variability of this parameter in any analysis that evaluates temperature distribution and thermal effectiveness.

For this example, the temperature distribution creates a variation in the viscosity of helium that is more moderate than that of the liquid salt. The viscosity drops 20% as the helium temperature decreases from the inlet to the outlet of the composite plate. This behavior is inverse that of the liquid salt where the viscosity drops with increases in temperature. The resulting viscosity distribution for the steady-state temperature distribution solved earlier is shown in Figure 3-9.

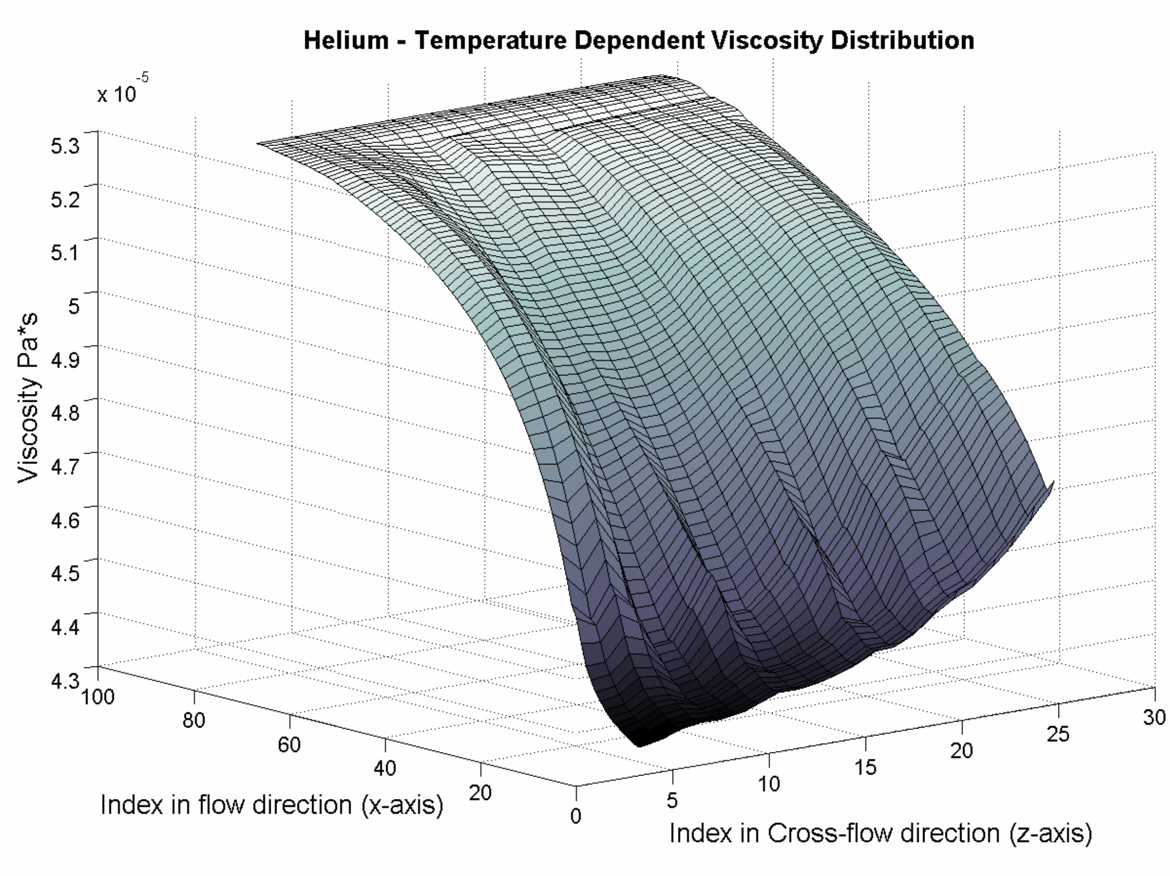

Figure 3-9: Helium viscosity distribution solved from steady-state temperature distributions from the composite plate.

It is particularly interesting to see the imprint of the temperature distribution in all of the thermophysical properties. These figures serve as clear reminders of how tightly coupled this three-phase system is.

The helium density is the last thermophysical property to be considered in this temperature-dependent model. In this case, the density of helium can be modeled to more than 1% accuracy through the ideal gas law compared with values published in the NIST web book [16]. Changes in the density of helium while flowing through the composite plate will affect the fluid velocity distribution. The variation of helium density with temperature can be seen in Figure 3-10.

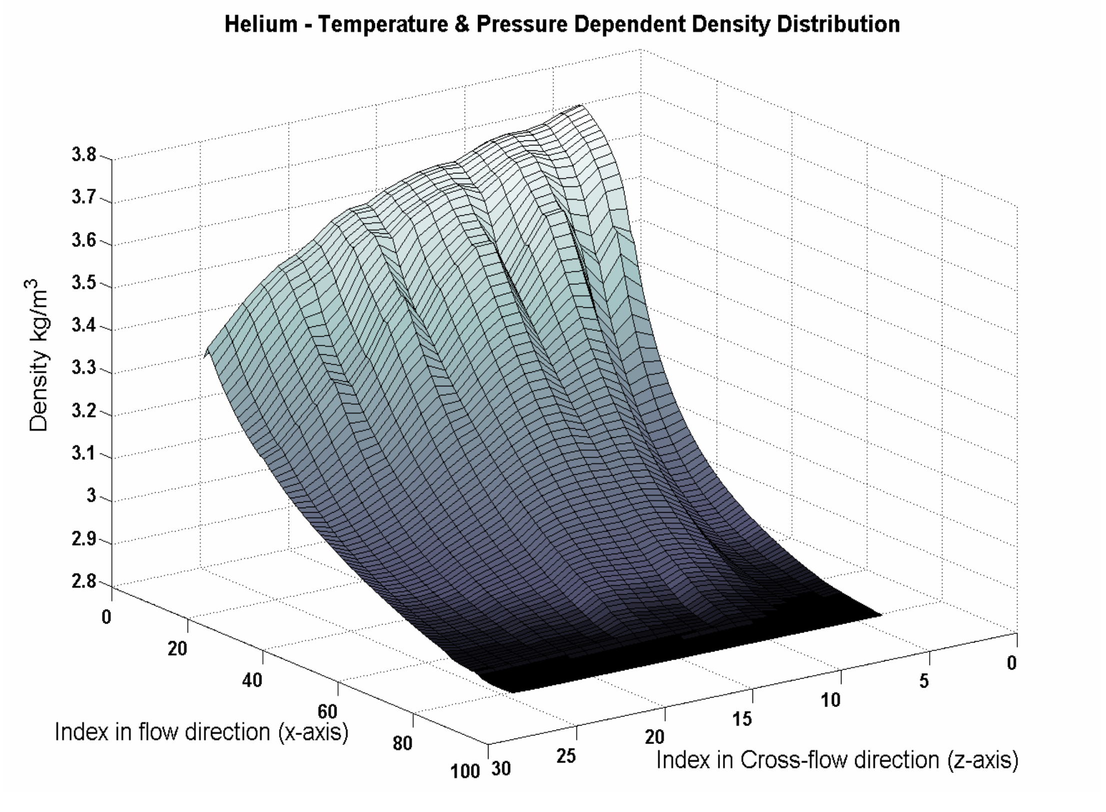

Figure 3-10: Helium density distribution solved with ideal gas law with steady-state temperature and pressure distributions from the composite plate.

3.3.2 Liquid Pressure Distribution

The steady-state pressure distributions are solved by the fluid mechanics module of CHEETAH considering liquid salt's viscosity variation with temperature. The code can be set to recalculate the viscosity distribution based on the current temperature distribution as often as necessary. The more often the thermophysical properties are updated with the temperature distribution, the more accurate the flow distribution will be, but the longer the code will take to find the steady-state flow distribution. The pressure distribution for the liquid side of the composite plate is based on temperature-dependent thermophysical properties, which are in turn based on the temperature distribution found in the previous section. The resulting pressure distributions are shown in Figure 3-11.

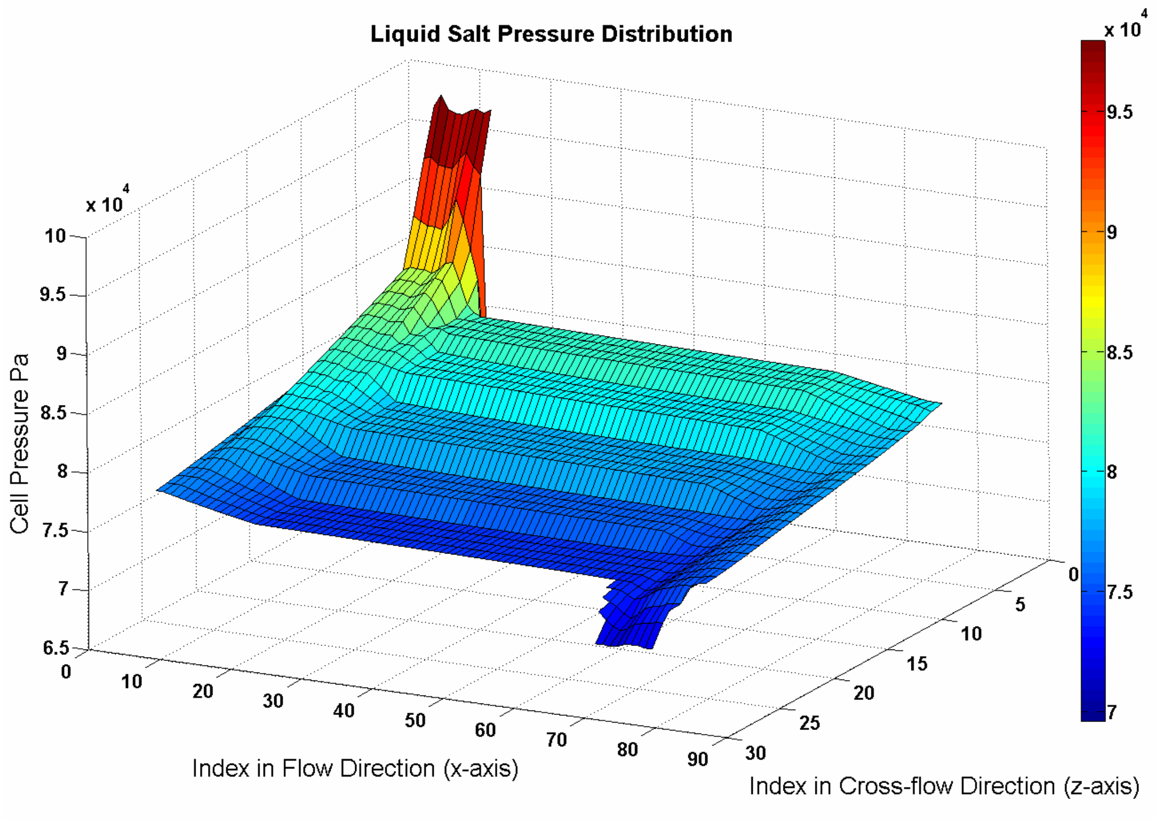

Figure 3-11: The steady-state liquid salt pressure distribution through the composite plate of the IHX with temperature-dependent thermophysical properties.

The liquid salt inlet can be found in Figure 3-11 because it has the highest pressure and is shown in red near coordinates (0,0). The liquid salt outlet manifold, shown in blue, has the lowest temperature and is located near coordinates (75,25) in Figure 3-11. Comparing Figure 3-11 with Figure 3-2 for constant thermophysical properties reveals that roughly three times the hydraulic head occurs near the inlet when viscosity is allowed to vary with temperature than when it is held constant. Clearly, using an average viscosity under-predicts the inlet pressure drop and over-predicts the outlet pressure drop.

The liquid salt distribution channels create a zone in the IHX that is not in counter-flow, but rather in cross-flow. Each of the flow channels covers a unique distance in the cross-flow region which means that the liquid salt in each channel reaches the OSF region at a different temperature. When measured from inlet to outlet all flow paths through the composite plate are ultimately the same length. This is because a long flow channel near the inlet eventually connects to a short flow channel near the outlet of the composite plate. However, the flow channels that take the longest path from the inlet to the OSF region traverse this path at much higher viscosity (due to the low temperatures near the inlet) and therefore more hydraulic head is lost than the very same distribution flow channels between the OSF and the outlet. In this case the long flow channels from the OSF to the outlet are traversed at higher temperature and thus at significantly lower viscosity, resulting in a lower head loss.

3.3.3 Gas Pressure Distribution

The pressure distribution in the gas side of the composite plate is simple when using variable thermophysical properties, just as when it is calculated with constant thermophysical properties. The permeability in both the flow and cross-flow directions through the center of the gas side of the composite plate are constant while the viscosity and density vary with temperature. The variation of these thermophysical properties is not apparent when examining the pressure profile because the changes in pressure are very mild compared to the total pressure drop from inlet to outlet. The resulting pressure distribution through the plate has a slight upward inflection due to the varying thermophysical properties, but this inflection is only apparent after close inspection on high resolution graphs. The helium pressure distribution for temperature-dependent density and viscosity is shown in Figure 3-12.

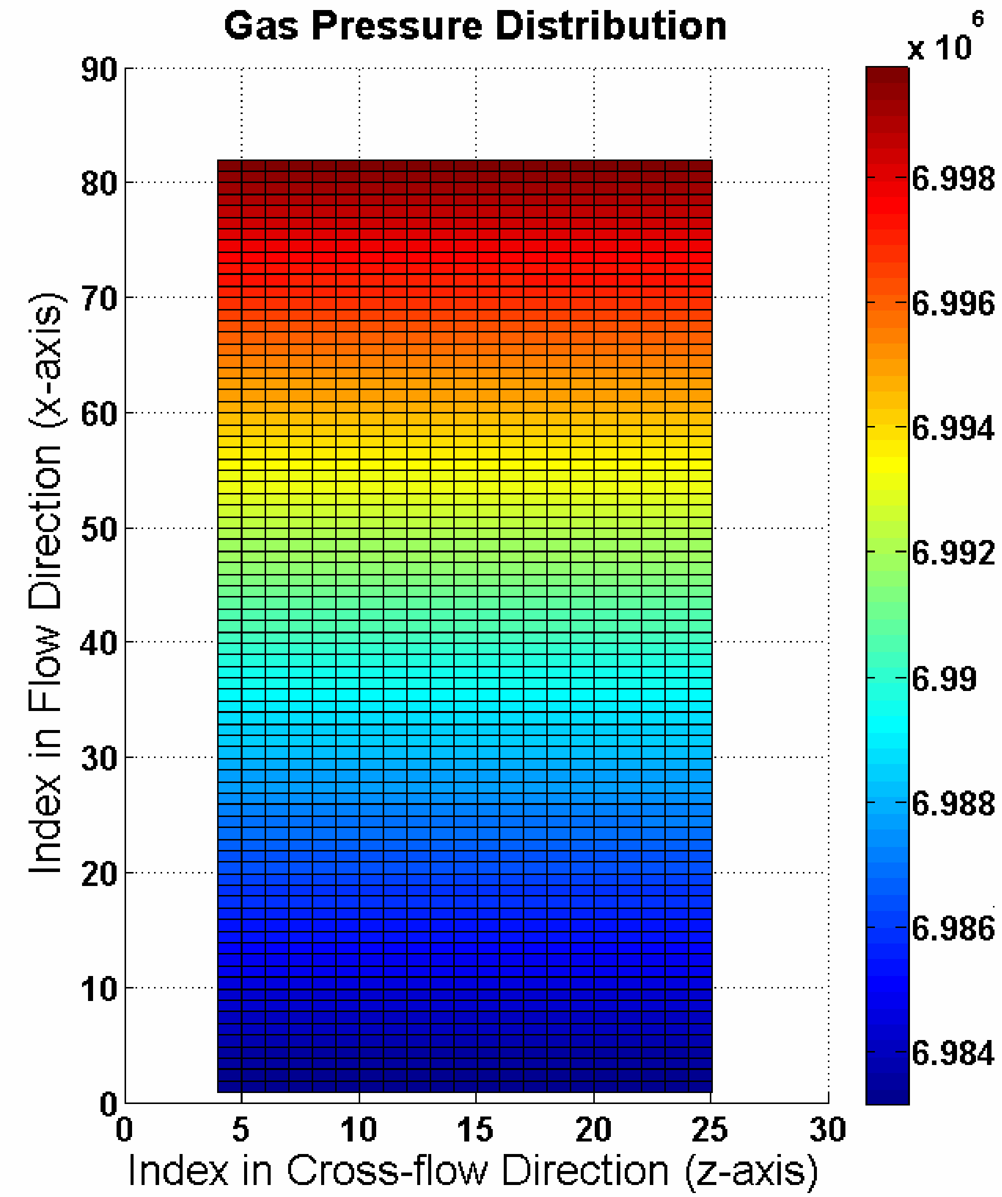

Figure 3-12: The steady-state helium pressure distribution through the composite plate of the IHX with temperature-dependent thermophysical properties.

3.3.4 Liquid Speed Distribution

The complex liquid side pressure distribution drives flow through the different permeability zones on the liquid side of the composite plate. The inlet is shown near coordinate (0,0) and the outlet lies near coordinate (75,30). Summing the x- and z-direction at every mesh provides a non-directional total fluid speed distribution in the liquid plate of the IHX. The liquid flow distribution in the composite plate is shown in Figure 3-13.

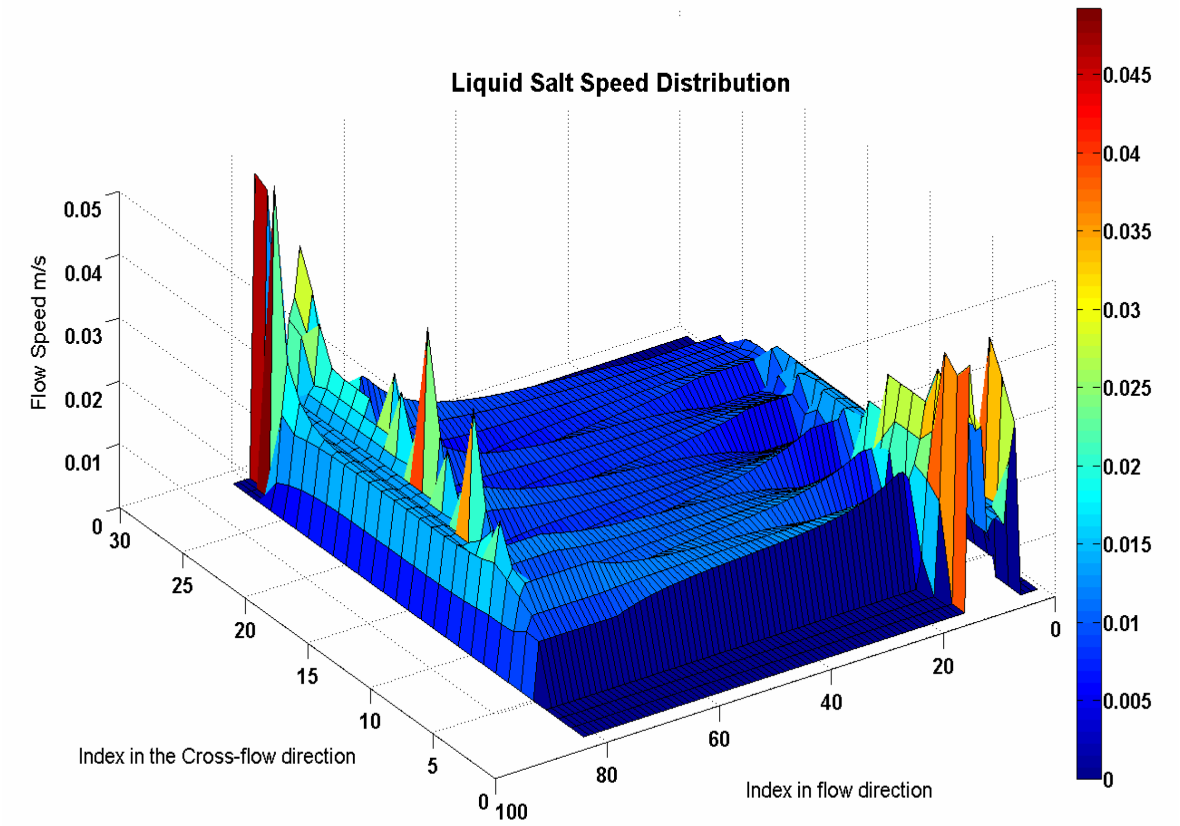

Figure 3-13: Flow speed distribution of liquid salt through the composite plate of the IHX with temperature-dependent thermophysical properties.

The flow rate through the OSF region is flat and relatively constant throughout the width of the IHX. Some peaks are visible where the inlet flow distribution channels turn 90° from the cross-flow direction to the flow direction. This is because the width of the zone containing the flow distribution channels in the cross-flow direction is narrower than the flow area in the primary flow direction. The step change in cross-sectional area causes some flow channels to narrow abruptly and then expand again at the border between zones, creating a localized nozzling effect. At the entrance to the OSF region the liquid can be seen to increase its speed in the vicinity of the inside corner of each flow section as it flows preferentially through the path of least resistance (in this case the shortest path being that which hugs the corner).

3.3.5 Gas Speed Distribution

The flow speed distribution of helium in the composite plate is shown in Figure 3-14.

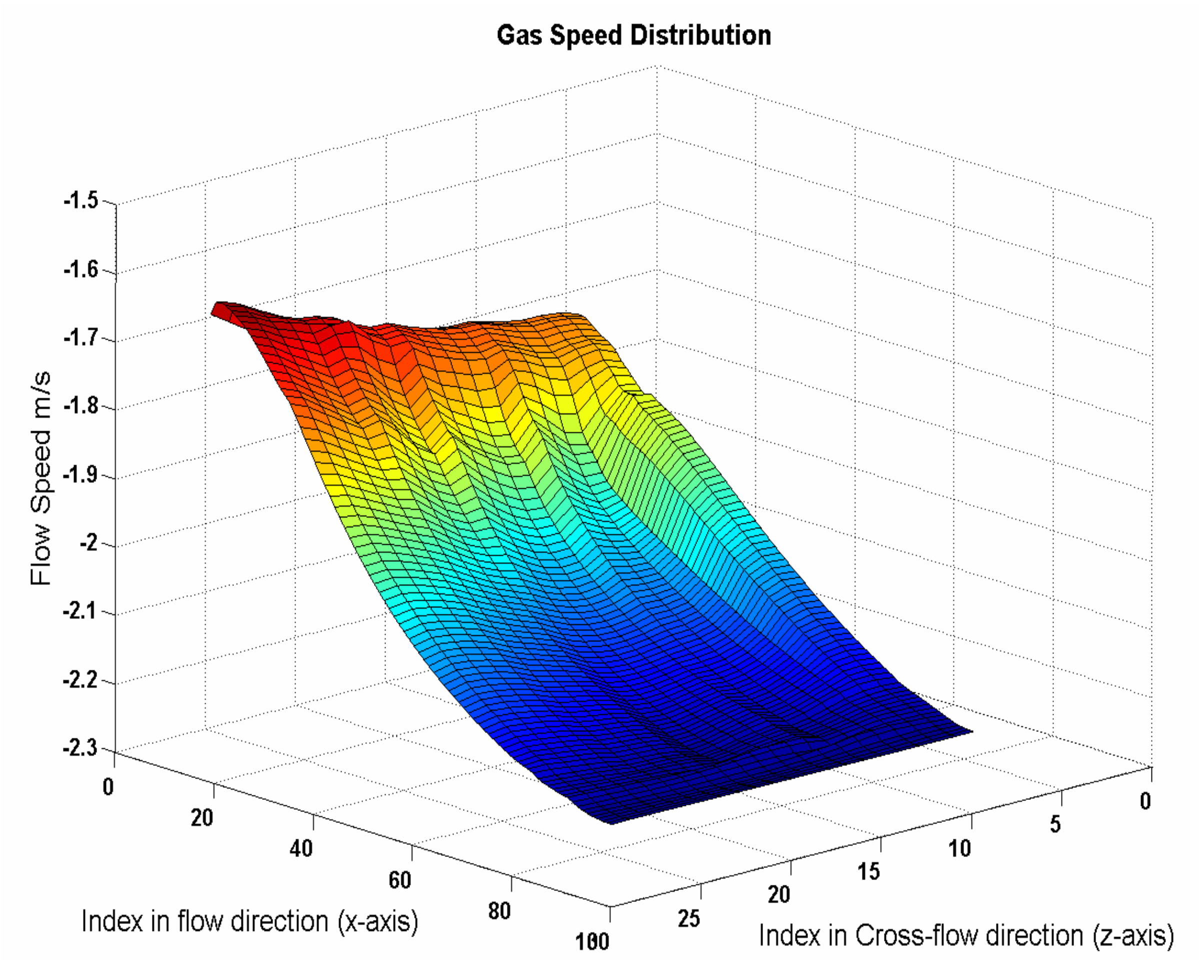

Figure 3-14: Flow speed distribution of gas through the composite plate of the IHX with temperature-dependent thermophysical properties.

The flow speeds on the gas side are indicated as negative because they flow counter to the direction of the coordinates and in counter-flow with the liquid salt. The effect of temperature-dependent thermophysical properties on the flow field is mild but noticeable nonetheless. The flow speed can be seen to increase by as much as 30% as the specific volume of helium increases with rising temperatures in the helium flow. The increase in speed would result in an increase in the Nusselt number of the flow and in increased heat transfer; but this effect is not included in this simulation because a constant Nusselt number is assigned based on an average flow velocity.

3.3.6 Steady-State Temperature Distribution

With the calculated temperature-dependent thermophysical properties and velocity distributions, CHEETAH solves for the steady-state temperature distribution for the composite plate which is shown in Figure 3-15.

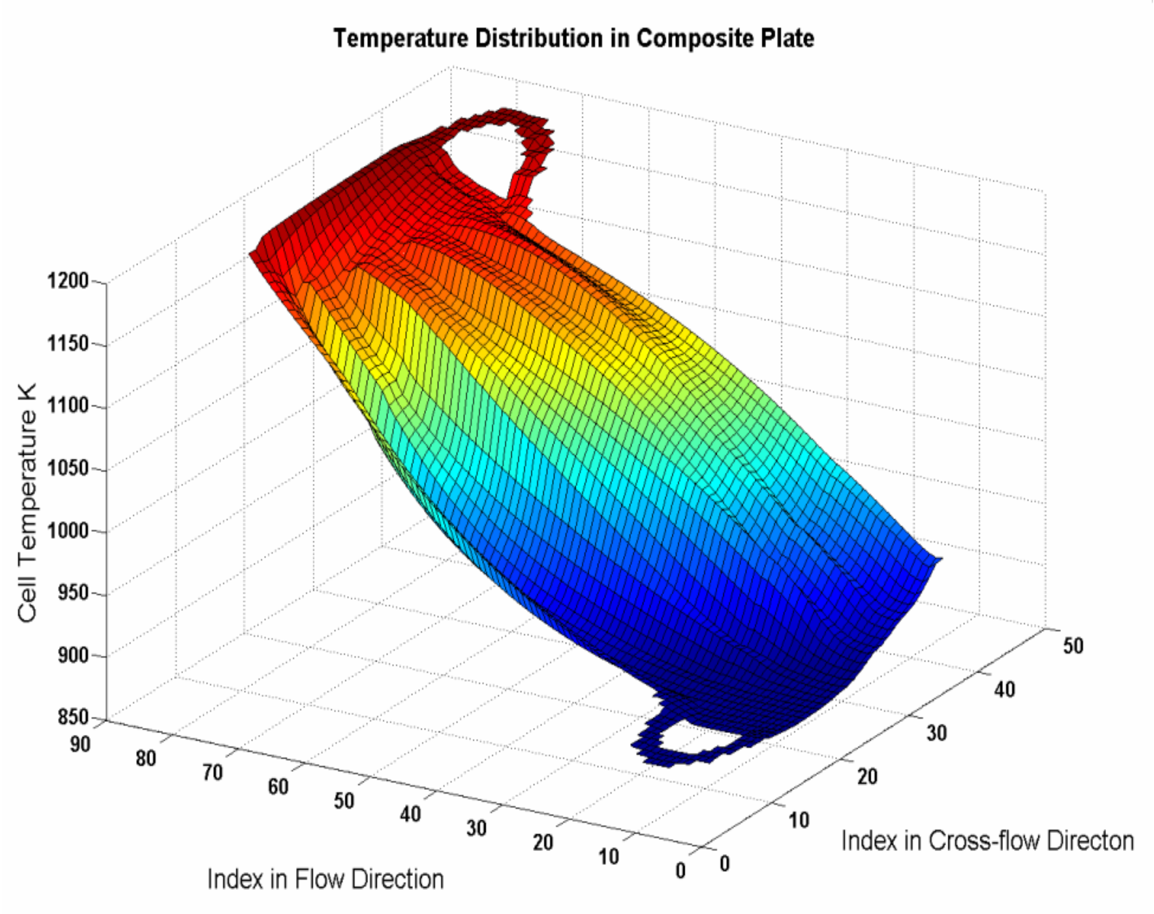

Figure 3-15: Steady-state temperature distribution solved by CHEETAH for the composite plate of the IHX with temperature-dependent thermophysical properties.

The results of changing from constant to temperature-dependent thermophysical properties can be seen more dramatically by comparing Figure 3-6 and Figure 3-15. This illustrates the significance of including this effect when determining the performance of a compact heat exchanger over a large temperature change. While the significant effects of temperature-dependent thermophysical properties are unique to applications that use fluids with relatively low volumetric heat capacity, the inclusion of these effects always result in more complex flow distributions. This effect seems particularly important when gases are used as coolants (such as in high temperature helium-cooled modular reactors) because local hot spots increase the gas viscosity and therefore decrease the flow in that area. Effective simulation pertaining to the safety and efficiency of thermal equipment involving gas coolants depends on the inclusion of temperature-dependent thermophysical properties.

Chapter 4

Verification of Numerical Method

Modeling the transient response of a three-phase system in two spatial dimensions undergoing changes in flow rate represents a problem too complex to approach analytically. The lack of an analytical solution implies that numerical and experimental methods are the remaining tools available to model this system. The implementation of an explicit scheme such as that used in CHEETAH requires some comparison to verify the results. With neither experimental nor analytical results for comparison, the validity of the results obtained for such a complex problem remains in question. To address questions concerning the accuracy of the numerical approach and results, a simpler problem is first considered.

4.1 Verifying Steady-State Temperature Distribution

In order to address this important question, a simplified version of the code called CHEETAH Cub was made to analyze a simpler system that only involves flow in one spatial dimension, but that like the original IHX system deals with both the steady-state and transient response of a two-fluid heat exchanger in a counter-flow arrangement. The steady-state solution to this one-dimensional three-phase problem is solved analytically and also numerically with CHEETAH Cub. The simplified system for the steady-state analysis is shown in Figure 4-1, below.

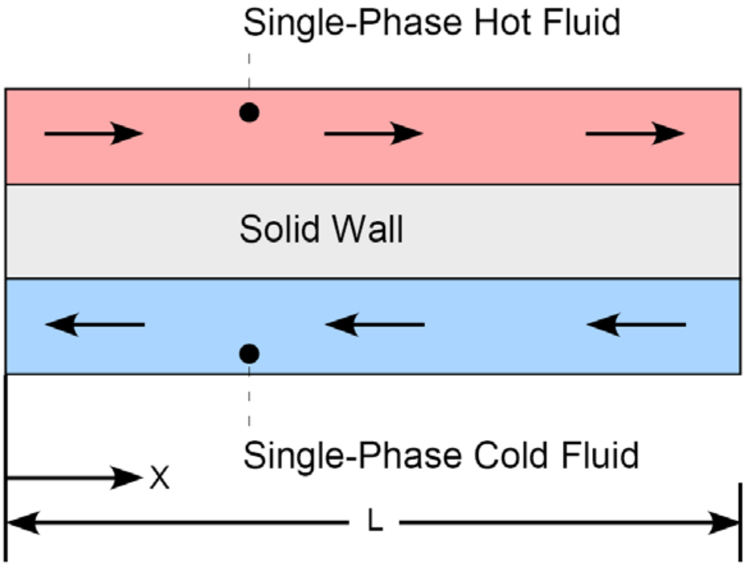

Figure 4-1: Schematic of the two single-phase fluid heat exchanger analyzed analytically and with CHEETAH Cub to obtain the steady-state temperature distribution.

The analytical and numerical results for this problem are presented so that the methods and algorithms used in the two-dimensional CHEETAH code can be verified for the steady-state case. The analytical solution to the steady-state temperature profiles in the three phases were analyzed using the effectiveness-NTU (number of transfer units) technique [17,18,19]. The complete analysis is available in Appendix C. The steady-state numerical solution found with CHEETAH Cub and the analytical results for the temperature distributions in all three phases in the heat exchanger are in agreement and are shown in Figure 4-2.

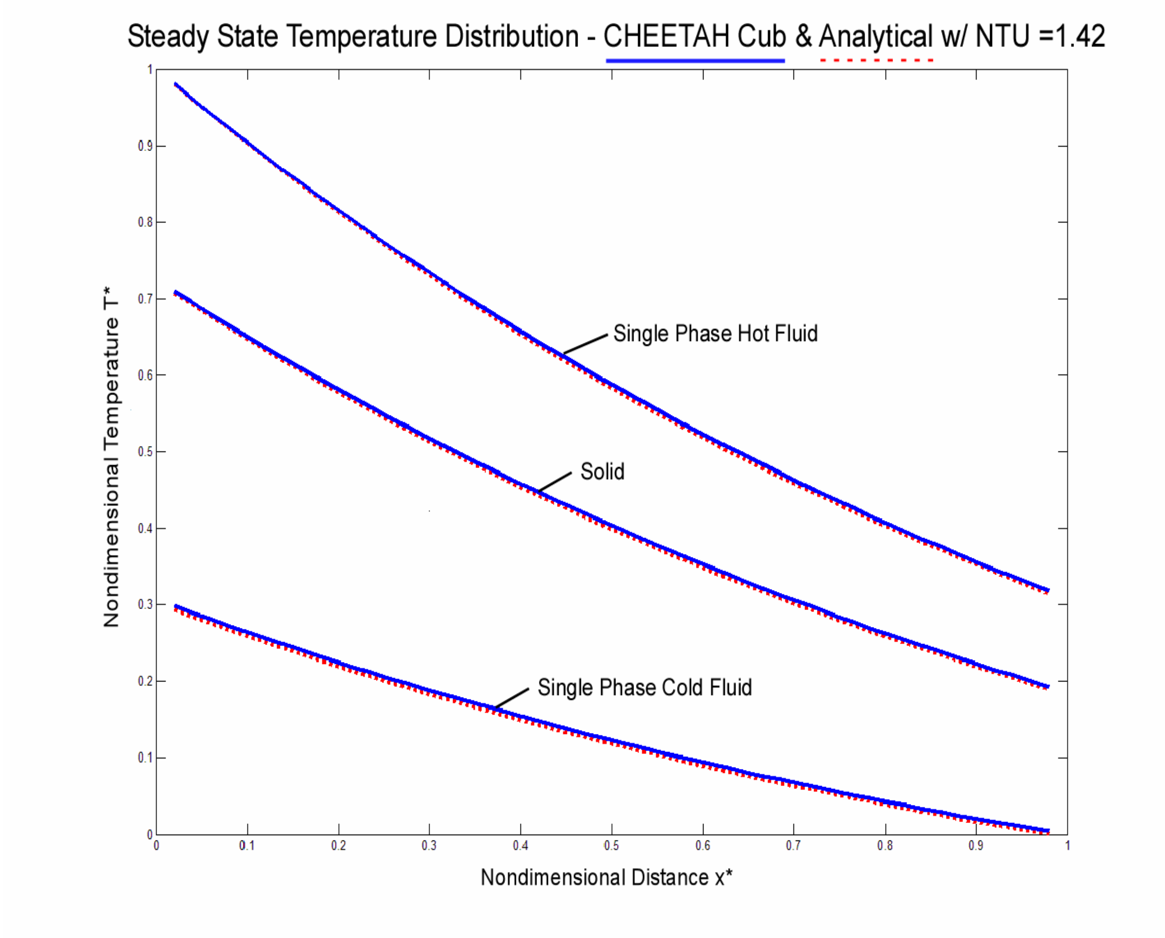

Figure 4-2: Steady-state temperature distribution by CHEETAH Cub and analytical solution.

The good agreement between the results reported from CHEETAH Cub and the analytical effectiveness-NTU method verifies that the algorithms, discretization, and methodology employed in the code correctly solve for steady-state conditions in a one-dimensional counter-flow heat exchanger.

4.2 Verifying Transient Temperature Distribution

Verifying the results for the transient response in this simplified arrangement is more complicated, but some analytical approaches are found in the literature and can be used for comparison with results from CHEETAH Cub. An integral method approach for the transient response is chosen for comparison; this approach is published in the International Journal of Heat and Mass Transfer authored by Juan Yin and Michael Jensen in 2003 [21].

In this publication, Yin and Jensen propose an analytical model for transient heat exchanger response for a flow arrangement very similar the one considered in the steady-state verification. This flow arrangement utilizes a single-phase fluid flowing in the positive *x* direction and a constant-temperature fluid flowing in the negative *x* direction as shown in the figure below. A solid wall separates the two fluids and has a prescribed convection coefficient on each side which governs heat transfer. Because one fluid undergoes no change temperature its flow direction is not relevant, and thus the analysis is equally applicable to a counter-flow, cross-flow, or parallel flow heat exchanger [21]. All temperatures are averaged or lumped in the vertical direction for each phase, as shown in Figure 4-3.

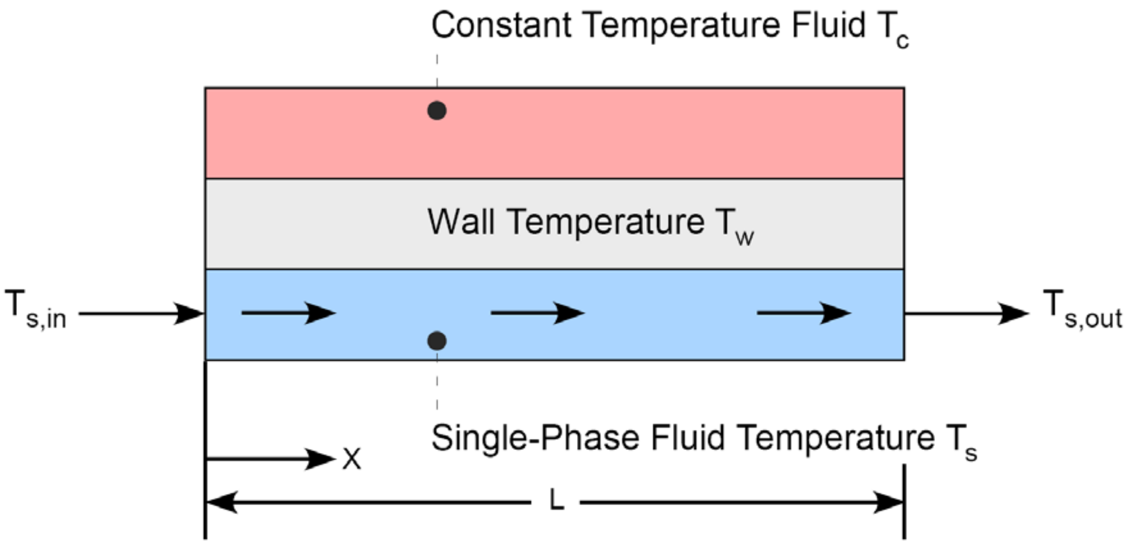

Figure 4-3: Schematic of heat exchanger used for verification with results from Yin and Jensen.

Yin and Jensen identify three important non-dimensional parameters that characterize the system in their article as shown below.

$$N_1 = \frac{m_w c_{pw}}{m_s c_{ps}}, \quad N_2 = \frac{h_c A_c}{\dot{m} c_{ps}}, \ and \ N_3 = \frac{h_s A_s}{\dot{m} c_{ps}} \qquad \text{Equation 4-1}$$

Here, N_1 shows the ratio of thermal energy that is stored in the wall and in the single phase for each degree of temperature rise with respect to time between them. N_2 represents the ratio of convection heat transfer in the constant temperature (or constant phase) fluid to advective heat transfer in the single-phase fluid. N_3 represents the ratio of convection heat transfer associated with the single-phase fluid and the advective heat transfer in the single-phase fluid. Finally, the NTU represents the ratio of the convective power between a fluid and the heat exchanger per degree of temperature difference to the advective power per degree of temperature change the fluid. For this problem, the NTU is expressed as follows:

$$NTU = \frac{h_c A_c h_s A_s}{\dot{m} c_{ps}(h_c A_c + h_s A_s)} = \frac{N_2 N_3}{N_2 + N_3} \qquad \text{Equation 4-2}$$

For comparison and verification the same simplified system is also characterized in CHEETAH Cub, where an energy balance is performed on the finite volumes just as in CHEETAH. The energy equation is written for each phase in the system occupying a control volume. The method and algorithms are identical to those used in the CHEETAH code for the two-dimensional system. The energy equations that represent the system are as follows:

Constant Temperature Fluid (c):

$$T_c = Constant \ \ (step\ changes\ in\ value\ at\ time\ equals\ 0) \qquad \text{Equation 4-3}$$

Wall or Solid (w):

$$h_c a_c'(T_c - T_w) - h_s a_s'(T_w - T_s) = \rho_w c_w \frac{dT_w}{dt} \qquad \text{Equation 4-4}$$

Single Phase Fluid (s):

$$u_s \rho_s c_s T_s\big|_x - u_s \rho_s c_s T_s\big|_{x+\Delta x} - h_s a_s'(T_s - T_w) = \rho_s c_s \frac{dT_s}{dt} \qquad \text{Equation 4-5}$$

In Yin and Jensen's analysis conduction effects will be neglected for both fluids and along the length of the wall, so the same is done in CHEETAH Cub and thus there are no axial conduction terms in the above energy equations.

Yin and Jensen then solve for the transient response of this system analytically using the integral method. They begin with a temperature distribution given by steady-state operation which is obtained from an analytical model based on the set of system parameters identified above. Two types of transients are induced:

Case 1: Step change in temperature of the uniform (constant) temperature fluid T_c (physically this can represent the change in the saturation temperature resulting from a step change in pressure).

Case 2: Step change in the flow rate of the single-phase fluid (physically this could result from a sudden partial blockage in system, pump failure or valve actuation).

Temperature profiles along the length of the one-dimensional heat exchanger are solved as a function of time. The integral method employed by Yin and Jensen involves using the steady-state solutions before and at the end of the transients together with two time functions to find the transient distributions for both the single-phase fluid and the wall temperature distributions in between these two states.

Yin and Jensen's method is analytical in nature; the derivation and final equations are quite involved and thus will it will not be covered in any greater detail here. Instead, this study focuses on comparing the results for CHEETAH Cub to those found by Yin and Jensen's model.

4.2.1 Case 1: Step Change in Temperature of Uniform-Temperature Fluid

In Case 1 as presented by Yin and Jensen, the constant-temperature fluid undergoes a step temperature rise and the transient behavior of both the single-phase fluid and the wall are calculated. Yin and Jensen used the object-oriented Modelica language to program a simulation in the Dymola (Dynamic Modeling Laboratory) software to verify their integral method analysis [21].

Figure 4-4 shows the results from the CHEETAH Cub code, Yin and Jensen's integral method analysis, and Yin and Jensen's computational Dymola model. The three analyses show excellent agreement throughout the transient for the single-phase fluid.

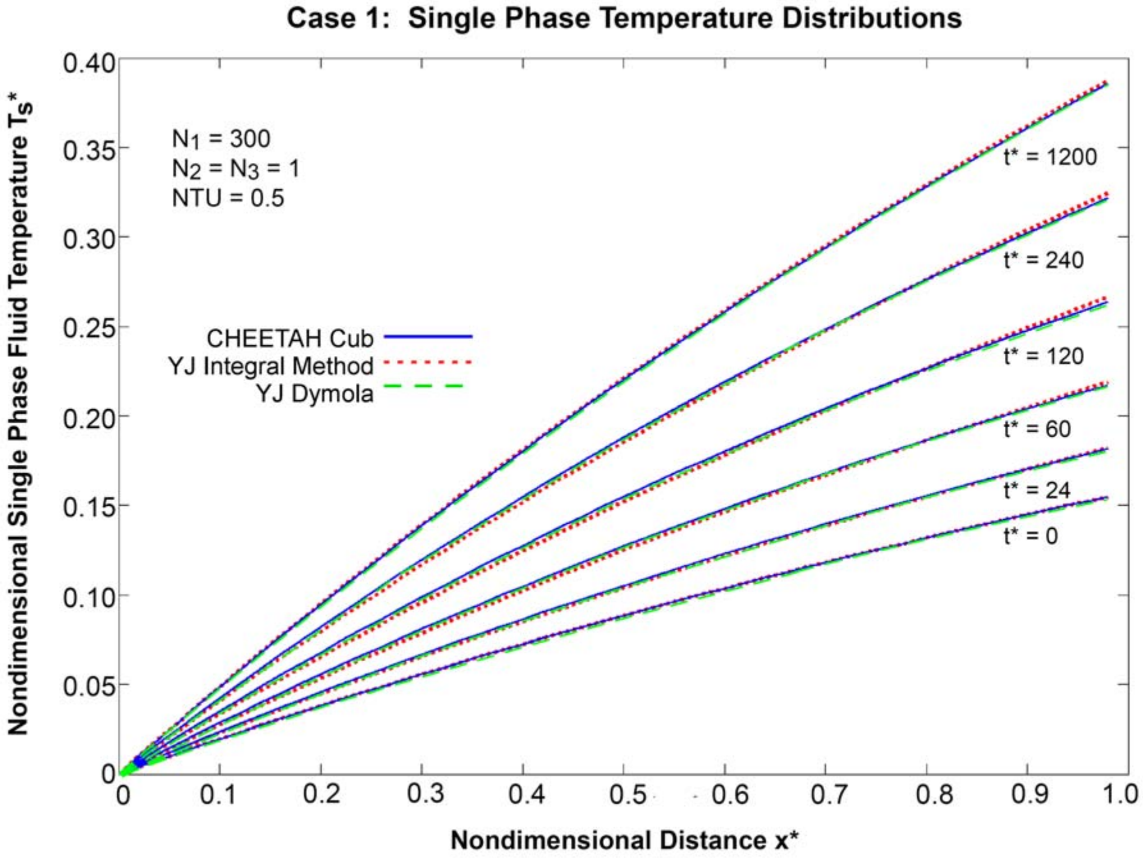

Figure 4-4: Case 1: Transient temperature distribution in the single-phase fluid solved by CHEETAH Cub and by both the computational Dymola model and integral method presented by Yin and Jensen [21].

The transient temperature distribution along the heat exchanger wall obtained with the CHEETAH Cub code also shows very good agreement with results from both Yin and Jensen's integral method analysis and with the computational results from their Dymola model. The computations results from the Dymola analysis are used to verify the integral method analysis and can also serve to further verify the numerical results from the CHEETAH Cub code.

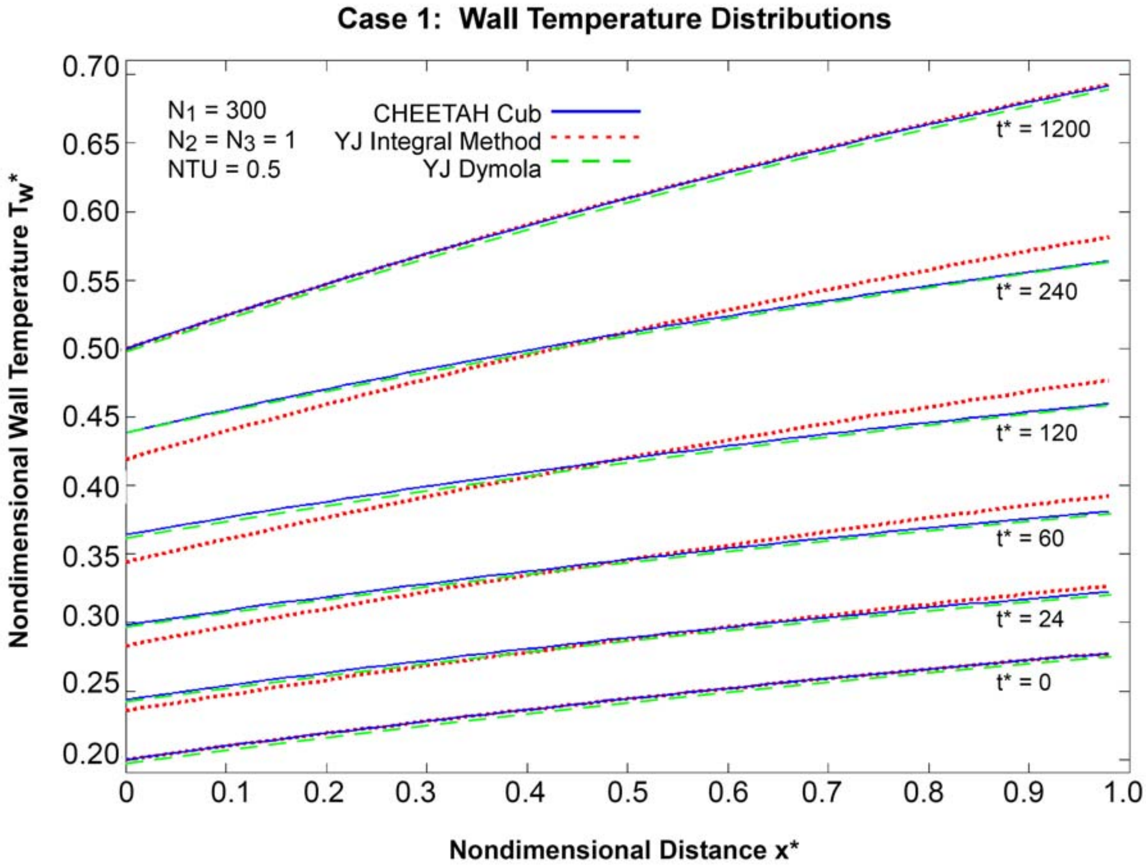

Figure 4-5: Case 1: Transient temperature distribution in the wall solved by CHEETAH Cub; closely matches the distributions found using Yin and Jensen's [21] integral method and the computational Dymola analysis.

The agreement in the lengthwise temperature distributions obtained both during the transient and near the final temperature distribution (t*=1200) demonstrates that the algorithms used in the CHEETAH Cub code provide reliable transient and steady-state results.

Grid independence was also tested by successive halving of the discretized volumes with no appreciable distortion observed. Care must be taken to ensure the scheme is stable. This can be achieved by maintaining a small Courant number $u^* \Delta t \,/\, \Delta x$

(Co_{MAX} <.25 was used in this case). Again, this verification effort (Case 1) is related to the transient step change in temperature of the uniform temperature fluid.

In this section, the algorithms in CHEETAH Cub are tested against the transient behavior that would result in the heat exchanger during a thermal transient induced by a step change in the temperature of the uniform temperature fluid. The study by Yin and Jensen contains an analytical model that is verified by numerical simulation. Both results presented the analyses by Yin and Jensen showed excellent agreement with the results obtained by the CHEETAH Cub code.

4.2.2 Case 2: Step Change in Flow Rate of Single-Phase Fluid

In Case 2, gamma (*γ)* represents the ratio of mass flow rate of the single-phase fluid after the step change to the mass flow rate of the single-phase fluid before the step change. The following figures show the fidelity of the CHEETAH Cub code under flow transients of varying magnitude. To match the results published by Yin and Jensen, rather than showing the spatial temperature distribution, the following figures show the variation in time of the outlet temperature under different flow transients denoted by varying values of gamma, $\gamma = \dot{m}_\infty / \dot{m}_o$. This allows a more complete comparison of the transient effects over various flow transients.

The results from the CHEETAH Cub code are compared with results from Yin and Jensen in Figure 4-6.

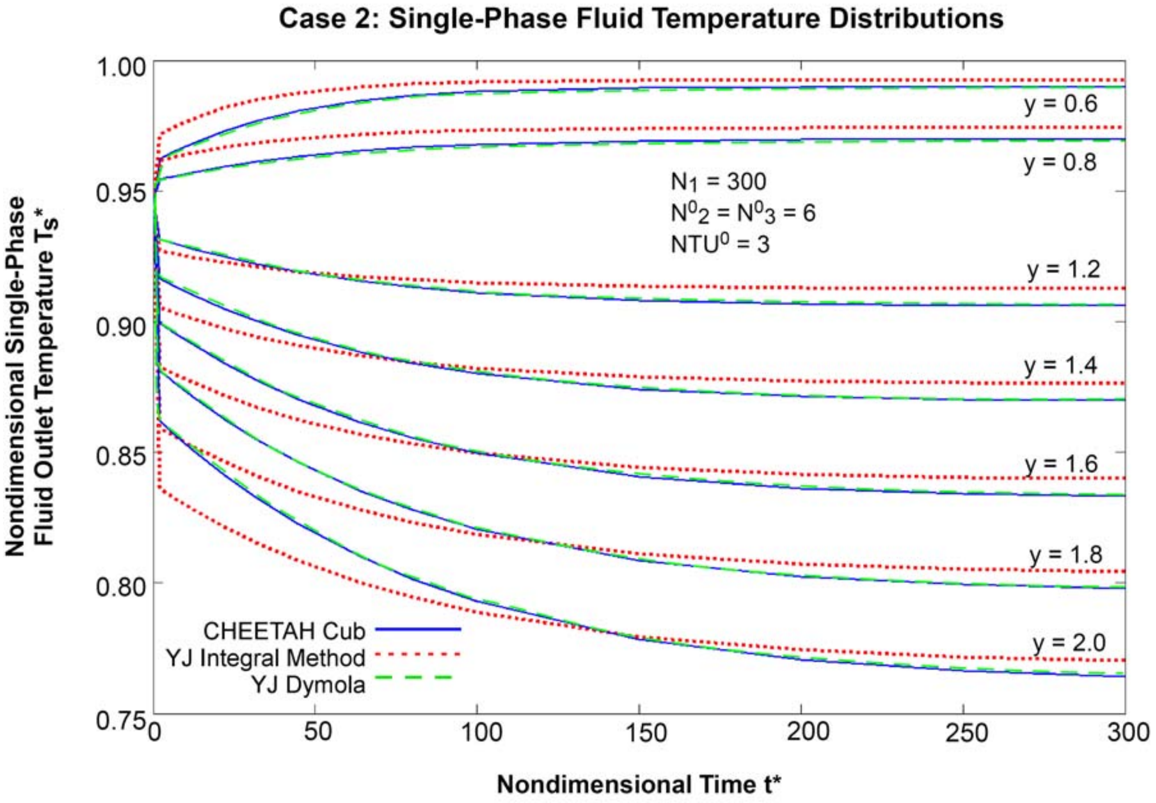

Figure 4-6: Case 2: Transient outlet temperature of the single-phase fluid solved by CHEETAH Cub and with Yin and Jensen's computational and integral method analyses [21]; small discrepancies are noted.

Excellent agreement is shown at all times between the results from the CHEETAH Cub code and those executed in Dymola by Yin and Jensen. Modest differences can be seen are shown between the computational results and those from Yin and Jensen's integral method. These differences are particularly noticeable near the step change in conditions, as can also be seen in Case 1. Similar behavior can be observed in the outlet wall temperature distributions shown in Figure 4-7 where again the two numerical models match well and deviate some from the results from the integral method published by Yin and Jensen.

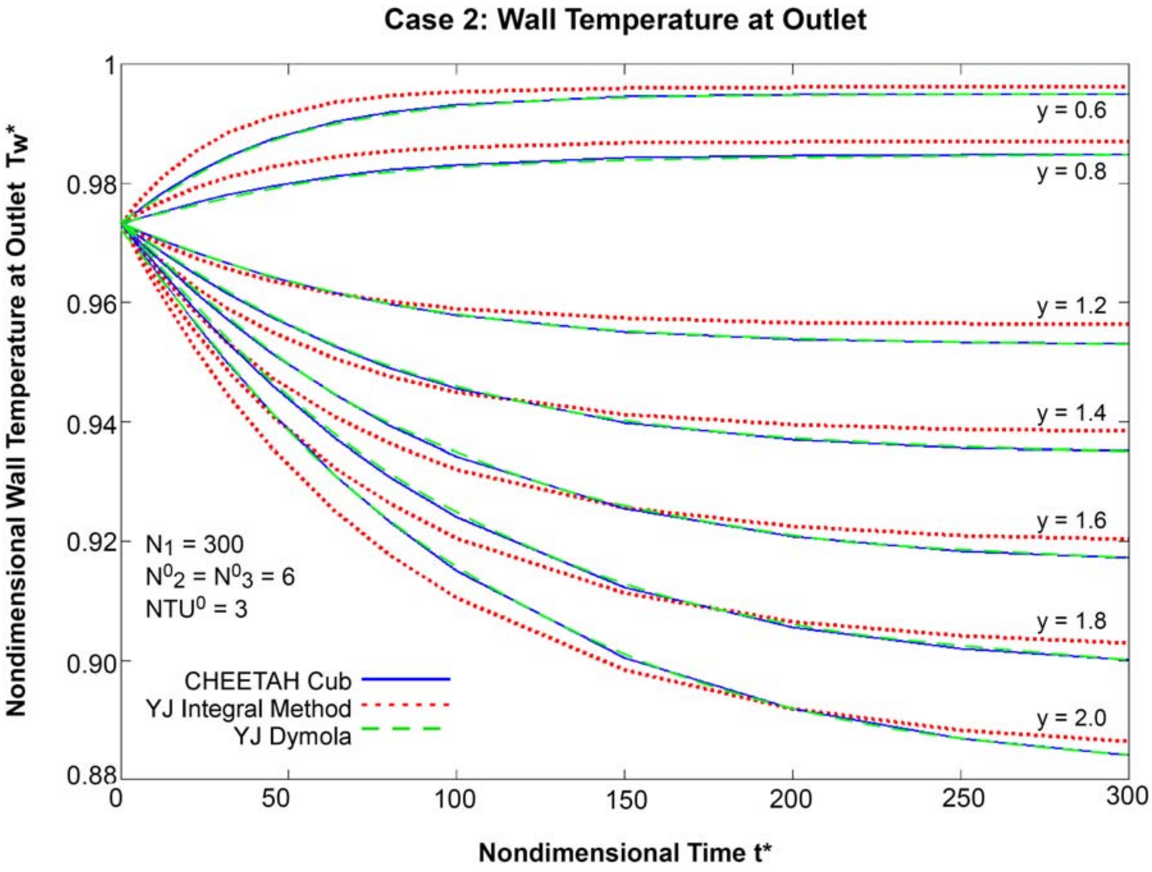

Figure 4-7: Case 2: Transient wall temperatures at the outlet solved by CHEETAH Cub and with Yin and Jensen's computational and integral method analyses [21]; small discrepancies are noted.

A relationship can be observed between the magnitude of the step change in mass flow rate and the discrepancy between the model proposed by Yin and Jensen and that found with CHEETAH Cub. In correspondence with the authors, they note that the use of the integral method in their model means that their time averaged solution is correct but that it will show greater error at times near the initiation of the transient. In Case 2, the discrepancy is indeed most notable at times near the initiation of the transient and is mostly limited to the single-phase temperature distribution (Figure 4-6) since it experiences a more volatile change in temperature from the high value of N_1 and due to the N_3 value being greater than unity. Comparing the single-phase fluid and wall temperature histories reported by CHEETAH Cub with those found in the numerical model simulated in Dymola by Yin and Jensen, it is clear that both numerical models produce matching results.

In the numerical analysis, Yin and Jensen checked grid independence in space and time by successive halving of the increments [21]. Furthermore, Yin and Jensen benchmarked their numerical results against those of Romie [22] and Roetzel and Xuan [23] for a parallel and counter-flow heat exchanger arrangement and reported that "the agreement was excellent [21]." The near match between the results of the CHEETAH Cub code and those from the Dymola analysis performed by Yin and Jensen verifies the approach used in CHEETAH Cub. The good agreement with Yin and Jensen's integral method further verifies both analyses. These results from this one-dimensional transient analysis give confidence in the techniques implemented in the two-dimensional CHEETAH code, since it relies on the same method and algorithms.

Chapter 5

Thermomechanical Stress Analysis

5.1 Domain Sub-Structuring with Effective Mechanical Properties

The creation of the composite plate is critical to both the mechanical analysis and the thermal hydraulic analysis. The thermal hydraulic results from Chapter 3 are buttressed by the verification of the code and method in Chapter 4. This is important because the thermomechanical stress analysis that follows will rely on temperature distributions provided by CHEETAH and presented earlier.

Just as discretizing the plate at the fin-scale required prohibitive computational power in the thermal hydraulic analysis, so too is it unfeasible to discretize at the fin scale in analyzing plate-scale temperature distributions on the composite plate. In the thermal hydraulic analysis it is valuable to use volume-averaged properties such as effective permeability, porosity, and effective convection coefficients. In a similar fashion, the evaluation of volume-averaged mechanical properties in zones within the composite plate will enable mechanical analysis on the plate scale with moderate computational time. Effective mechanical properties such as Poisson ratios, elastic, and shear moduli will be determined for several regions in the composite plate that share complex geometries such as the solid plate, flow distributor regions, and the offset strip fin region. The regions for which effective mechanical properties are evaluated as well as the regional representative unit cells are shown around the composite plate in Figure 5-1, below.

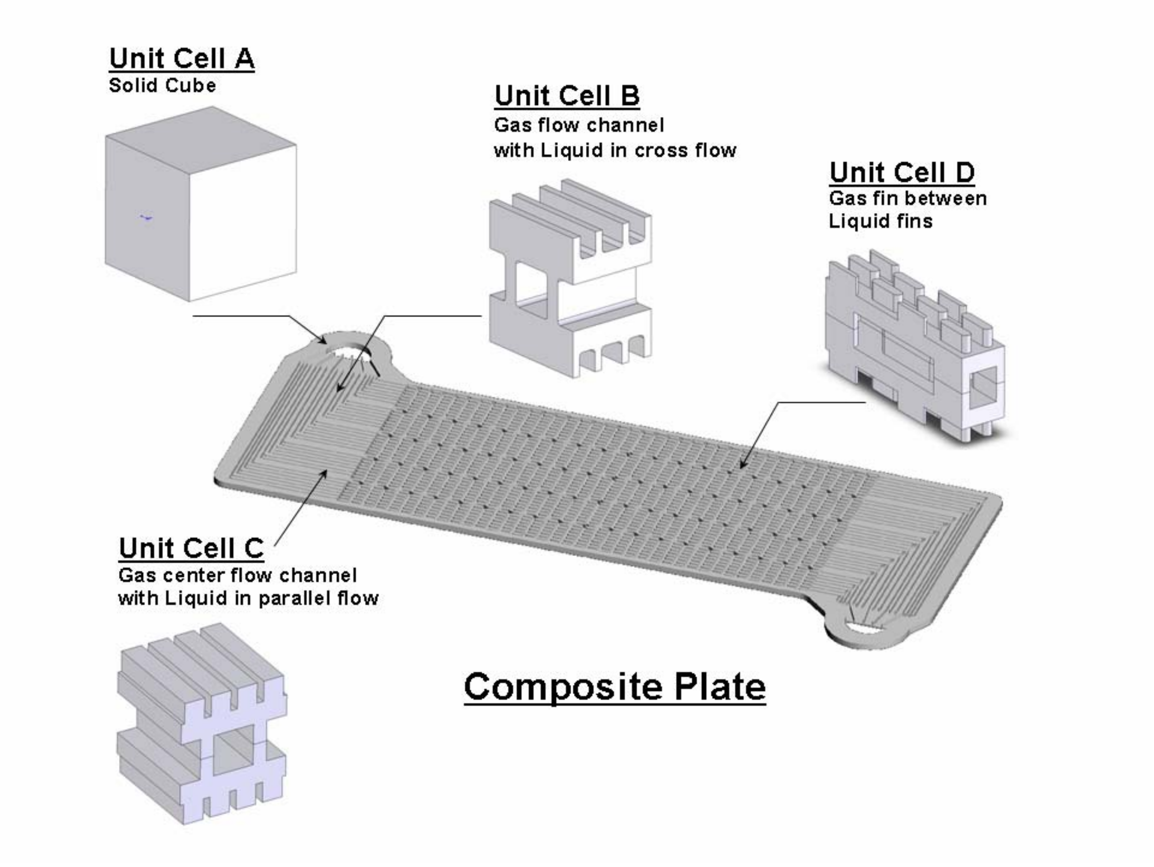

Figure 5-1: Composite plate with the representative unit cells that are used to calculate effective mechanical properties.

Finding the effective mechanical properties of a complex and repeating geometry involves subjecting a test section or unit cell to the same test procedures used to characterize a material. Essentially, the complex repeating geometry of the region is replaced by a simple geometry made of a representative material that has the same mechanical properties as the complex geometry in another material. This concept is illustrated in Figure 5-2, below, where Bar 1 and Bar 2 are both made of Alloy A while Bar 3 is made out of a more elastic Alloy B. Both Bar 1 and Bar 3 are solid while Bar 2 has a complex repeating geometry.

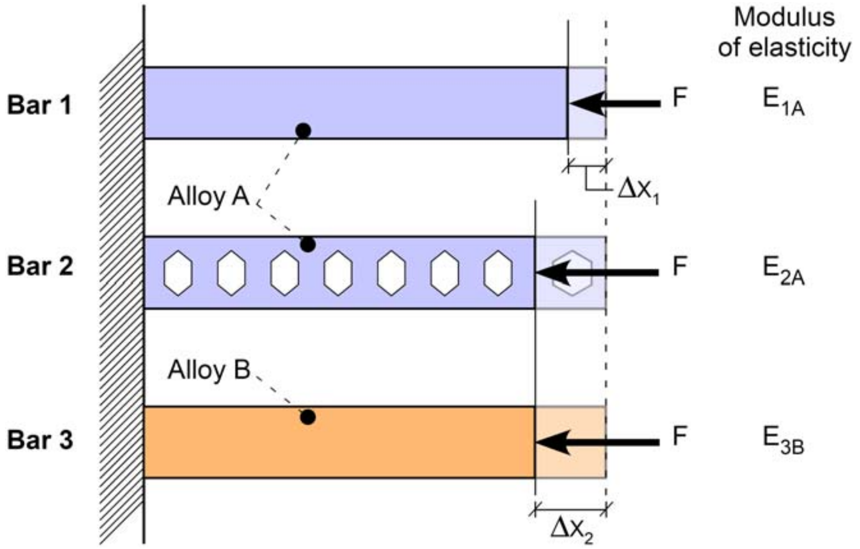

Figure 5-2: A mechanical component with a simple geometry can replace a component with a complex geometry when the two share effective mechanical properties such as an effective modulus of elasticity.

Under the same compressive load, both Bar 2 and Bar 3 deflect equally and both deflect more than Bar 1. Analyzing the deflection and applied load allows for the calculation of a modulus of elasticity (E) for each bar. Clearly, Bar 1 and Alloy A will have the highest modulus of elasticity (most rigid). The more complex geometry of Bar 2 with Alloy A gives it an effective elastic modulus (E_{2A}) that equals the elastic modulus (E_{3B}) for the less rigid Bar 3 and Alloy B. This means that in this type of model the more complex geometry of Bar 2 with Alloy A can be replaced by the simpler geometry of Bar 3 with Alloy B, saving computation time.

Explained more conceptually, the idea of effective properties and materials in a computational model is analogous to replacing the complex geometry of a short metal spring with the simple geometry of a short rubber cylinder or slug that has the same elasticity. Clearly the short rubber cylinder is simpler to model from a computational perspective due to its simple geometry.

Applying this idea to the composite plate shown in Figure 5-1, above, the unique geometry of each of the four representative unit cells in the composite plate will create four regions in the composite plate, each with their own effective mechanical properties, as if the regions were made of different materials. Unlike in the one-dimensional and isotropic example shown above, however, three out of the four unit cells have orthotropic material properties. The isotropic cell is unit cell A while the orthotropic unit cells are B, C, and D.

Explained simply, orthotropic materials have mechanical properties that are directionally-dependent in the three principle axes. Characterizing the effective material properties of each of the regions with orthotropic unit cells will require nine material constants per unit cell versus two material constants needed to fully characterize the isotropic unit cell. Detailed work on this technique can be found in a publication by D. Huang, H. Zhao, and P. F. Peterson [2] and in a descriptive write-up by Kenneth Lee [Appendix D], who found the effective mechanical properties in this study.

The nine constants needed to characterize an orthotropic material include three-directional moduli of elasticity (Young's moduli), *E*, three Poisson's ratios (relate strain in orthogonal directions), ν, and three shear moduli, *G*. These constants are related to one another through Hooke's Law for orthogonal materials. The 6x1 stress matrix shown below in Equation 5-1 is set equal to the product of the (9x9) inverse elastic matrix (equal to the stiffness matrix) and the (6x1) strain matrix [24].

$$\begin{Bmatrix} \sigma_{xx} \\ \sigma_{yy} \\ \sigma_{zz} \\ \sigma_{xy} \\ \sigma_{yz} \\ \sigma_{xz} \end{Bmatrix} = \begin{bmatrix} \frac{1}{E_x} & -\frac{\nu_{xy}}{E_x} & -\frac{\nu_{xz}}{E_x} & 0 & 0 & 0 \\ -\frac{\nu_{yx}}{E_y} & \frac{1}{E_y} & -\frac{\nu_{yz}}{E_y} & 0 & 0 & 0 \\ -\frac{\nu_{zx}}{E_z} & -\frac{\nu_{zy}}{E_z} & \frac{1}{E_z} & 0 & 0 & 0 \\ 0 & 0 & 0 & \frac{1}{2G_{xy}} & 0 & 0 \\ 0 & 0 & 0 & 0 & \frac{1}{2G_{yz}} & 0 \\ 0 & 0 & 0 & 0 & 0 & \frac{1}{2G_{xz}} \end{bmatrix}^{-1} \begin{Bmatrix} \varepsilon_{xx} \\ \varepsilon_{yy} \\ \varepsilon_{zz} \\ \varepsilon_{xy} \\ \varepsilon_{yz} \\ \varepsilon_{xz} \end{Bmatrix} \qquad \textit{Equation 5-1}$$

Furthermore, $\frac{\nu_{xy}}{E_x} = \frac{\nu_{yx}}{E_y}$, $\frac{\nu_{yz}}{E_y} = \frac{\nu_{zy}}{E_z}$, and $\frac{\nu_{xz}}{E_x} = \frac{\nu_{zx}}{E_z}$. This leaves nine unknown parameters for a given state of stress and strain. The three unknown shear moduli will be found through shear tests imposed on each unit cell using a commercial finite element analysis (FEA) code. Each cell will be subjected to a strain and the shear stresses will be evaluated using the FEA code. Hooke's law will thus yield a shear modulus for each of the three shear tests.

After executing these three shear tests and resolving the three shear moduli, there are still six unknown material constants left. These three unknowns are three Poisson ratios and three elastic moduli that can be seen in the inverse elastic matrix in Equation 5-2, below.

$$\begin{Bmatrix} \sigma_{xx} \\ \sigma_{yy} \\ \sigma_{zz} \end{Bmatrix} = \begin{pmatrix} \frac{1}{E_x} & -\frac{\nu_{xy}}{E_x} & -\frac{\nu_{xz}}{E_x} \\ -\frac{\nu_{yx}}{E_y} & \frac{1}{E_y} & -\frac{\nu_{yz}}{E_y} \\ -\frac{\nu_{zx}}{E_z} & -\frac{\nu_{zy}}{E_z} & \frac{1}{E_z} \end{pmatrix}^{-1} \begin{Bmatrix} \varepsilon_{xx} \\ \varepsilon_{yy} \\ \varepsilon_{zz} \end{Bmatrix} \qquad \textit{Equation 5-2}$$

In theory, executing two strain tests with displacements in the *x*, *y,* and *z* directions will provide six equations from which all six unknowns can be resolved. In practice, however, the two-test method yields an inverse elastic tensor with a condition number that is too high to give consistent results with Matlab. This is explained in greater detail in Appendix D. Therefore, three tests are necessary to solve for the remaining six unknowns and the technique previously used by D. Huang, H. Zhao, and P. F. Peterson [2] is used instead.

A test using this three-test technique involves straining a unit cell in the *x*, *y*, and *z* directions (ε_{xx}, ε_{yy}, and ε_{zz}) and using the FEA code to find the principle stresses (σ_{xx}, σ_{yy}, and σ_{zz}). Executing this test with sets of three directional strains will provide three matrix equations in total, which can be easily solved with matrix inversion giving all of the terms in the inverse elastic matrix (or stiffness matrix). Simple algebra then yields all of the directional moduli of elasticity and Poisson's ratios which are listed in Table 5-1, below.

Effective conductivity is also found with the FEA code by applying constant temperature constraints on either side of each unit cell and solving for the heat flux through each unit cell in that direction. The heat flux is then divided by the total area of the face in each direction and an effective conductivity is found. Effective conductivities for each unit cell are also listed in Table 5-1, below.

	UNIT CELL A	**UNIT CELL B**	**UNIT CELL C**	**UNIT CELL D**
E_x [GPa]	149.00	65.38	57.08	52.58
E_y [GPa]	149.00	69.09	99.30	59.95
E_z [GPa]	149.00	48.40	52.28	31.21
v_{xy}	0.30	0.24	0.17	0.26
v_{xz}	0.30	0.21	0.13	0.12
v_{yx}	0.30	0.25	0.30	0.30
v_{yz}	0.30	0.21	0.30	0.19
v_{zx}	0.30	0.16	0.12	0.07
v_{zy}	0.30	0.15	0.16	0.10
G_{xy}	58.83	50.65	29.81	21.20
G_{xz}	58.83	42.20	16.85	12.65
G_{yz}	58.83	38.39	31.99	15.52
k_x [W/mK]	25.50	11.23	11.25	9.67
k_y [W/mK]	25.50	11.87	16.99	11.33
k_z [W/mK]	25.50	8.85	11.69	9.16
Solid phase fraction	1	0.53	0.67	0.53
Liquid phase fraction	0	0.22	0.08	0.23
Gas phase fraction	0	0.25	0.25	0.23
Liquid s.area density [m^2/m^3]	0	125.09	97.60	112.40
Gas s.area density [m^2/m^3]	0	32.89	44.30	77.60

Table 5-1: Effective conductivities for unit cells A, B, C, and D.

With the effective mechanical properties for each unit cell specified, the FEA model can be reconstructed as a true composite plate made of several materials, each with its own mechanical properties. When these regions are put under mechanical strain they will respond just as the more complex geometry of the unit cells would under similar deflection because analysis from their stress tests provide the effective moduli and Poisson's ratios.

After recreating the two-dimensional composite plate analyzed in CHEETAH in the FEA code ANSYS, the effective mechanical properties are added to the code's material library and assigned to their respective zones as shown in Figure 5-3, below. The solid plate, offset strip fin, flow, and cross-flow distributor areas are clearly assigned different effective material properties as dictated by color.

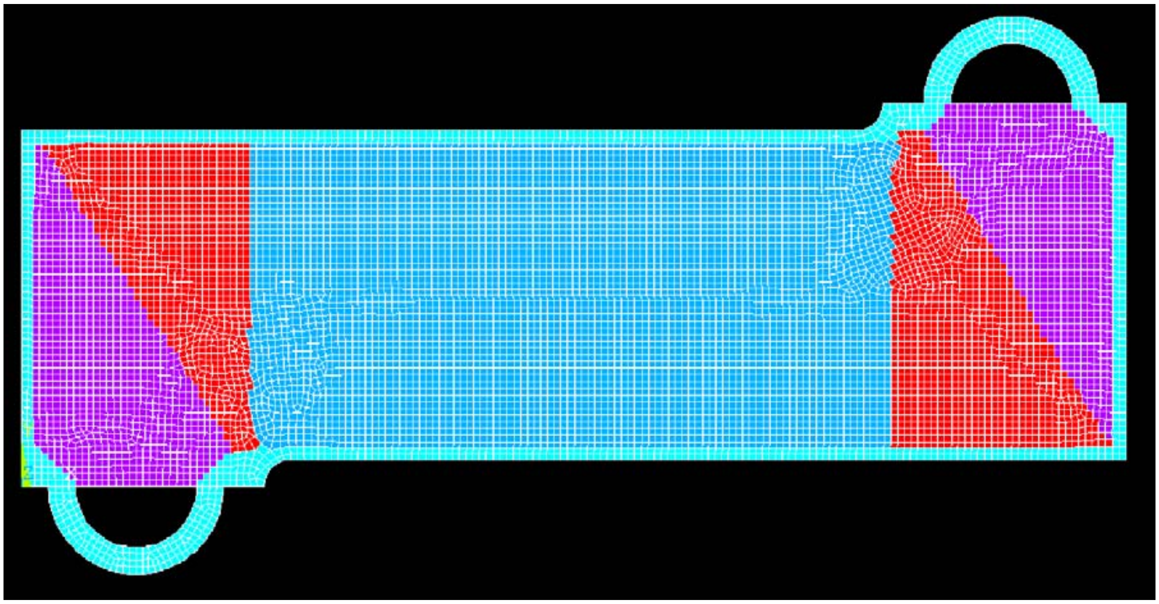

Figure 5-3: Two-dimensional ANSYS model of composite plate with effective material properties assigned.

5.2 CHEETAH-ANSYS Communicator Code (CAC code)

With the composite plate's temperature distribution in CHEETAH's Matlab data files and the composite plate's effective mechanical properties modeled and assigned in ANSYS, a code, tool, or utility had to be created to communicate results between these two codes. One of the attractive features of ANSYS versus other FEA codes is its simple text-driven commands. ANSYS can easily read simple text files with commands in them that allow the user to control every node and element in a finite element analysis. This option is not available with other FEA codes that are more intensely driven from their graphical user interface (GUI) such as Pro-E/Mechanica, Abacus, and COMSOL. The ability to read text files with assignments to every node gives the researcher complete control over the mechanical analysis. In this case it permits several thousand temperature results from CHEETAH to be entered into over ten thousand nodes in the FEA model in ANSYS. With matrices involving tens of thousands of values, this work must be automated.

Automating the data processing from CHEETAH to ANSYS first requires exporting a node text file from ANSYS containing the node number, and x, y, z coordinates of each structural node in the composite plate model (just over 10,000 nodes). This requires going to ANSYS' Preprocessor>Modeling>Create>Nodes>Write Node File commands and naming the file. This file is then read into the CHEETAH-ANSYS Communicator code (CAC code) written in Matlab. The data file from CHEETAH is also loaded into the CAC code where algorithms calculate the position of each ANSYS node on the CHEETAH discretization or grid. With the ANSYS node's location, the distance to the nearest four surrounding CHEETAH nodes is calculated. Depending on distance to each of these surrounding nodes, a temperature is interpolated in two dimensions onto the ANSYS node. The CAC code then generates a command line in a text file which will assign this temperature to the ANSYS node by number. A typical command line to assign node #9096 (body force, BF) a temperature of 1197.87 K would read as follows: BF, 9096, TEMP, 1197.87.

After roughly 10,000 nodes and interpolations that include corner nodes and special nodes the text file is saved. This temperature assignment text file has over 10,000 command lines and is around 100kb in size. Assigning this array of values into the ANSYS model requires going to the Preprocessor and then File>Read input from … and selecting the .txt file created with the CAC code. After completing this procedure, all nodes in the FEA model are assigned a temperature solved in CHEETAH.

5.3 Steady-State Stress Analysis

The steady-state mechanical stress analysis that follows uses the temperature distribution found with constant thermophysical fluid properties in CHEETAH. A comparison of the temperature and mechanical stress distributions found using constant and temperature-dependent fluid thermophysical properties is covered in a later section. After assigning the steady-state temperature distributions to the ANSYS model, the software illustrates the temperature assignment with a color map. The color map of the composite plate in ANSYS can be seen in Figure 5-3.

The nodes on the outer edge of the welded pipe manifolds posed special challenges since there were often no neighboring nodes outside of these pipe sections. Special algorithms in the CAC code interpolate only between nodes with real temperature values. The temperature distribution in ANSYS along with the assignment of effective mechanical properties finally enables the thermomechanical analysis. The Von Mises stress distribution resulting from the complex thermal expansion of the composite plate can be seen in Figure 5-5. The constraint on the IHX composite plate can be seen on the pipe section. The constrained node belongs to the welded pipe section on the liquid outlet manifold.

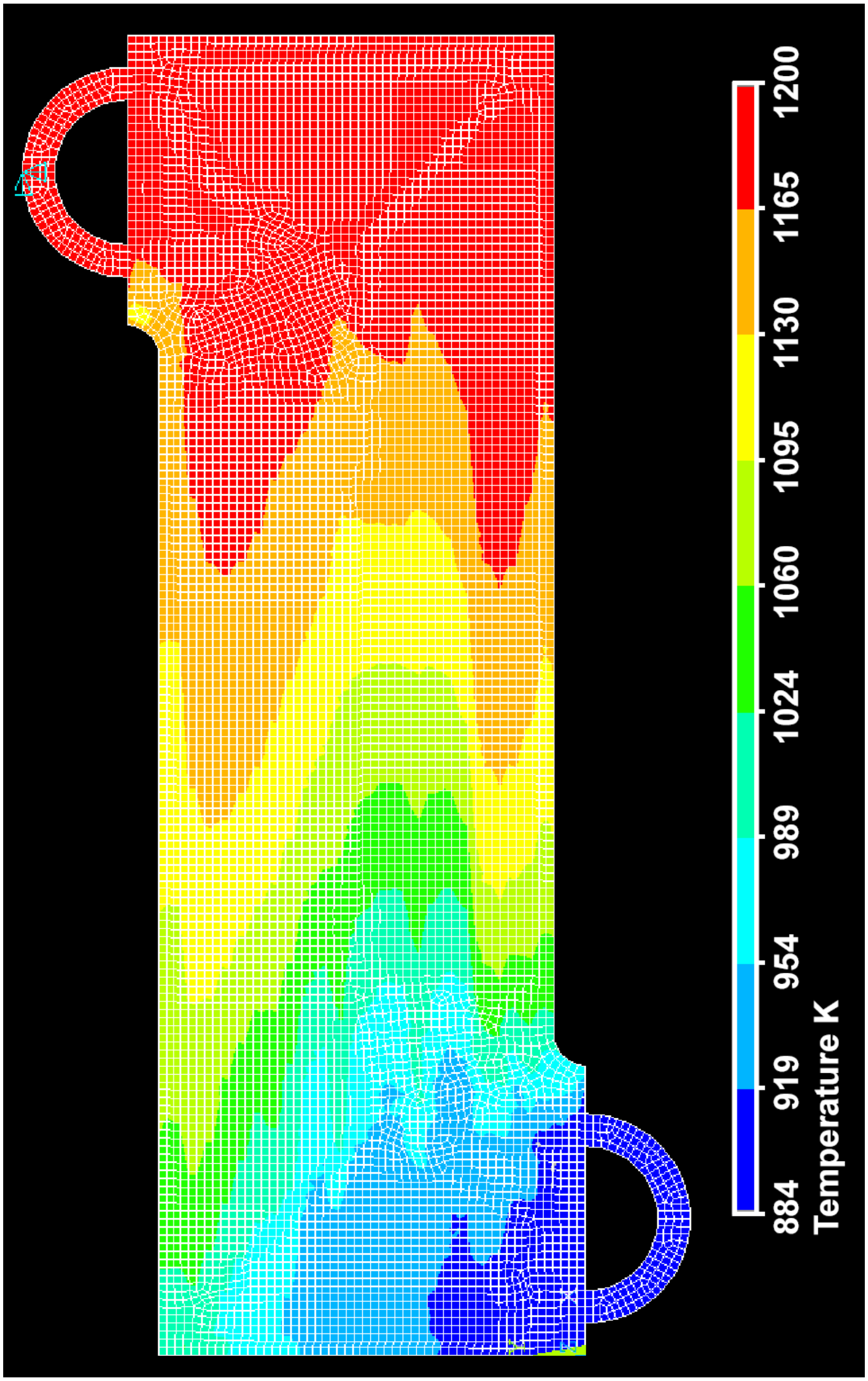

Figure 5-4: Steady-state temperature distribution in composite plate found using constant thermophysical properties in CHEETAH.

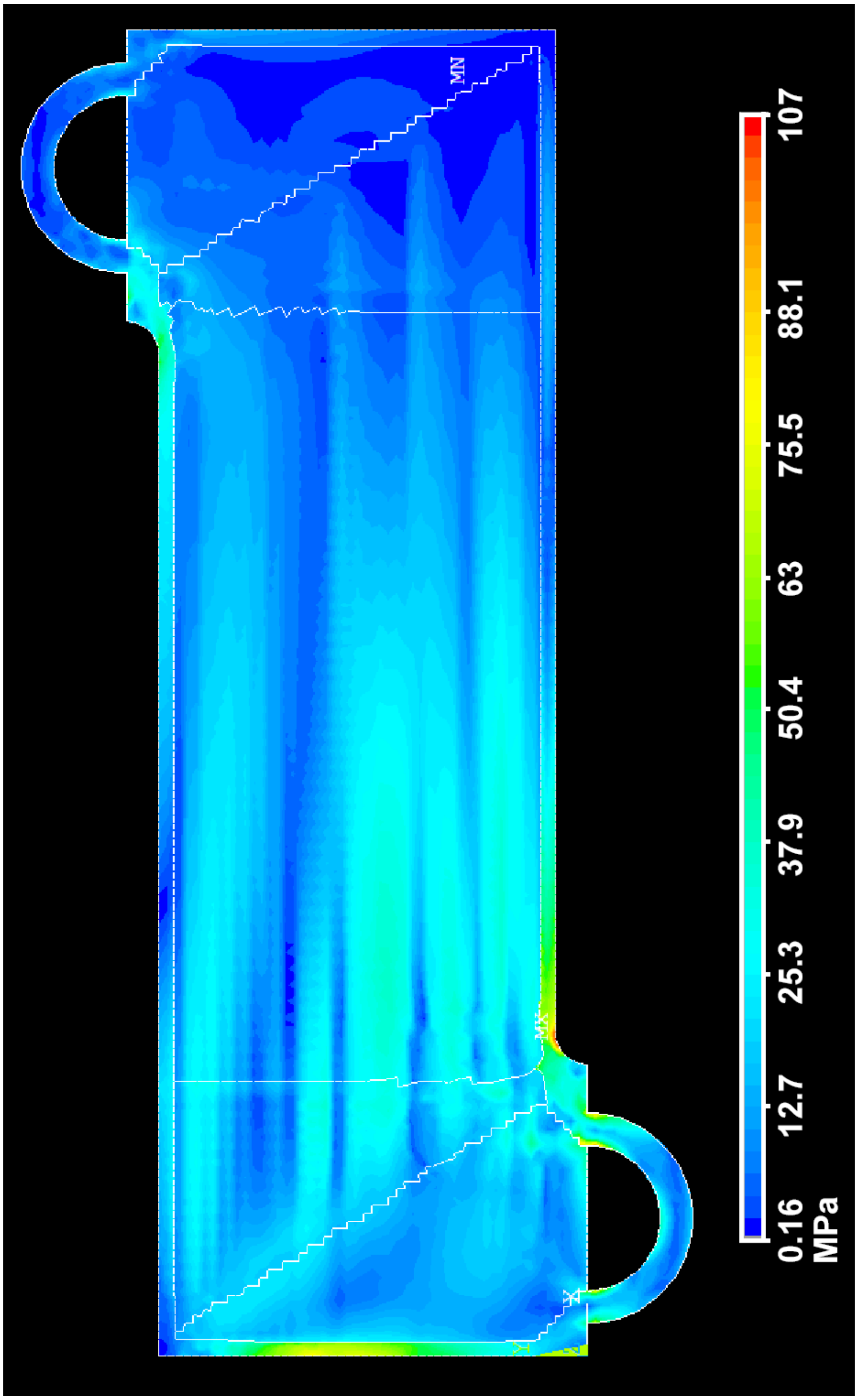

Figure 5-5: Von Mises stress distribution in composite plate with steady-state temperature distribution applied with a single node constraint on outlet pipe.

5.3.1 Failure Analysis - Yielding

The primary failure modes explored in this work are yielding and creep. At the plate scale the Von Mises stress distribution provided in Figure 5-5 is used to judge failure based on yielding, the onset of plastic deformation. The mechanical properties of Alloy 617 (Inconel) are published by HAYNES International [25]. The yield stress is a strong inverse function of temperature at high temperatures. Haynes reports that at 1143 K (870°C) the yield stress of Alloy 617 is 207 MPa, while at 1253 K (980°C) the yield stress is 111 MPa. The peak operating temperatures in the IHX are 1200 K (927°C), and performing a linear interpolation gives a yield stress at this temperature of 157 MPa. Assuming a typical factor of safety of two means that stresses in the composite plate should not exceed 78 MPa.

It is important to emphasize that the true yield stress of the composite plate is temperature dependent and because there is a spatial temperature distribution on the plate the yield stress is therefore spatially dependent. This is due to the large temperature difference from one end of the plate to the other, and also because the yield stress vary greatly with temperature.

For the steady-state temperature distribution, the peak stresses on the plate scale are around 100 MPa. This is below the yield stress but above the design limit set at 78 MPa. However, peak stresses do occur far from peak temperatures which are located near the gas inlet as can be seen in Figure 5-4. From the perspective of mechanical yielding, it seems the composite plate can withstand the operational stresses if imposed momentarily, but the current design for the composite plate fails to provide an adequate factor of safety. The following creep analysis will further explore the effects of this stress distribution on the composite plate over an extended period of time.

5.3.2 Failure Analysis - Creep

The Von Mises stress distribution provides the basis for the creep failure analysis performed on this design of the composite plate in the IHX. By operating at peak temperatures of 1200 K (927°C), the IHX must be robust enough to endure the stresses imposed at the operating procedure over a 30 year life. Several high-temperature alloys have creep data available for 100,000 hours, but for Alloy 617 only results for 10,000 hours were found. The maximum allowable creep stress listed by HAYNES International [25] at 1143 K (870°C) is 47 MPa, while at 1253 K (980°C) the maximum allowable creep stress drops to 17.45 MPa. The peak operating temperatures in the IHX are 1200 K (927°C), and performing a linear interpolation gives a maximum allowable sustained creep stress of 32.34 MPa. Including a factor of safety of two, the design limit for creep stress is 16 MPa for this application of Inconel Alloy 617.

In Figure 5-5, above, the peak stresses in the composite plate certainly exceed the design creep limit of 16 MPa. Operating Von Mises stresses in this two-dimensional analysis shows that the areas of the IHX exposed to peak temperatures experience operating stresses around 25 MPa which already surpasses the design limit for creep stress. Furthermore, it is important to note that this analysis includes only plate-scale expansion stresses and therefore excludes the pressure differential between the liquid and gas phases. This pressure differential is 7MPa, so with the plate-scale stresses included the total stress could come close to the maximum allowable creep stress with no safety factor. Plate-scale creep stresses in this design are unacceptable for the application; the composite plate must be redesigned to reduce operational stresses. This indicates that fin-scale stresses, which tend to be higher, will likely fail the creep criteria as well.

5.4 Effect of Constant and Temperature-Dependent Thermophysical Fluid Properties

Two complete steady-state thermal, hydraulic, and mechanical stress analyses were executed using the CHEETAH code and the FEA code ANSYS. The objective is to understand the significance of including effects caused by temperature-dependent thermophysical fluid properties in the analysis. Therefore both analyses used the same boundary conditions and composite plate parameters and were only different in that one used constant thermophysical fluid properties while the other included the temperature dependency. The resulting steady-state temperature distributions from both analyses are shown in Figure 5-6; the corresponding Von Mises stress distributions for both analyses are shown in Figure 5-7 and Figure 5-8.

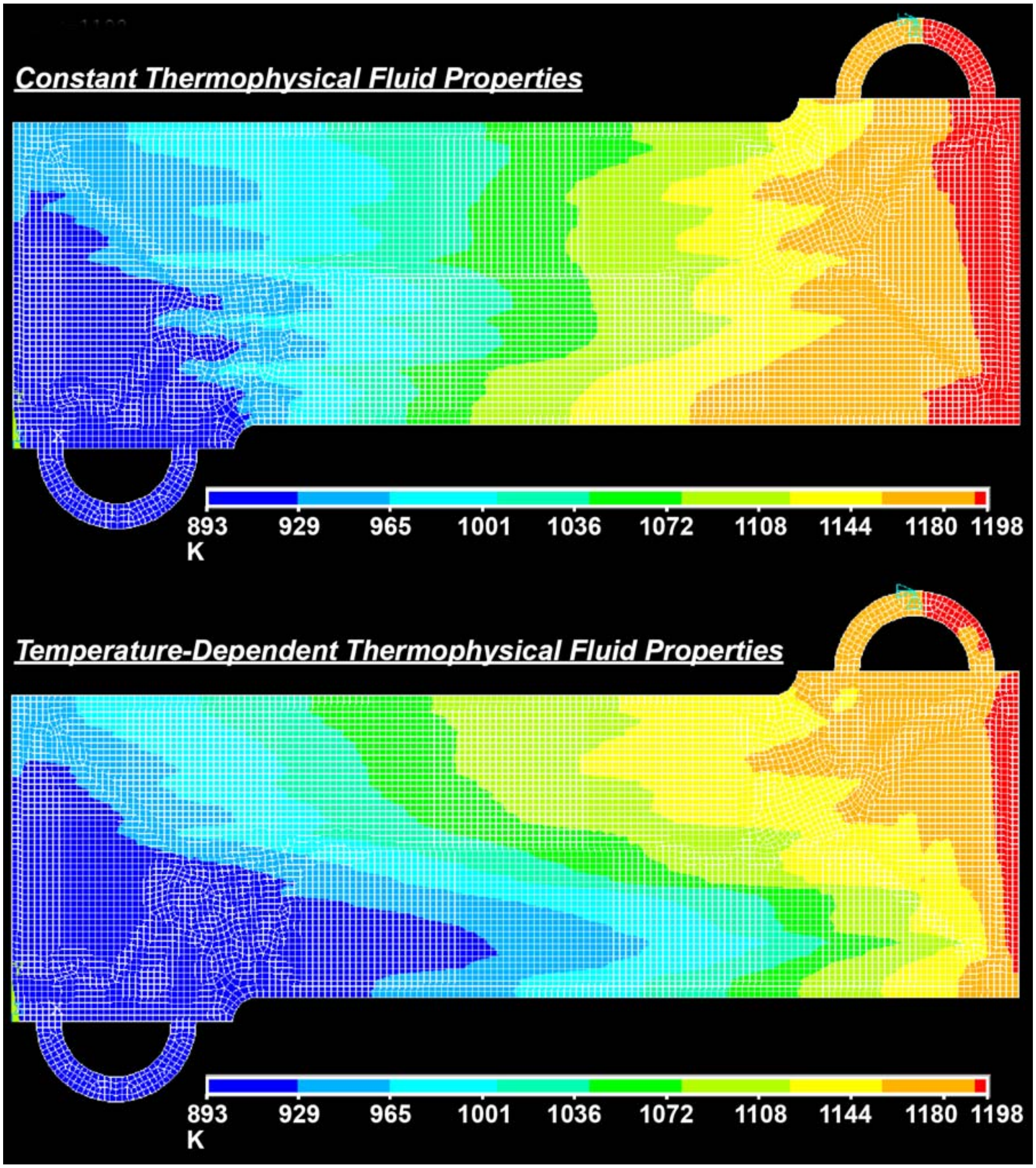

Constant Thermophysical Fluid Properties

Temperature-Dependent Thermophysical Fluid Properties

Figure 5-6: The steady-state temperature distribution is significantly affected by the inclusion of temperature-dependent thermophysical fluid properties.

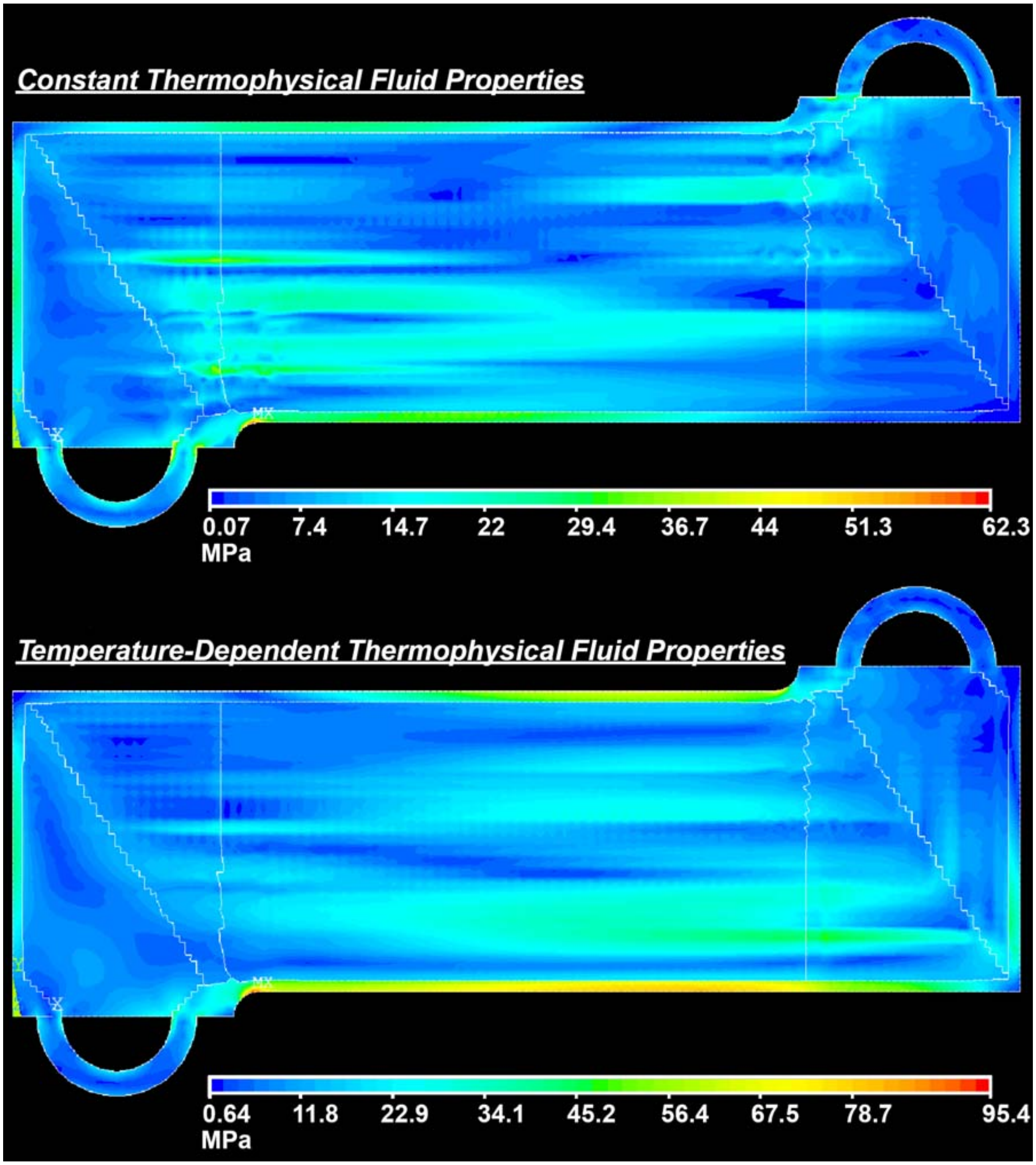

Figure 5-7: The Von Mises stress distribution with constant and temperature-dependent thermophysical fluid properties.

The thermal results show that the temperature-dependent fluid thermophysical properties significantly affect the temperature distribution in the composite plate. The larger cold zone near the liquid salt (cold fluid) inlet shows that the exposure to the longer distributor in the hot outlet manifold reduces the average viscosity of that flow path and increases flow and thus cooling over that flow path.

The resulting mechanical stress field shown in Figure 5-7 shows that while peak stresses increase by 50% in the temperature-dependent case, the steady-state stresses are still sufficiently low so as to not cause yielding. The peak stresses in the temperature-dependent fluid property case, however, are above the maximum allowable stresses when considering the safety factor. The stress field is significantly above what could be tolerated from a mechanical creep perspective in both cases. It is interesting to note that the stress field over the plate does change significantly when considering the temperature-dependent thermophysical fluid properties.

5.5 Transient Stress Analysis

The CHEETAH code, the CHEETAH-ANSYS Communicator code (CAC Code), and the FEA code (ANSYS) have enabled the mechanical analysis of composite plate design. The results have shown that the composite plate fails the design stress limits set for both yield and creep stresses. Still, this is an illustrative example that aims to show how the methodology and CHEETAH code can be applied towards compact heat exchanger optimization by executing comprehensive thermal, hydraulic, and mechanical analysis.

Despite showing that a redesign of the composite plate is required based on previously analyzed criteria, the analyses based on severe thermal hydraulic transients are presented to illustrate the methodology and utility of the CHEETAH code.

The two transients solved by CHEETAH in Chapter 3 involve harsh step changes in the flow of just one of the two fluids in the IHX. The following analysis will build on those thermal hydraulic results to perform transient thermomechanical analysis on the composite plate. The temperature distributions come from analysis using the CHEETAH code with constant thermophysical properties. Including the steady-state temperature distribution, a total of six temperature distributions are used in each transient analysis.

The first thermomechanical transient examined results from the interruption of the cold liquid salt flow in the heat exchanger. Consequently a heating front propagates through the IHX as the hot helium continues flowing. The results for the first thermomechanical transient can be seen in Figure 5-8 in 15 second intervals. The second thermomechanical transient examined results from the interruption of the hot helium flow in the heat exchanger. A cooling front then moves through the IHX as the cold liquid salt continues flowing. The results for the second thermomechanical transient can be seen in Figure 5-9. For both cases, the temperature distributions can be seen on the left-side and the corresponding Von Mises stresses are illustrated on the right-side of Figure 5-8 and Figure 5-9, below. One legend applies to all of the stress distributions and another to all the temperature distributions.

5.5.1 Liquid Salt (Cold) Pump Trip

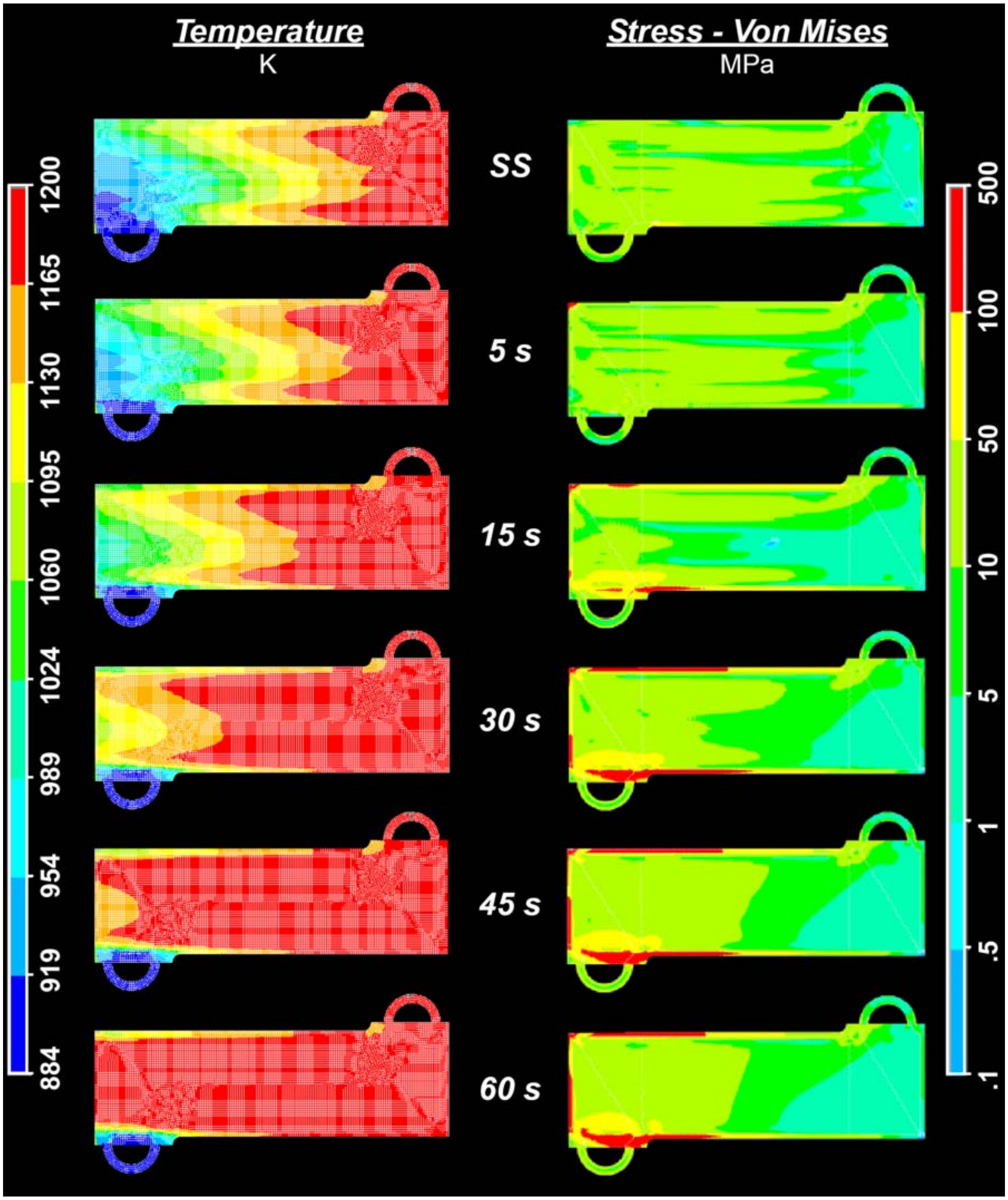

Figure 5-8: Temperature and Von Mises stress distributions corresponding to the liquid salt pump trip results in heating front propagation.

5.5.2 Helium (Hot) Pump Trip

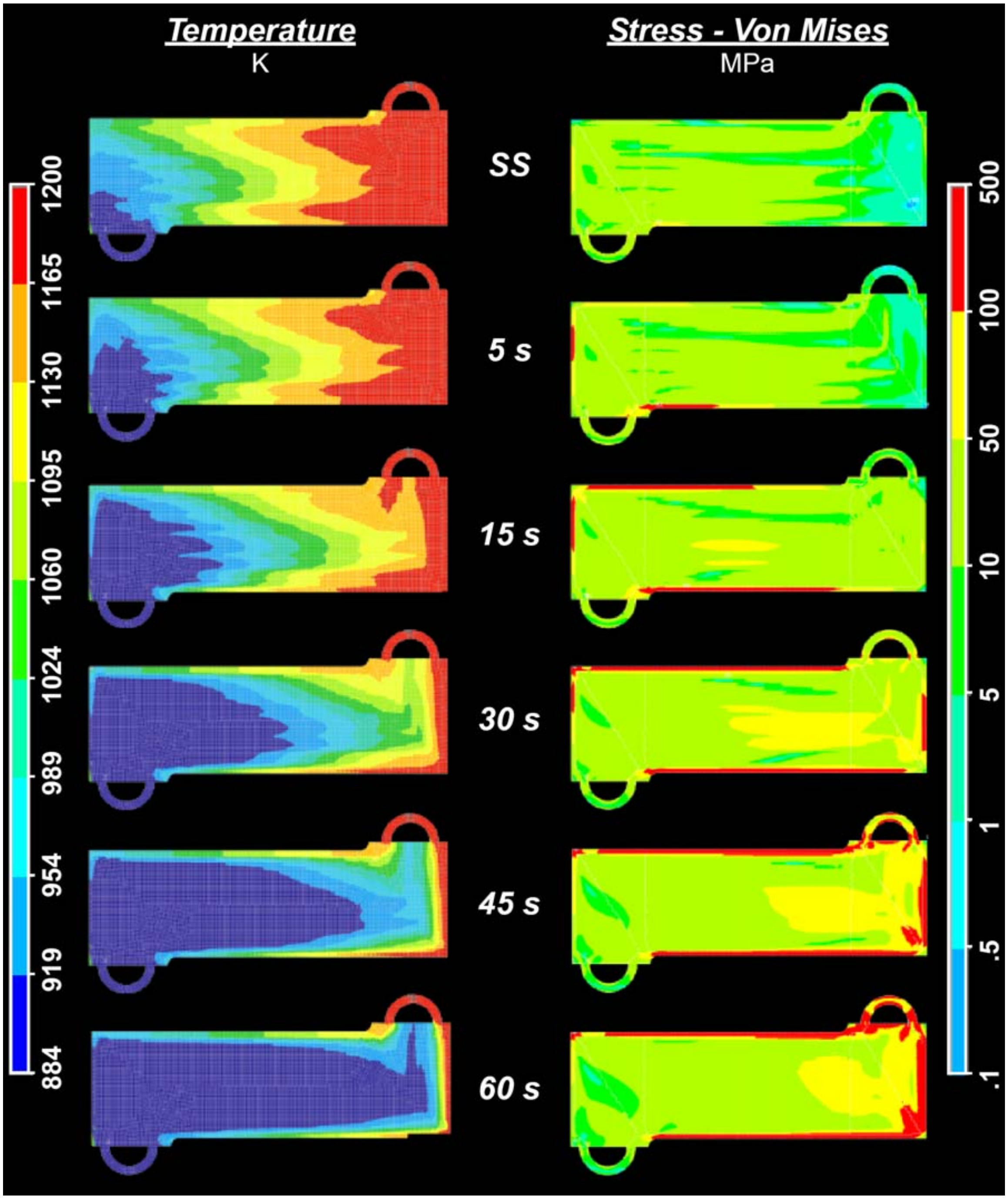

Figure 5-9: Temperature and Von Mises stress distributions corresponding to the helium pump trip results in cooling front propagation.

Based on the peak temperature of 1200 K (927°C), the yield stress for Inconel Alloy 617 is 157 MPa and considering a typical safety factor of two, Von Mises stresses should be kept below the design stress limit of 78 MPa. The results of both thermomechanical transients shown in Figure 5-8 and Figure 5-9, above, show that the temperature gradient propagating through the composite plate creates moderate plate-level stresses in the majority of the composite plate.

In both cases, peak stresses move in the direction of the propagating temperature gradient and concentrate on the perimeter of the composite plate where the cross-section of the material is thicker and takes significantly longer to equilibrate. Also, in both cases, the temperature gradient can be seen to remain near the inlet of the residual flow rate at the end of the transient. As expected, this residual flow rate plays an important role in peak stresses by creating a steep temperature gradient in its entrance area. This phenomena can be observed in the temperature gradient and associated stresses that can be seen in Figure 5-8 near the liquid salt inlet (bottom left) on the liquid salt pump trip. The same can be seen for the helium pump trip near the helium inlet shown on the right side of Figure 5-9.

Aside from the thick perimeter of the composite plate, another trouble area can be seen in the corners created where the liquid inlet and outlet pipe sections are welded onto the plate. The inner and outer corners generated where the pipes are welded must have generous fillets to avoid the stress concentrations produced there using the current design. Lastly, the sharp right-angled turn in the distributor channels is called a Mitre distributor. This distributor geometry amplifies stresses where the distributors change direction. The high stresses can be seen towards the end of the transient associated with the liquid salt pump trip (60s) shown in Figure 5-8.

The composite plate design failed the transient thermomechanical analysis with yielding stresses on corners and on the plate perimeter. However, with the lessons provided by the methodology presented and with the convergence of CHEETAH and the FEA simulation tools, the areas of the composite plate that are vulnerable to stress have been identified. The design problems are simple and can probably be resolved in the next design iteration. Finally, with the exceptions noted above, the plate-scale analysis shows that for the majority of the composite plate, the transient thermomechanical stresses are manageable, peaking near 50 MPa and leaving a safety factor of at least 2 in most areas.

5.6 Fin-scale Stress Analysis

Plotting the plate-scale principle stresses will show only the *x* or *z* components of the stress distribution rather than the average or Von Mises stresses. With the principle stresses on the plate-scale, the peak stresses in each unit cell region can be selected for both the *x* and *z* directions. The peak principle stresses for each unit cell were found from the plate-scale results and are listed in Table 5-2.

Local principle stresses on unit cells at each temperature state (MPa)

		Unit Cells			
		A	**B**	**C**	**D**
Steady-state (0s)	*x-dir*	16.2	23.7	35.7	43.9
	z-dir	14.8	14.8	14.8	14.8
LS 30 sec	*x-dir*	25	70	35	20
	z-dir	10	30	30	10
He 30 sec	*x-dir*	10	10	15	70
	z-dir	10	50	10	10
LS 60 sec	*x-dir*	10	70	40	25
	z-dir	10	20	20	5.5
He 60 sec	*x-dir*	23	5	20	55
	z-dir	20	60	20	20

Table 5-2: Local principle stresses on unit cells at each temperature state (MPa)

To recreate the plate-scale stresses on each unit cell a model of each unit cell is imported to the FEA software (ANSYS). To replicate the pressure difference across the composite plate, the fluid pressure for the helium (7MPa) is applied to its heat transfer surface while 150 kPa is applied to the heat transfer surface corresponding to the liquid salt surface area. Then, applying the corresponding principle stresses to the *x* and *z* faces from Table 5-2 and constraining the opposite face in each direction, the plate-scale stress state can be recreated on the unit cell. The fin-scale stresses were analyzed in ANSYS with help from Kennth Lee. The stress state for the operating (steady-state) temperature distribution are shown on unit cells A, B, C, and D in Figure 5-10, below.

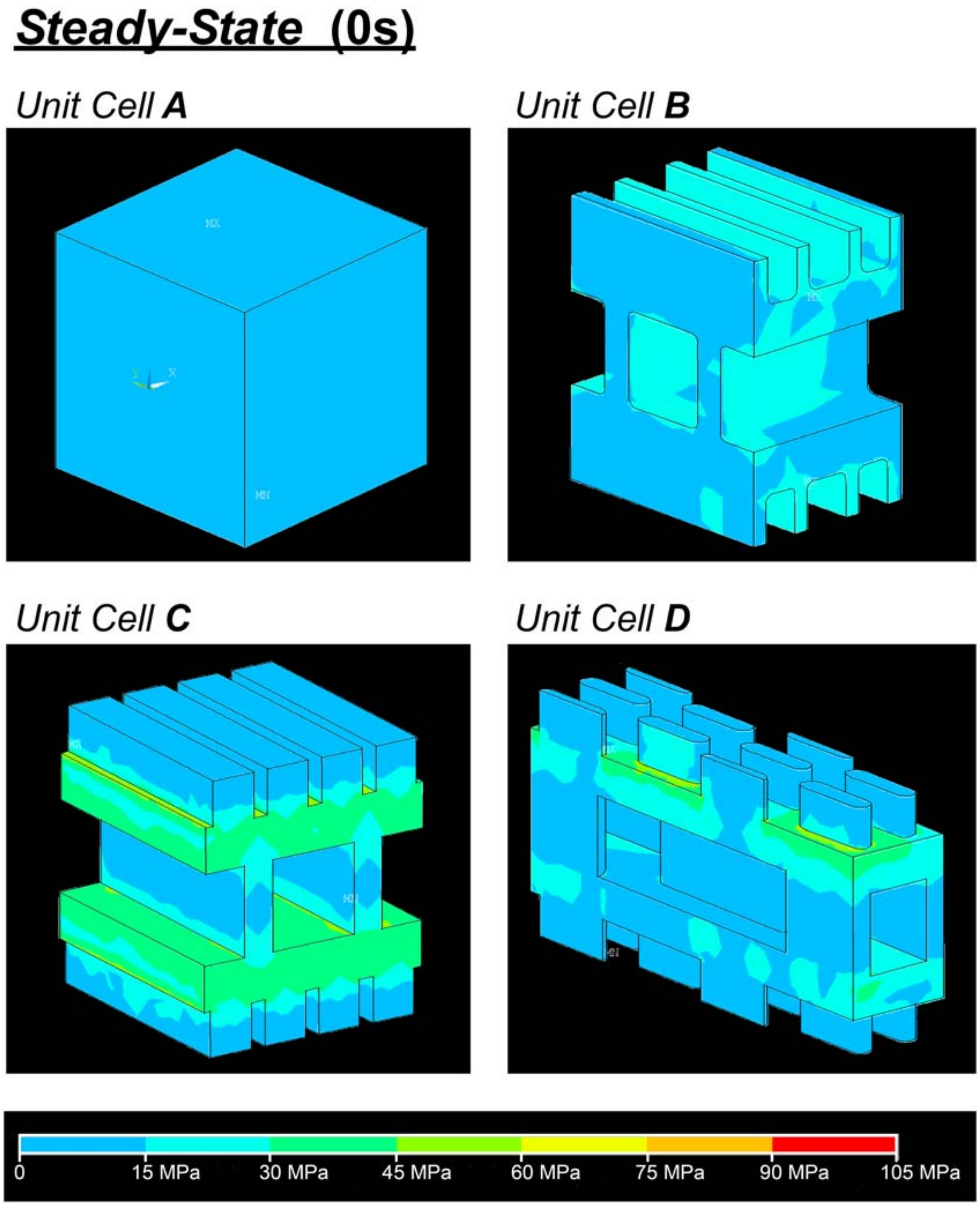

Figure 5-10: Steady-state Von Mises stress distribution on unit cells.

The stresses illustrated in Figure 5-10 show that the composite plate is sufficiently robust to momentarily resist the operational steady-state stresses. Peak stresses occur in the sharp corner regions as expected but even these leave an acceptable safety factor when considering that only unit cells A and B will be close to peak temperatures. Here again, it is the creep resistance that is lacking. Unit cells C and D show stresses significantly above the 16 MPa maximum design stress (2 SF, or safety factor) for Inconel Alloy 617. Like the composite plate, the inclusion of fillets in the unit cells would likely reduce stresses significantly.

5.7 Stress Results from the Helium Pump Trip

The stress state corresponding to 30 seconds after the helium pump trip is obtained by applying the pressure difference on each unit cell in addition to the stresses from Table 5-2. The resulting stress state can be seen on unit cells A, B, C, and D in Figure 5-11, below.

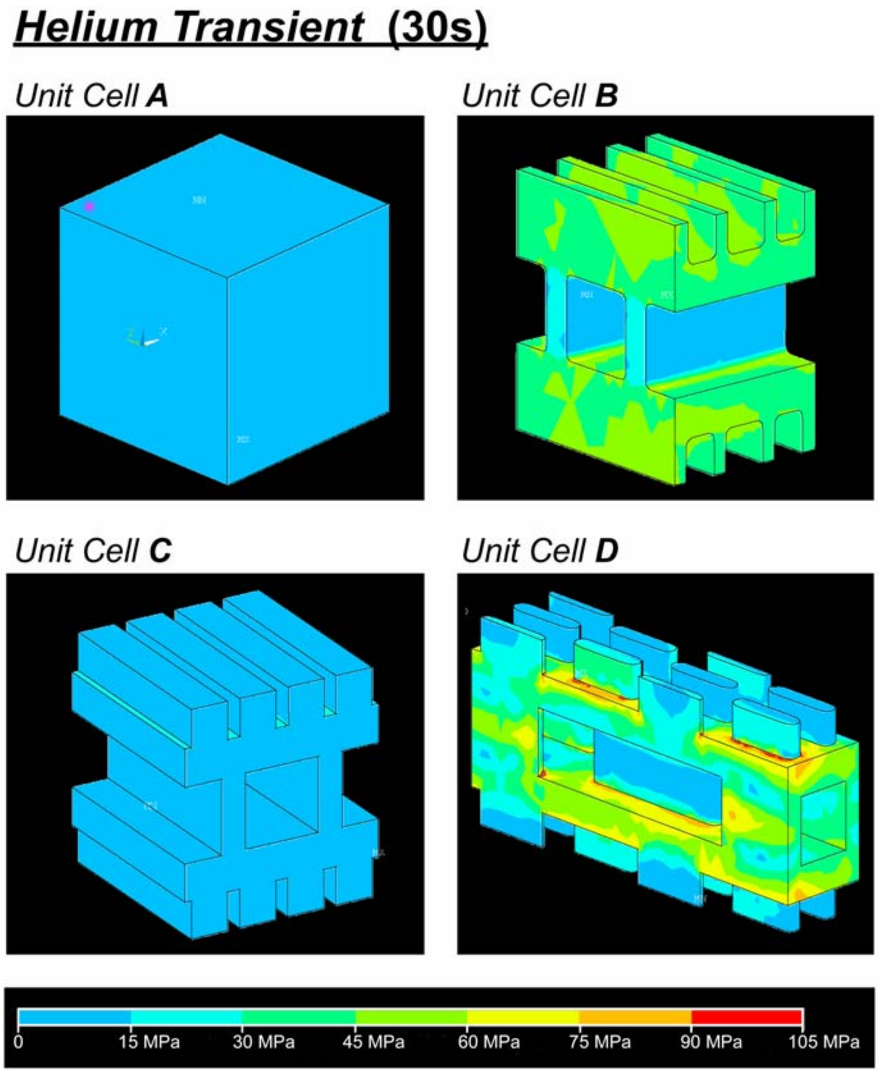

Figure 5-11: Transient Von Mises stress distribution on unit cells 30 seconds after the helium pump trip.

The stress state corresponding to 60 seconds after the helium pump trips can be seen on unit cells A, B, C, and D in Figure 5-12, below.

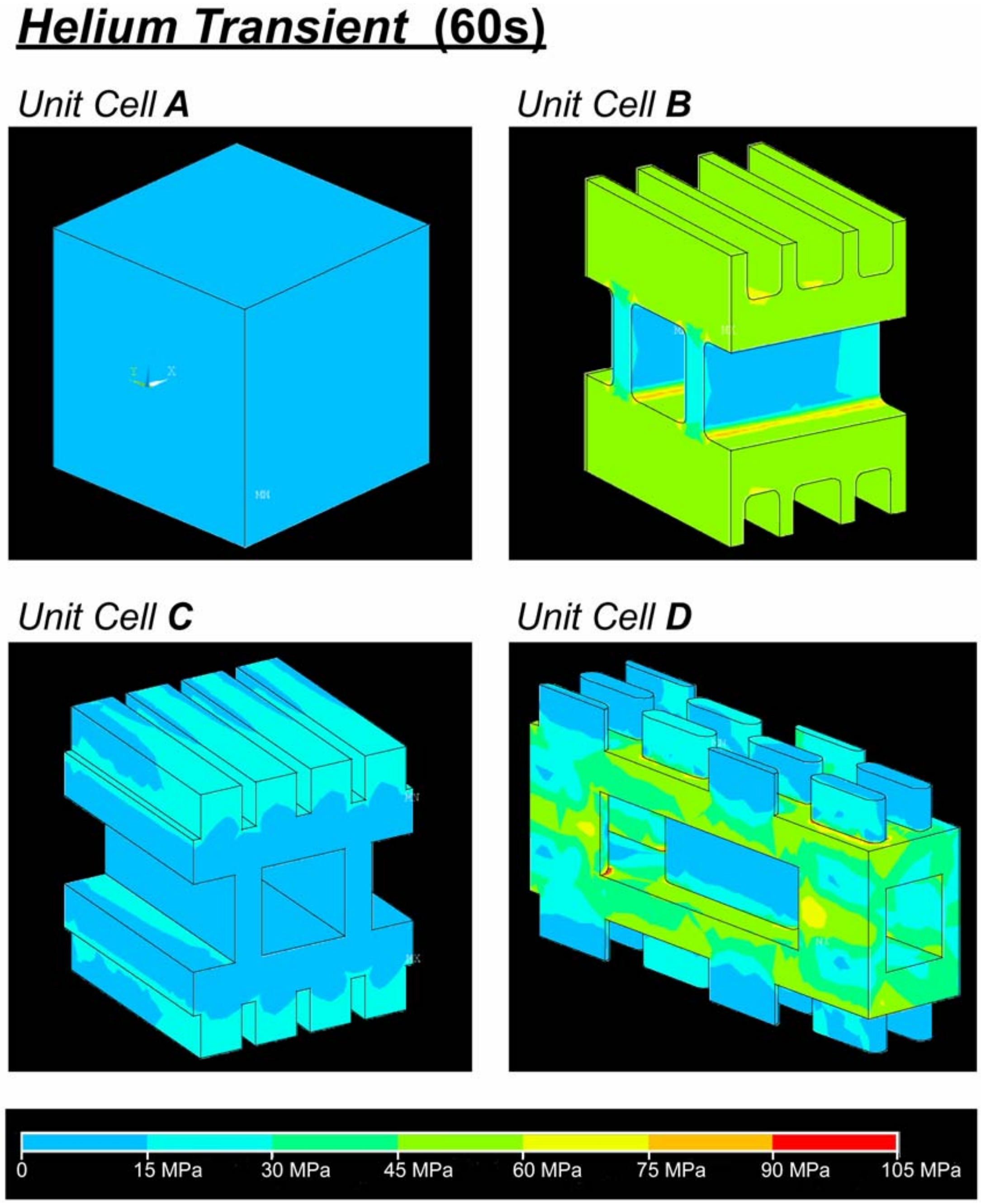

Figure 5-12: Transient Von Mises stress distribution on unit cells 60 seconds after the helium pump trip.

Depending on location (temperature-dependent yield stress) some yielding might occur in unit cell D in the fin roots where the angle creates elevated stresses but generally the unit cells show stresses below the yield stress of 157 MPa. However, the stresses early in the transient are certainly beyond the maximum design yield stress set at 78 MPa; this is especially visible in unit cell D in Figure 5-11.

5.7 Stress Results from the Liquid Salt Pump Trip

The stress state corresponding to 30 seconds after the liquid salt pump trips can be seen on unit cells A, B, C, and D in Figure 5-13, below.

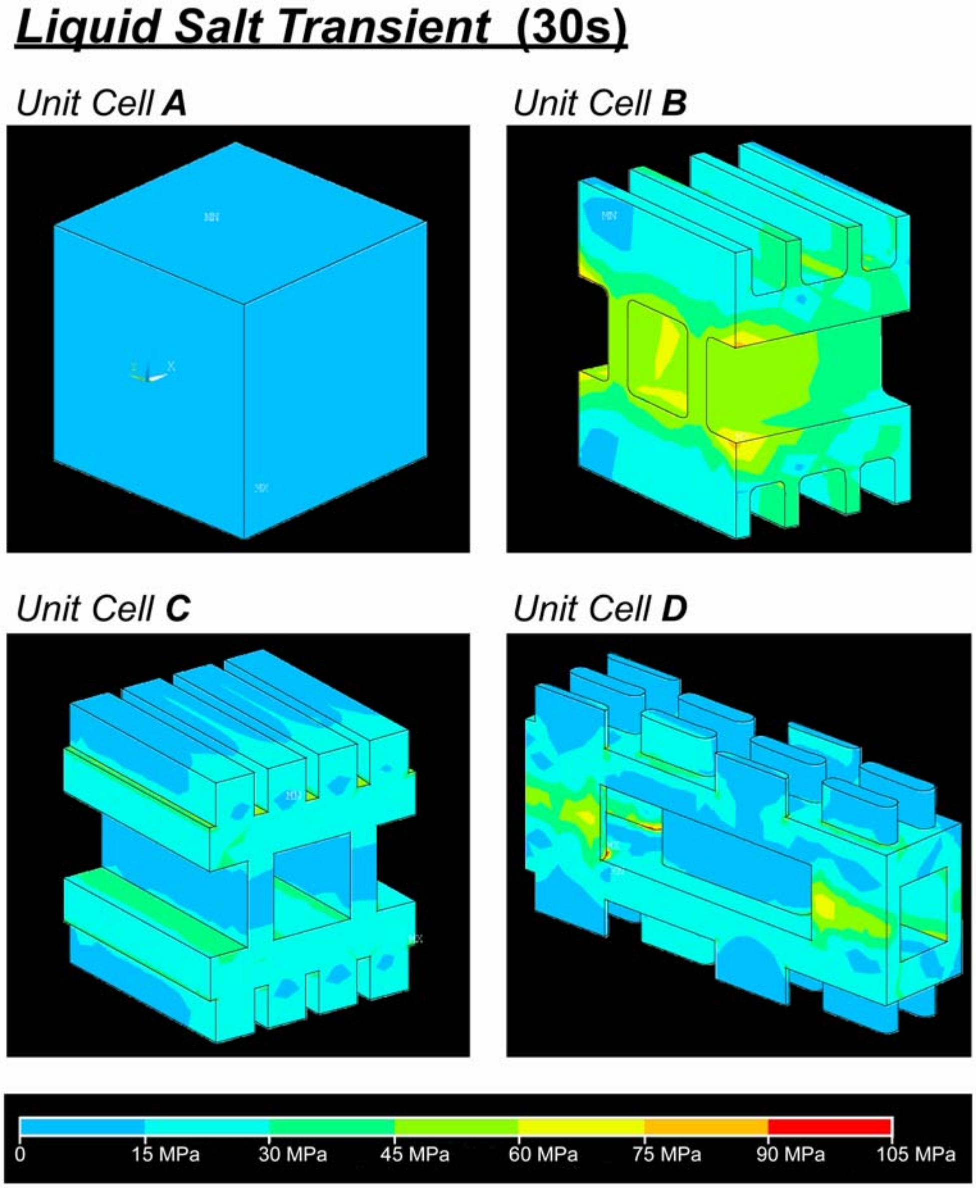

Figure 5-13: Transient Von Mises stress distribution on unit cells 30 seconds after the liquid salt pump trip.

The stress state corresponding to 60 seconds after the liquid salt pump trips can be seen on unit cells A, B, C, and D in Figure 5-14, below.

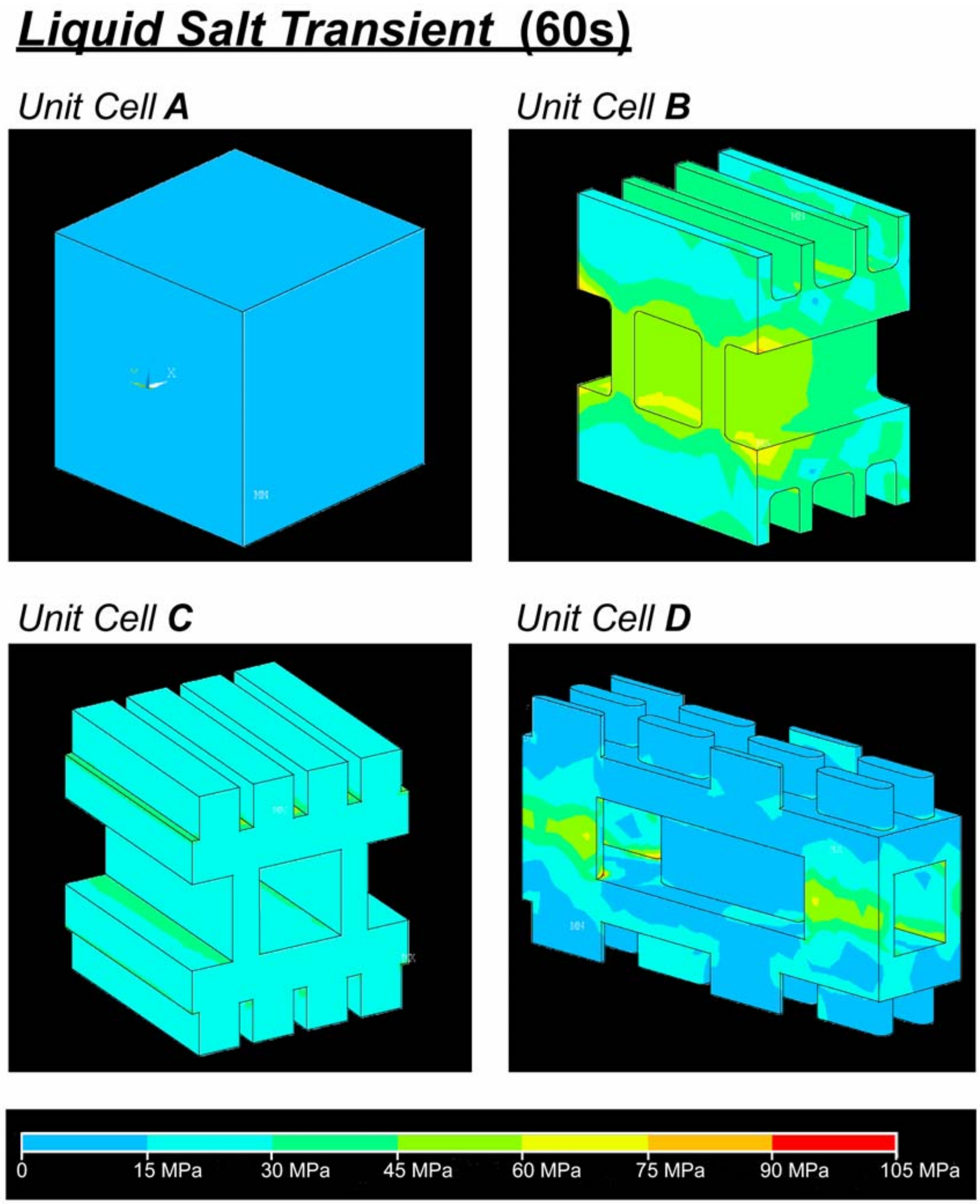

Figure 5-14: Transient Von Mises stress distribution on unit cells 60 seconds after the liquid salt pump trip.

The liquid salt pump trip shows thermomechanical stresses that are more moderate than those associated with the helium pump trip. The stresses do not appear large enough to cause yielding; however, the maximum design stress of 78 MPa (SF 2) is exceeded. By including fillets in the fin roots the geometries in these unit cells can be made to resist the transient thermomechanical stresses associated with a liquid salt pump trip.

Chapter 6

Conclusions and Recommendations

6.1 Recommendations Regarding Example Problem

From the mechanical results presented in the previous chapter it is clear that at peak temperatures of 1200 K, Inconel Alloy 617 retains a formidable yield stress of 157 MPa. The results provided by CHEETAH and ANSYS show that this is sufficient to resist the very severe thermo-mechanical transient caused by the liquid salt and helium pump trips. This is particularly notable since these pump failures are modeled as a 98% step down in flow of one of the fluids which produces a deeply unbalanced counter-flow condition in the IHX.

6.1.1 System Recommendations

One possibility to reduce the severity of thermal hydraulic transients associated with pump failure or trip would be to include large flywheels on the centrifugal pump axels. This would add rotational inertia to the system making the pump output ramp down more gradually and thus reduce the shock associated with a more abrupt change in flow rate. The size of the flywheels will depend on the vulnerability of the entire loop to flow and thermal transients and will require detailed analysis to determine. CHEETAH can contribute with the thermal hydraulic results associated with the compact heat exchangers in the system.

Another idea to reduce the intensity of these types of flow transients involves installing a pump trip relay that would automatically trip the counter-flow pump when one pump trips. By tripping both pumps simultaneously the temperature transient on the heat exchanger can be significantly reduced. Currently the trip of just one pump causes a severe transient because the counter-flowing fluid continues to remove or deposit thermal energy without adjusting to the conditions on the opposite side of the composite plate. The simultaneous trip would help keep a thermal balance on the temperature distribution while conduction effects more slowly take the system to thermal equilibrium.

Placing several shorter intermediate heat exchangers in series would reduce the temperature change over any one heat exchanger significantly. The illustrative example analyzed must endure a temperature change of 300°C from one end to the other; placing three smaller heat exchangers in series could obtain the same total temperature drop but with only a 100°C temperature change in each device. Lastly, the first heat exchanger contacting the hot helium gas could have a specialized design, such as a bayonette or shell and tube design to better cope with the creep stresses at high temperature while the rest of the heat exchangers could be plate-type diffusion bonded heat exchangers like the one presented in this illustrative example.

6.1.2 Hydraulic Recommendations

The selection of helium as a coolant in constant heat flux and high temperature applications must be accompanied by careful thermal hydraulic analysis particularly because the viscosity of helium gas rises with increasing temperatures [16]. This fact is particularly important with regard to the formation and grown of hot spots in a high temperature component cooled by helium. Hotter areas will increase local helium gas coolant temperatures and viscosities, thereby decreasing coolant flow rates and creating positive thermal feedback that leads to continuously increasing local temperatures. In the illustrative example analyzed the intermediate heat exchanger used high pressure helium not as the coolant but rather as the hot fluid. However, on the opposite side of that hot loop the high pressure helium is the coolant in the modular helium reactor (MHR). This is a case where careful consideration of temperature dependant fluid properties is paramount.

Another complication from helium concerns its low volumetric heat capacity relative to the liquid salt. This entails that the helium be used at high pressure to increase its density and it means that large flow rates are required in the helium side of the composite plate. High flow rates demand relatively high pumping power be expended on the helium flow compared to that in the liquid salt flow. The low volumetric heat capacity of helium also necessitates a large temperature rise in the helium compared to that of the liquid salt. The large temperature and pressure difference between fluids is responsible for the large stresses in the IHX which must be resisted at high temperature. Optimally, a high temperature heat exchanger would operate between fluids operating with a low pressure difference between them and with a more moderate temperature change between inlet and outlet.

6.1.3 Mechanical Recommendations

The mechanical stress analysis in Chapter 5 highlights an important trend in the vulnerability of the composite plate. The stress plots (Figures 5-5, 5-6, and 5-7) resulting from the thermal hydraulic analysis using CHEETAH demonstrate that the there are fundamentally two phenomena that threaten the integrity of the composite plate; these are transient yielding and operational creep deformation. In both cases stresses concentrate on the perimeter of the composite plate but the reasons for stress intensity are different.

Regarding transient yielding stress, the CHEETAH code shows that large temperature gradients are associated with the thicker sections in the composite plate. These are sections that have a high thermal inertia (100% solid phase fraction) and only exchange heat by conduction, which means that they take longer to equilibrate than the sections in direct contact with the heat transfer fluids which can exchange heat via both conduction and convection. Thick walls dominate the perimeter of the composite plate, reducing the thickness of this perimeter will likely solve the transient yielding stress problem with this heat exchanger. This hypothesis can be tested by subjecting a redesigned composite plate to the same thermal hydraulic analysis with CHEETAH as the one performed on the composite plate geometry presented in this study. A redesigned plate that addresses these and other issues can be seen below in Figure 6-1.

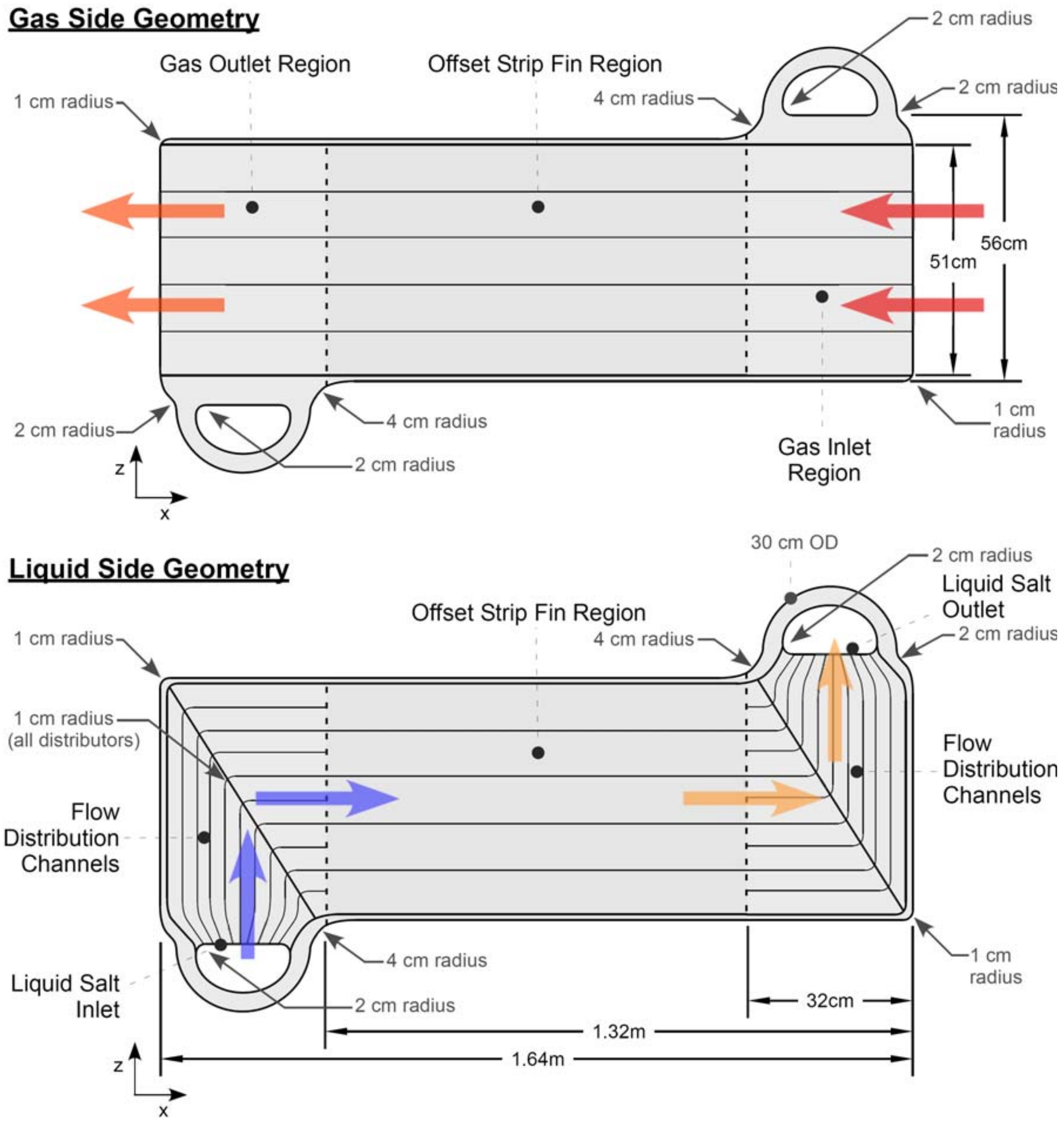

Figure 6-1: New composite plate design improved with information provided through CHEETAH and FEA analysis.

In evaluating creep stresses, the steady state temperature and stress distribution are relevant and can be seen in Figure 5-4 and Figure 5-5. The latter shows peak stresses occurring at the corners created by the union of the composite plate with the semi-circular liquid salt manifolds as well as in the areas where the plate thickness is significantly reduced. These stresses can be avoided with large fillets in the corners between pipe manifolds and rectangular plates. Furthermore, the reduction in plate thickness between the liquid slat manifold and the side of the composite plate must be executed more gradually culminating in thinner sections as can be seen in the redesigned composite plate shown in Figure 6-1, above.

The steady state or operational temperature gradients in the composite plate that are relevant for the creep analysis are quite mild. Still, flow maldistribution in the OSF region creates some temperature gradients large enough to create thermo-mechanical stresses above the design limit for creep which is set at 16 MPa. In order to avoid this mode of failure, the OSF section could be divided into six flow zones rather than the current five. This would reduce the difference in velocities from the inside to outside corner of each flow zone that can be seen as ridges in Figure 3-4 and Figure 3-13. Additionally, the OSF geometry must be made more robust. This can be done by significantly reducing the gas and liquid fin heights and by including large fillets at the base of fins and in channels. Shortening fins will increase the number of plates in an IHX assembly while modifications to include large fillets will have the side benefit of reducing flow friction in the OSF region to the detriment of heat transfer.

Yet another option is to avoid the creep problems all together by using a material with a larger yield stress at the peak temperatures of 1200 K (927°C). Ceramics would offer the creep resistance but may be more vulnerable to thermo-mechanical transients.

Research at UC Berkeley has explored the possibility of making a compact IHX out a silicon-carbide based ceramic material via a molding process [26].

6.2 Conclusions

The previous chapters have covered a multi-scale thermal, hydraulic, and mechanical analysis of a high temperature compact intermediate heat exchanger. This work characterized the heat exchanger's internal geometry by analyzing a representative composite plate which includes geometry from both gas and liquid plates. This composite plate was further parsed into several zones containing unique geometrical configurations including repetitive small scale features. Unit cells containing these features which are also representative of the zones from which they were obtained are then analyzed and their effective thermal, hydraulic, and mechanical properties are derived. A separate model is build based on these effective or volume averaged properties; this model is analyzed using an FVA code developed for this purpose called Compact Heat Exchanger Explicit and Hydraulics (CHEETAH) code.

The model analyzed in CHEETAH is designed to capture the phenomena created by the small features in the original heat exchanger without forcing discretization at this small scale. The steady state and transient thermal hydraulic response of this system was analyzed in CHEETAH using modest computational resources. These results lead to thermal hydraulic optimization of the heat exchanger and also to a multi-scale mechanical analysis in ANSYS that identifies the more vulnerable areas of the design so that they can be improved.

This method and its implementation in CHEETAH enable the transient thermal hydraulic computation of a complex system containing descriptive dimensions too small to discretize individually. The CHEETAH code bridges multiple scales to effectively analyze at the component scale (composite plate).

This method does have its limitations, however. Yet more work is required to improve usability and to facilitate the adaptability of the code to different geometries. Also, by performing a volume average of fin-scale effects the variation in performance at that is dependent on the correlation used to define volume averaged behavior rather than on first principles. Furthermore, discontinuities in properties occur at the boundaries between zones with effective properties, and while the distortions in this case are small, if the analysis were searching for subtle effects, the distortions could dominate. Finally, just as the ability to discretize at a larger scale enables faster and transient analyses it also means limits the resolution of the thermal hydraulic data obtained.

In conclusion, the successful application of this code to the example problem shows the potential of carefully undertaken volume averaging. The CHEETAH code is a tool that together with FEA software can help designers and researchers analyze and optimize the thermal, hydraulic, and mechanical performance of a plate-type compact heat exchanger. The code also readily provides insightful performance data regarding the effects of temperature dependent fluid properties on flow distribution in a high temperature heat exchanger. Lastly, the results from CHEETAH can be used to provide boundary conditions for an analysis at a smaller scale. Subsequent analyses at a smaller scale can be executed using CFD or by adapting the algorithms used in CHEETAH to detailed geometry at the new scale with appropriate local volume averaging.

References

[1] Urquiza-Fernández E., Peterson P. F. and R. Greif. "Multi-Scale Thermal Analysis for Compact Plate-Type Heat Exchangers." *American Institute of Chemical Engineering Annual Meeting*, Salt Lake City, UT, November 4-9, 2007.

[2] Huang W., Zhao H. and P. F. Peterson. "Multi-scale Stress Analysis for Compact Plate Heat Exchangers." *2006 International Congress on Advances in Nuclear Power Plants (ICAPP 2006)*, Reno, NV, June 4-8, 2006.

[3] Dewson S. J. and B. Thonon. The Development of High Efficiency Heat Exchangers for Helium Gas Cooled Reactors (Paper No. 3213). 2003 International Congress on Advances in Nuclear Power Plants (ICAPP 2003).

[4] Williams D. F. et al. *Assessment of Candidate Molten Salt Coolants for the Advanced High-Temperature Reactor (AHTR)*; ORNL/TM-2006/12; Oak Ridge National Laboratory, Oak Ridge, TN, March 2006.

[5] Peaceman, D. W., *Fundamentals of Numerical Reservoir Simulation.* Elsevier, 1977. ISBN 0444415785, 9780444415783

[6] Domenico, P. A. and F. W. Schwartz, *Physical and Chemical Hydrogeology.* University of Michigan: Wiley & Sons, 1990

[7] Ponyavin, V. et al., "The Flow Calculation in the High Temperatured Heat Exchanger with the Manufactring geometrical Effects." *Proceedings of the 2005 Summer Heat Transfer Conference*, San Francisco, CA, USA.

[8] Hu, S. and K. E. Herold. "Prandtl number effect on offset fin heat exchanger performance: predictive model for heat transfer and pressure drop." *Int. J. Heat Mass Transfer* 38, No. 6 (1995): 1043-1051.

[9] Kays W. M. and A. L. London. *Compact Heat Exchangers*. 3rd ed., New York, NY: McGraw-Hill, 1984.

[10] Manglik R. M. and A. E. Bergles. “Heat Transfer and Pressure Drop Correlations for the Rectangular Offset Strip Fin Compact Heat Exchanger.” *Experimental Thermal and Fluid Science* 10 (1995): 171-180.

[11] Fox R. W. and A. T. McDonald. *Introduction to Fluid Mechanics*. 3rd ed., Wiley & Sons, 1985.

[12] Kays, W. M., “Compact Heat Exchangers,” AGARD Lecture Ser. No. 57 on Heat Exchangers, AGARD-LS-57-72, NATO, Paris, 1972.

[13] Sparrow E.M., B.R. Baliga and S.V. Patankar, “Heat transfer and fluid flow analysis of interrupted-wall channels with application to heat exchangers,” *J. Heat Transfer* 22, 1613-1625 (1977).

[14] Kelkar K.M. and S.V. Patankar, “Numerical prediction of heat transfer and fluids flow sin rectangular offset-fin arrays,” *Numerical Heat Transfer* A 15, 149-164 (1989).

[15] Anderson D. A., J.C. Tannehill, and R. H. Pletcher. *Computational Fluid Mechanics and Heat Transfer*. New York, NY: McGraw-Hill, 1984.

[16] National Institute for Standards and Technology, NIST. www.nist.gov.

[17] Mills A. F. *Heat and Mass Transfer*. Concord, MA: Irwin, 1995.

[18] Incropera F. and D. P. DeWitt. *Fundamentals of Heat and Mass Transfer*. 5th ed., Wiley & Sons, 2002.

[19] Çengel Y. A. and R. H. Turner. *Thermal-Fluid Sciences*. New York, NY: McGraw-Hill, 2001.

[20] Patankar S.V. *Numerical Heat Transfer and Fluid Flow*. New York, NY: McGraw-Hill, 1980.

[21] Yin J. and M. K. Jensen. "Analytic Model for Transient Heat Exchanger Response." *Int. J. Heat Mass Transfer* 46 (2003): 3255-3264.

[22] F.E. Romie, "Transient response of the counterflow heat exchanger," *J. Heat Transfer* 106 (3) (1984) 620–626.

[23] W. Roetzel, Y. Xuan, "Transient response of parallel and counterflow heat exchangers," *J. Heat Transfer* 114 (2) (1992) 510–512.

[24] Boresi, A.P. and R.J. Schmidt. *Advanced Mechanics of Materials.* Wiley & Sons, 2003.

[25] Haynes International, Inc., "Heat-resistant alloy-at-a-glance: Haynes 617 alloy." http://www.haynesintl.com.

[26] Peterson P. F., Zhao H., Niu F. and W. Huang, Schmidt J. and J. Schulte-Fischedick. "Development of C-SiC ceramic compact plate heat exchangers for high temperature heat transfer applications." *American Institute of Chemical Engineering Annual Meeting*, San Francisco, CA, November 12-16, 2006.

Appendix A

Intermediate Heat Exchanger Sizing Calculations

Mathcad spreadsheet design by Dr. Hai Hua Zhao

Modified by Eugenio Urquiza

Flow channel geometries:

Unit Cell D - Offset strip fin region of the IHX

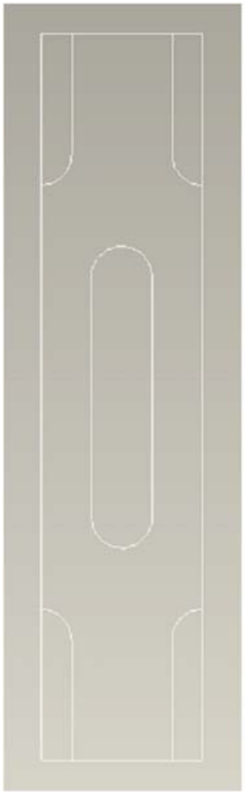

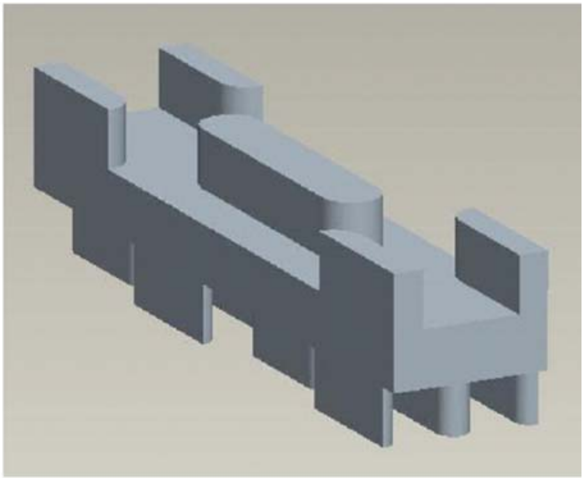

effective fin thickness coefficient: $C_{fin} := 0.5$

effective fin thickness coefficient: $C_{fin} := 0.5$

Hot side (helium): subscript h indicates hot channel (helium side)

Each channel cell includes a complete fin and and two half fins.

channel height: $height_h := 5.\cdot mm$ fin thickness: $t_h := 5mm$

fin length: $l_h := 20.mm$ pitch in x direction: $P_{xh} := 15.mm$

pitch in y direction: $P_{yh} := l_h + 4mm$

Hydraulic diameter:

$$D_h(height_h) := 2\cdot\frac{height_h}{1 + height_h\cdot\frac{l_h + t_h}{P_{xh}\cdot P_{yh} - t_h\cdot l_h}} \qquad D_h(height_h) = 6.75325\times10^{-3}\,m$$

unit flow cross section area for each cell:

$$ac_h(height_h) := (P_{xh} - t_h)\cdot height_h \qquad ac_h(height_h) = 5.00000\times10^{-5}\,m^2$$

unit heat transfer areas for each cell:

Heat transfer area for the base wall surface:

$$aw_{wall} := 2\cdot(P_{xh}\cdot 2\cdot P_{yh} - 2\cdot t_h\cdot l_h) \qquad aw_{wall} = 1.04000\times10^{-3}\,m^2$$

Heat transfer area for the fin surface:

$$aw_{finh}(height_h) := 4\cdot(l_h + t_h)\cdot height_h \qquad aw_{finh}(height_h) = 5.00000\times10^{-4}\,m^2$$

Total heat transfer area for a cell:

$$aw_h(height_h) := aw_{wall} + aw_{finh}(height_h) \qquad aw_h(height_h) = 1.54000\times10^{-3}\,m^2$$

Volume of a cell: $vol\_cell_h := P_{yh}\cdot P_{xh}\cdot height_h$ $vol\_cell_h = 1.80000\times10^{-6}\,m^3$

Surface Area to Vol Ratio: $SA\_Vol := \frac{aw_h(height_h)}{vol\_cell_h}$ $SA\_Vol = 855.55556\,\frac{1}{m}$

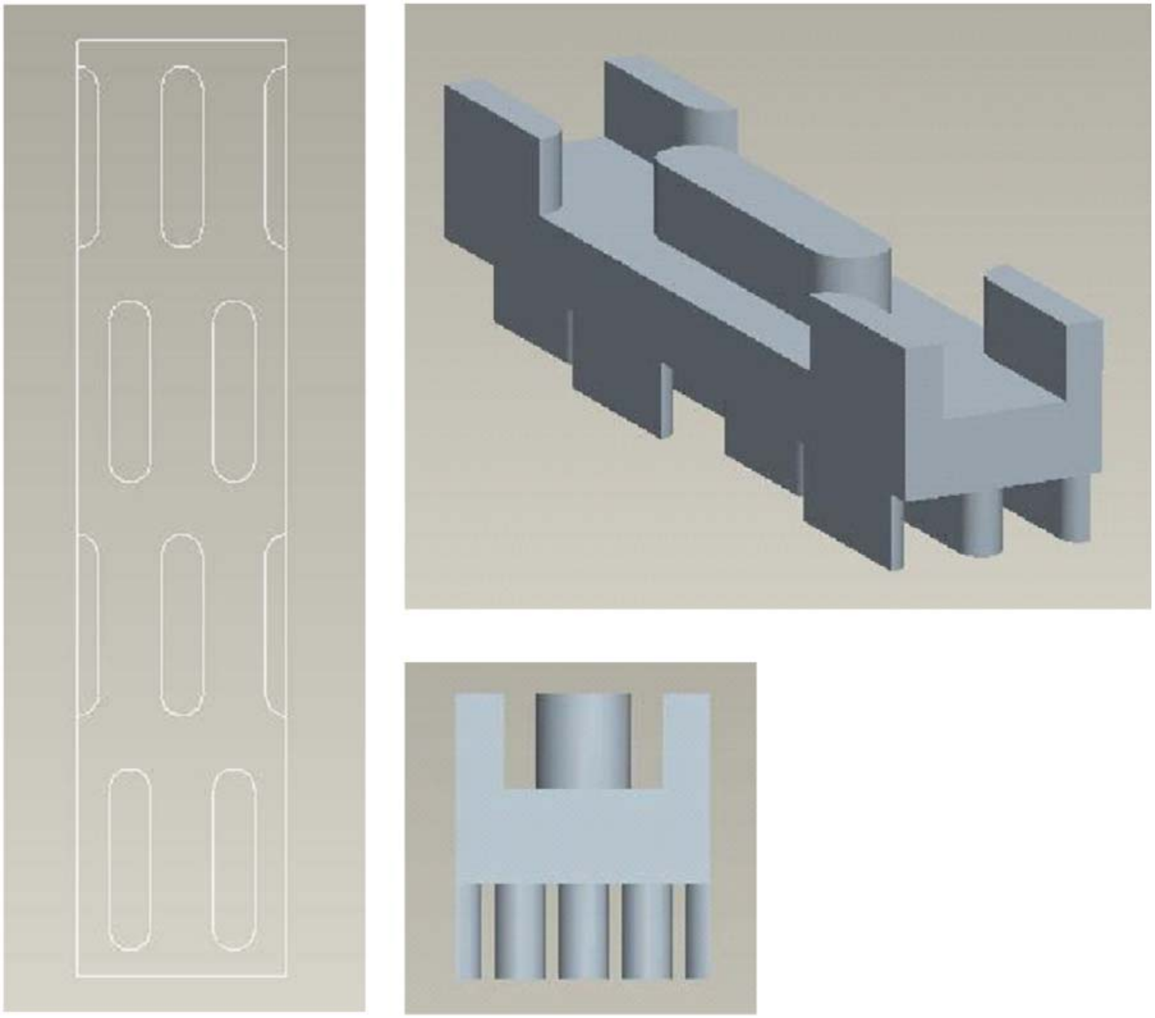

Molten salt side(cold side):

subscript c indicates the cold side

channel height: $height_c := 3.\cdot mm$ fin thickness: $t_c := 4mm$

fin length: $l_c := l_h$ pitch in x direction: $P_{xc} := P_{xh}$

pitch in y direction: $P_{yc} := P_{yh}$

hydraulic diameter:

$$D_c := 2\cdot\frac{height_c}{1 + height_c\cdot\frac{l_c + t_c}{P_{xc}\cdot P_{yc} - t_c\cdot l_c}}$$

$$D_c = 4.77273 \times 10^{-3}\,m$$

unit effective or flow cross section area
for each cell:

$ac_c(height_c) := (P_{xc} - t_c) \cdot height_c$ $\qquad ac_c(height_c) = 3.30000 \times 10^{-5}\,m^2$

Unit heat transfer areaes for each cell:

Heat transfer area for the fin surface:

$aw_{finc} := 4 \cdot (l_c + t_c) \cdot height_c$ $\qquad aw_{finc} = 2.88000 \times 10^{-4}\,m^2$

Total heat tranfer area for a cell:

$aw_c := aw_{wall} + aw_{finc}$ $\qquad aw_c = 1.32800 \times 10^{-3}\,m^2$

Volume of a cell: $vol\_cell_c := P_{yc} \cdot P_{xc} \cdot height_c$ $\qquad vol\_cell_c = 1.08000 \times 10^{-6}\,m^3$

Surface Area to Vol Ratio: $SA\_Vol := \frac{aw_c}{vol\_cell_c}$ $\qquad SA\_Vol = 1.22963 \times 10^{3}\,\frac{1}{m}$

`Thickness of material between cold and hot channels:` `1.0 mm`

$t_{wall} := 2.0mm$

3. Thermal parameters design:

$MW := 10^6 W$ $\qquad MPa := 10^6 Pa$

Thermal power : $Power_{ihx} := 50MW$

Helium side pressure: $P_h := 7.06MPa$ $\qquad$ System pressure: $P_0 := 7.12MPa$

Hot side inlet temperature: $T_{1i} := 1000K + 273.15K$ $\qquad T_{1i} = 1.27315 \times 10^3\,K$

Hot side outlet temperature: $T_{1o} := 632K + 273.15K$ $\qquad T_{1o} = 905.15000\,K$

Cold side inlet temperature: $T_{2i} := 560K + 273.15K$ $\qquad T_{2i} = 833.15000\,K$

Cold side outlet temperature: $T_{2o} := 975K + 273.15K$ $\qquad T_{2o} = 1.24815 \times 10^3\,K$

$\Delta T_c := T_{2o} - T_{2i}$ $\qquad \Delta T_c = 415.00000\,K$

$\Delta T_h := T_{1i} - T_{1o}$ $\qquad \Delta T_h = 368.00000\,K$

$\Delta T_i := T_{1i} - T_{2o}$ $\qquad \Delta T_i = 25.00000\,K$

$\Delta T_o := T_{1o} - T_{2i}$ $\qquad \Delta T_o = 72.00000\,K$

LMTD : $\Delta T_m := \dfrac{\Delta T_o - \Delta T_i}{\ln\left(\dfrac{\Delta T_o}{\Delta T_i}\right)}$ $\Delta T_m = 44.43225\,K$

Thermal effectiveness: $\varepsilon_{ihx} := \dfrac{\max(\Delta T_h, \Delta T_c)}{T_{1i} - T_{2i}}$ $\varepsilon_{ihx} = 0.94318$

Hot side (helium) channel thermal calculation:

Velocity calculation:

mass flow rate of helium: $mfr_{He} := \dfrac{Power_{ihx}}{c_{pHe} \cdot \Delta T_h}$ $mfr_{He} = 26.16398\,\dfrac{kg}{s}$

volumetric flow rate of helium: $Q_h := \dfrac{mfr_{He}}{\rho_{He}\left(P_h, \dfrac{T_{1i} + T_{1o}}{2}\right)}$ $Q_h = 8.48930\,\dfrac{m^3}{s}$

Total helium side frontal area of face: $A\_face_h := 5m^2$ $\phi_{fh} := \dfrac{\dfrac{ac_h(height_h)}{2}}{\left(\dfrac{height_h}{2} + t_{wall} + \dfrac{height_c}{2}\right) \cdot P_{xh}}$ $\phi_{fh} = 0.27778$

Total helium side frontal effective or flow area: $Ac_h := A\_face_h \cdot \phi_{fh}$ $Ac_h = 1.38889\,m^2$

total number of flow channels in front: This divides the total effective or flow area on the HX face by the effective or flow area for unit cell D

$$n_{front.h} := \frac{Ac_h}{ac_h(height_h)}$$

$n_{front.h} = 2.77778 \times 10^4$ $n_{stack} := 250$ The number of composite plates in the stack

$height_{comp\_p} := \left(\dfrac{height_c}{2} + \dfrac{height_h}{2} + t_{wall}\right)$ $height_{comp\_p} = 6.00000 \times 10^{-3}\,m$

$height_{IHX} := n_{stack} \cdot height_{comp\_p}$ $height_{IHX} = 1.50000\,m$

$width_{comp\_p} := \dfrac{A\_face_h}{height_{IHX}}$ $width_{comp\_p} = 3.33333\,m$

$width_{comp\_p} := \dfrac{2n_{front.h} \cdot P_{xc}}{n_{stack}}$ 2.n_front_c is used because it takes 2 composite plates to make one flow channel

$width_{comp\_p} = 3.33333\,m$

This is an alternate method of getting the width

$height_{IHX} := \dfrac{A\_face_h}{width_{comp\_p}}$ $height_{IHX} = 1.50000\,m$

Helium average Darcy (advection term) velociy:

$u_{darcy\_h}(Ac_h) := \dfrac{Q_h}{A\_face_h}$ $u_{darcy\_h}(Ac_h) = 1.69786\,\dfrac{m}{s}$

Helium average interstitial velocity:

$$u_h(Ac_h) := \frac{Q_h}{Ac_h} \qquad\qquad u_h(Ac_h) = 6.11230\,\frac{m}{s}$$

Heat transfer and friction calculation:

$$Re_h(height_h, Ac_h) := \frac{u_h(Ac_h)\cdot D_h(height_h)}{\nu_{He}\left(P_h, \frac{T_{1i} + T_{1o}}{2}\right)} \qquad\qquad Re_h(height_h, Ac_h) = 2.59089 \times 10^{3}$$

Heat transfer equation by Manglik&Bergles:

$$\alpha_h(height_h) := \frac{P_{xh} - t_h}{height_h} \qquad\qquad \alpha_h(height_h) = 2.00000$$

$$\delta_h := \frac{C_{fin} t_h}{P_{vh}} \qquad\qquad \delta_h = 0.10417$$

$$\gamma_h := \frac{C_{fin}\cdot t_h}{P_{xh} - t_h} \qquad\qquad \gamma_h = 0.25000$$

$$j_h(height_h, Ac_h) := \left| \begin{array}{l} A \leftarrow 0.6522\cdot\left(\alpha_h(height_h)^{-0.1541}\cdot\delta_h^{\,0.1499}\cdot\gamma_h^{\,-0.0678}\right)\cdot Re_h(height_h, Ac_h)^{-0.5403} \\ B \leftarrow \left(1 + 5.269\cdot 10^{-5}\cdot\alpha_h(height_h)^{0.504}\cdot\delta_h^{\,0.456}\cdot\gamma_h^{\,-1.055}\cdot Re_h(height_h, Ac_h)^{1.340}\right)^{0.1} \\ A\cdot B \end{array} \right.$$

$$j_h(height_h, Ac_h) = 7.75912 \times 10^{-3}$$

$$f_h(height_h, Ac_h) := \left| \begin{array}{l} A \leftarrow 9.6243\cdot\alpha_h(height_h)^{-0.1856}\,\delta_h^{\,0.3053}\,\gamma_h^{\,-0.2659}\cdot Re_h(height_h, Ac_h)^{-0.7422} \\ B \leftarrow \left(1 + 7.669\cdot 10^{-8}\cdot\alpha_h(height_h)^{0.920}\cdot\delta_h^{\,3.767}\,\gamma_h^{\,0.236}\cdot Re_h(height_h, Ac_h)^{4.429}\right)^{0.1} \\ A\cdot B \end{array} \right.$$

$$f_h(height_h, Ac_h) = 0.04989$$

flow area goodness factor: $goodness_h(height_h, Ac_h) := \frac{j_h(height_h, Ac_h)}{f_h(height_h, Ac_h)}$ $\qquad goodness_h(height_h, Ac_h) = 0.15553$

For offset strip fin channel:

$$Nu_h(height_h, Ac_h) := j_h(height_h, Ac_h)\cdot Re_h(height_h, Ac_h)\cdot Pr_{He}\left(P_h, \frac{T_{1i} + T_{1o}}{2}\right)^{\frac{1}{3}} \qquad\qquad Nu_h(height_h, Ac_h) = 17.49609$$

For smooth channel:

$$Nu_{h0}(height_h, Ac_h) := 0.023\cdot Re_h(height_h, Ac_h)^{0.8}\cdot Pr_{He}\left(P_h, \frac{T_{1i} + T_{1o}}{2}\right)^{0.33} \qquad\qquad Nu_{h0}(height_h, Ac_h) = 10.78375$$

Heat transfer augumentation by offset arrangement:

$$E_h(\mathrm{height}_h, Ac_h) := \frac{Nu_h(\mathrm{height}_h, Ac_h)}{Nu_{h0}(\mathrm{height}_h, Ac_h)} \qquad E_h(\mathrm{height}_h, Ac_h) = 1.62245$$

Heat transfer coefficient for helium side:

$$h_h(\mathrm{height}_h, Ac_h) := Nu_h(\mathrm{height}_h, Ac_h)\cdot\frac{k_{He}\left(P_h, \frac{T_{1i} + T_{1o}}{2}\right)}{D_h(\mathrm{height}_h)} \qquad h_h(\mathrm{height}_h, Ac_h) = 1.00209 \times 10^3 \,\frac{\mathrm{kg}}{\mathrm{K}\cdot\mathrm{s}^3}$$

fin efficiency:

$$mh_h(\mathrm{height}_h, Ac_h) := \sqrt{2\cdot\frac{h_h(\mathrm{height}_h, Ac_h)}{k_{LSI}\, t_h}}\cdot\frac{\mathrm{height}_h}{2} \qquad mh_h(\mathrm{height}_h, Ac_h) = 0.35392$$

$$\eta_{finh}(\mathrm{height}_h, Ac_h) := \frac{\tanh(mh_h(\mathrm{height}_h, Ac_h))}{mh_h(\mathrm{height}_h, Ac_h)} \qquad \eta_{finh}(\mathrm{height}_h, Ac_h) = 0.96024$$

overall surface efficiency:

$$\eta_{h0}(\mathrm{height}_h, Ac_h) := \frac{aw_{wall} + \eta_{finh}(\mathrm{height}_h, Ac_h)\cdot aw_{finh}(\mathrm{height}_h)}{aw_h(\mathrm{height}_h)} \qquad \eta_{h0}(\mathrm{height}_h, Ac_h) = 0.98709$$

Cold side(Molten Salt) thermal calculation:

mass flow rates of MS: $mfr_{MS} := \frac{\mathrm{Power}_{ihx}}{c_{pMS}\cdot\Delta T_c}$ $\qquad mfr_{MS} = 51.48800\,\frac{\mathrm{kg}}{\mathrm{s}}$

volumetric flow rates of MS: $Q_c := \frac{mfr_{MS}}{\rho_{MS}}$ $\qquad Q_c = 0.02783\,\frac{\mathrm{m}^3}{\mathrm{s}}$

Total MS side frontal area of face: $A\_face_c := A\_face_h$

$$\phi_{fc} := \frac{\frac{ac_c(\mathrm{height}_c)}{2}}{\left(\frac{\mathrm{height}_h}{2} + t_{wall} + \frac{\mathrm{height}_c}{2}\right)\cdot P_{xc}} \qquad \phi_{fc} = 0.18333$$

Solid Fraction of Control Volume: $\phi_s := 1 - \phi_{fh} - \phi_{fc}$ $\qquad \phi_s = 0.53889$

Total MS flow cross section area: $Ac_c(\mathrm{height}_c, Ac_c) := A\_face_c\cdot\phi_{fc}$ $\qquad Ac_c(\mathrm{height}_c, Ac_c) = 0.91667\,\mathrm{m}^2$

total number of flow channels leading into the OSF section:

$$\frac{Ac_c(\mathrm{height}_c, Ac_c)}{ac_c(\mathrm{height}_c)} = 2.77778 \times 10^4$$

$$n_{front.c} := \frac{Ac_c(\mathrm{height}_c, Ac_c)}{ac_c(\mathrm{height}_c)}$$

This divides the total effective or flow area on the HX face by the effective or flow area for unit cell D

$n_{front.c} = 2.77778 \times 10^{4}$

$n_{stack} = 250.00000$ The number of composite MS & He plates in the stack $A\_face_c = 5.00000\,m^{2}$

$$height_{comp\_p} := \left(\frac{height_c}{2} + \frac{height_h}{2} + t_{wall}\right) \qquad height_{comp\_p} = 6.00000 \times 10^{-3}\,m$$

MS average Darcy (advection term) velociy:

$$u_{darcy\_c}(Ac_{MS}) := \frac{Q_c}{A\_face_c} \qquad u_{darcy\_c}(Ac_h) = 5.56627 \times 10^{-3}\,\frac{m}{s}$$

MS average interstitial velocity:

$$u_c(height_h, Ac_h) := \frac{Q_c}{Ac_c(height_h, Ac_h)} \qquad u_c(height_h, Ac_h) = 0.03036\,\frac{m}{s}$$

$$Re_c(height_h, Ac_h) := u_c(height_h, Ac_h)\cdot\frac{D_c}{\nu_{MS}} \qquad Re_c(height_h, Ac_h) = 51.75252$$

Heat transfer equation by Manglik&Bergles:

$$\alpha_c := \frac{P_{xc} - t_c}{height_c} \qquad \alpha_c = 3.66667$$

$$\delta_c := \frac{C_{fin}\cdot t_c}{P_{yc}} \qquad \delta_c = 0.08333$$

$$\gamma_c := \frac{C_{fin}\cdot t_c}{P_{xc} - t_c} \qquad \gamma_c = 0.18182$$

$$j_c(height_h, Ac_h) := \left|\begin{array}{l} A \leftarrow 0.6522\cdot Re_c(height_h, Ac_h)^{-0.5403}\,\alpha_c^{-0.1541}\,\delta_c^{0.1499}\,\gamma_c^{-0.0678} \\ B \leftarrow \left(1 + 5.269\cdot 10^{-5}\cdot Re_c(height_h, Ac_h)^{1.340}\cdot\alpha_c^{0.504}\cdot\delta_c^{0.456}\,\gamma_c^{-1.055}\right)^{0.1} \\ A\cdot B \end{array}\right. \qquad j_c(height_h, Ac_h) = 0.04915$$

$$f_c(height_h, Ac_h) := \left|\begin{array}{l} A \leftarrow 9.6243\cdot Re_c(height_h, Ac_h)^{-0.7422}\,\alpha_c^{-0.1856}\,\delta_c^{0.3053}\,\gamma_c^{-0.2659} \\ B \leftarrow \left(1 + 7.669\cdot 10^{-8}\cdot Re_c(height_h, Ac_h)^{4.429}\cdot\alpha_c^{0.920}\cdot\delta_c^{3.767}\,\gamma_c^{0.236}\right)^{0.1} \\ A\cdot B \end{array}\right. \qquad f_c(height_h, Ac_h) = 0.29783$$

flow area goodness factor: $goodness_c(height_h, Ac_h) := \frac{j_c(height_h, Ac_h)}{f_c(height_h, Ac_h)}$ $goodness_c(height_h, Ac_h) = 0.16501$

Heat transfer correlation for off-set strip fin channels:

$$Nu_c(height_h, Ac_h) := j_c(height_h, Ac_h)\cdot Re_c(height_h, Ac_h)\cdot Pr_{MS}^{\frac{1}{3}} \qquad Nu_c(height_h, Ac_h) = 5.80400$$

Heat transfer correlation for smooth channels (turbulent flow):

$$Nu_{c0}(height_h, Ac_h) := 0.023 \cdot Re_c(height_h, Ac_h)^{0.8} \cdot Pr_{MS}^{0.33} \qquad Nu_{c0}(height_h, Ac_h) = 1.22350$$

Heat transfer augumentation by offset arrangement:

$$E_c(height_h, Ac_h) := \frac{Nu_c(height_h, Ac_h)}{Nu_{c0}(height_h, Ac_h)} \qquad E_c(height_h, Ac_h) = 4.74376$$

Heat transfer coefficient for MS:

$$h_c(height_h, Ac_h) := Nu_c(height_h, Ac_h) \cdot \frac{k_{MS}}{D_c} \qquad h_c(height_h, Ac_h) = 1.24040 \times 10^3 \frac{kg}{K \cdot s^3}$$

fin efficiency:

$$mh_c(height_h, Ac_h) := \sqrt{2 \cdot \frac{h_c(height_h, Ac_h)}{k_{LSI} \cdot t_c}} \cdot \frac{height_c}{2} \qquad mh_c(height_h, Ac_h) = 0.26414$$

$$\eta_{finc}(height_h, Ac_h) := \frac{\tanh(mh_c(height_h, Ac_h))}{mh_c(height_h, Ac_h)} \qquad \eta_{finc}(height_h, Ac_h) = 0.97737$$

overall surface efficiency:

$$\eta_{c0}(height_h, Ac_h) := \frac{aw_{wall} + \eta_{finc}(height_h, Ac_h) \cdot aw_{finc}}{aw_c} \qquad \eta_{c0}(height_h, Ac_h) = 0.99509$$

Overall thermal calculation:

LMTD of HX: $\Delta T_m = 44.43225\,K$

$mfr_{He} = 26.16398 \frac{kg}{s}$ $\qquad mfr_{MS} = 51.48800 \frac{kg}{s}$

$Power_{ihx} = 5.00000 \times 10^7\,W$

Overall heat transfer coefficient: $UA := \frac{Power_{ihx}}{\Delta T_m}$ $\qquad UA = 1.12531 \times 10^6 \frac{m^2 \cdot kg}{K \cdot s^3}$

cold fluid heat capacity rate: $C_c := mfr_{MS} \cdot c_{pMS}$ $\qquad C_c = 1.20482 \times 10^5 \frac{m^2 \cdot kg}{K \cdot s^3}$

hot fluid heat capacity rate: $C_h := mfr_{He} \cdot c_{pHe}$ $\qquad C_h = 1.35870 \times 10^5 \frac{m^2 \cdot kg}{K \cdot s^3}$

$C_{min} := \min(C_c, C_h)$ $\qquad C_{min} = 1.20482 \times 10^5 \frac{m^2 \cdot kg}{K \cdot s^3}$

$NTU := \frac{UA}{C_{min}}$ $\qquad NTU = 9.34006$

the HX effectiveness: $\varepsilon_{ihx} = 0.94318$

ratio of total hot side heat transfer surface to the hot side base wall heat transfer surface:

$$r_{He2wall}(height_h) := \frac{aw_h(height_h)}{aw_{wall}} \qquad r_{He2wall}(height_h) = 1.48077$$

ratio of total salt side heat transfer surface to the salt side base wall heat transfer surface:

$$r_{MS2wall} := \frac{aw_c}{aw_{wall}} \qquad r_{MS2wall} = 1.27692$$

heat resistances per unit base wall area:

$$R_h(height_h, Ac_h) := \frac{1}{h_h(height_h, Ac_h)\cdot\eta_{h0}(height_h, Ac_h)\cdot r_{He2wall}(height_h)} \qquad R_h(height_h, Ac_h) = 6.82729 \times 10^{-4}\,\frac{K\cdot s^3}{kg}$$

$$R_{wall} := \frac{t_{wall}}{k_{LSI}} \qquad R_{wall} = 1.00000 \times 10^{-4}\,\frac{K\cdot s^3}{kg}$$

$$R_c(height_h, Ac_h) := \frac{1}{h_c(height_h, Ac_h)\cdot\eta_{c0}(height_h, Ac_h)\cdot r_{MS2wall}} \qquad R_c(height_h, Ac_h) = 6.34469 \times 10^{-4}\,\frac{K\cdot s^3}{kg}$$

Total one side base wall surface:

$$A_w(height_h, Ac_h) := UA\cdot\left(R_h(height_h, Ac_h) + R_{wall} + R_c(height_h, Ac_h)\right) \qquad A_w(height_h, Ac_h) = 1.59479 \times 10^3\,m^2$$

Total heat transfer area for the hot side:

$$A_h(height_h, Ac_h) := A_w(height_h, Ac_h)\cdot r_{He2wall}(height_h) \qquad A_h(height_h, Ac_h) = 2.36151 \times 10^3\,m^2$$

Total heat transfer area for the cold side:

$$A_c(height_h, Ac_h) := A_w(height_h, Ac_h)\cdot r_{MS2wall} \qquad A_c(height_h, Ac_h) = 2.03642 \times 10^3\,m^2$$

Total number of HX cells: $n_c(height_h, Ac_h) := \dfrac{A_w(height_h, Ac_h)}{aw_{wall}}$ $\qquad n_c(height_h, Ac_h) = 1.53345 \times 10^6$

The number of cells in the flow direction:

$$n_{length}(height_h, Ac_h) := \frac{n_c(height_h, Ac_h)}{n_{front.c}} \qquad n_{length}(height_h, Ac_h) = 55.20410$$

The length of flow channel:

$$length_{path}(height_h, Ac_h) := n_{length}(height_h, Ac_h)\cdot 2\cdot P_{yh} \qquad length_{path}(height_h, Ac_h) = 2.64980\,m$$

The total cross area for a unit cell (include the wall and fins):

$$a_{cell}(height_h) := P_{xh}\cdot(height_h + height_c + 2\cdot t_{wall}) \qquad a_{cell}(height_h) = 1.80000 \times 10^{-4}\,m^2$$

The total frontal cross area for the HX:

$$A_{total}(height_h, Ac_h) := n_{front.h}\cdot a_{cell}(height_h) \qquad A_{total}(height_h, Ac_h) = 5.00000\,m^2$$

The total volume for the HX:

$$V_{ht}(height_h, Ac_h) := A_{total}(height_h, Ac_h)\cdot length_{path}(height_h, Ac_h) \qquad V_{ht}(height_h, Ac_h) = 1.32490 \times 10^{4}\,L$$

The total mass for the HX:

the material volume of a cell:

$$v_{LSI\_cell}(height_h) := 2\cdot t_c\cdot l_c\cdot height_c + 2\cdot P_{xc}\cdot 2\cdot P_{yc}\cdot t_{wall} + 2t_h\cdot l_h\cdot height_h \qquad v_{LSI\_cell}(height_h) = 4.36000 \times 10^{-3}\,L$$

the material mass of a cell (exclude fluids):

$$m_{cell}(height_h) := \rho_{LSI}\, v_{LSI\_cell}(height_h) \qquad m_{cell}(height_h) = 8.72000 \times 10^{-3}\,kg$$

the total material mass of the HX:

$$m_{ht}(height_h, Ac_h) := m_{cell}(height_h)\cdot n_c(height_h, Ac_h) \qquad m_{ht}(height_h, Ac_h) = 1.33717 \times 10^{4}\,kg$$

Compactness of the HX:

$$compactness(height_h, Ac_h) := \frac{A_h(height_h, Ac_h)}{V_{ht}(height_h, Ac_h)} \qquad compactness(height_h, Ac_h) = 178.24074\,\frac{1}{m}$$

4. Pressure loss calculation:

Cold side:

assume smooth channel, for cold side: $\mathrm{Re_c}(\mathrm{height_h}, \mathrm{Ac_h}) = 51.75252$

$$\mathrm{f_{c0}}(\mathrm{height_h}, \mathrm{Ac_h}) := \begin{cases} \frac{64}{4} \cdot \mathrm{Re_c}(\mathrm{height_h}, \mathrm{Ac_h})^{-1} & \text{if } \mathrm{Re_c}(\mathrm{height_h}, \mathrm{Ac_h}) \le 2000 \\ \frac{\mathrm{Re_c}(\mathrm{height_h}, \mathrm{Ac_h})^{0.33}}{381 \cdot 4} & \text{if } \mathrm{Re_c}(\mathrm{height_h}, \mathrm{Ac_h}) > 2000 \wedge \mathrm{Re_c}(\mathrm{height_h}, \mathrm{Ac_h}) \le 4000 \\ \frac{0.316}{4} \mathrm{Re_c}(\mathrm{height_h}, \mathrm{Ac_h})^{-0.25} & \text{if } \mathrm{Re_c}(\mathrm{height_h}, \mathrm{Ac_h}) > 4000 \wedge \mathrm{Re_c}(\mathrm{height_h}, \mathrm{Ac_h}) \le 30000 \\ \frac{0.184}{4} \cdot \mathrm{Re_c}(\mathrm{height_h}, \mathrm{Ac_h})^{-0.2} & \text{otherwise} \end{cases}$$

$\mathrm{f_{c0}}(\mathrm{height_h}, \mathrm{Ac_h}) = 0.30916$

Actual friction increase: $\mathrm{F_c}(\mathrm{height_h}, \mathrm{Ac_h}) := \frac{\mathrm{f_c}(\mathrm{height_h}, \mathrm{Ac_h})}{\mathrm{f_{c0}}(\mathrm{height_h}, \mathrm{Ac_h})}$ $\mathrm{F_c}(\mathrm{height_h}, \mathrm{Ac_h}) = 0.96335$

Pressure drop:

smooth channel:

$$\Delta \mathrm{p_{c0}}(\mathrm{height_h}, \mathrm{Ac_h}) := 4 \cdot \mathrm{f_{c0}}(\mathrm{height_h}, \mathrm{Ac_h}) \cdot \frac{\mathrm{length_{path}}(\mathrm{height_h}, \mathrm{Ac_h}) \cdot \rho_{MS} \cdot \mathrm{u_c}(\mathrm{height_h}, \mathrm{Ac_h})^2}{D_c \cdot 2}$$

$\Delta \mathrm{p_{c0}}(\mathrm{height_h}, \mathrm{Ac_h}) = 585.43945\,\mathrm{Pa}$

Offset strip fin channel:

$$\Delta \mathrm{p_c}(\mathrm{height_h}, \mathrm{Ac_h}) := 4 \cdot \mathrm{f_c}(\mathrm{height_h}, \mathrm{Ac_h}) \cdot \frac{\mathrm{length_{path}}(\mathrm{height_h}, \mathrm{Ac_h}) \cdot \rho_{MS} \cdot \mathrm{u_c}(\mathrm{height_h}, \mathrm{Ac_h})^2}{D_c \cdot 2}$$

$\Delta \mathrm{p_c}(\mathrm{height_h}, \mathrm{Ac_h}) = 563.98428\,\mathrm{Pa}$

pumping power needed for the cold side:

$\eta_p := 0.85$

puming power: $\mathrm{P_{pump\_c}}(\mathrm{height_h}, \mathrm{Ac_h}) := \frac{Q_c \cdot \Delta \mathrm{p_c}(\mathrm{height_h}, \mathrm{Ac_h})}{\eta_p}$ $\mathrm{P_{pump\_c}}(\mathrm{height_h}, \mathrm{Ac_h}) = 18.46641\,\mathrm{W}$

Hot side:

$\mathrm{Re_h}(\mathrm{height_h}, \mathrm{Ac_h}) = 2.59089 \times 10^3$

assume smooth channel,

$$f_{h0}(\mathrm{height}_h, Ac_h) := \begin{cases} \frac{64}{4}\cdot Re_h(\mathrm{height}_h, Ac_h)^{-1} & \text{if } Re_h(\mathrm{height}_h, Ac_h) \le 2000 \\ \frac{Re_h(\mathrm{height}_h, Ac_h)^{0.33}}{381\cdot 4} & \text{if } Re_h(\mathrm{height}_h, Ac_h) > 2000 \wedge Re_h(\mathrm{height}_h, Ac_h) \le 4000 \\ \frac{0.316}{4} Re_h(\mathrm{height}_h, Ac_h)^{-0.25} & \text{if } Re_h(\mathrm{height}_h, Ac_h) > 4000 \wedge Re_h(\mathrm{height}_h, Ac_h) \le 30000 \\ \frac{0.184}{4}\cdot Re_h(\mathrm{height}_h, Ac_h)^{-0.2} & \text{otherwise} \end{cases}$$

$$f_{h0}(\mathrm{height}_h, Ac_h) = 8.77916 \times 10^{-3}$$

Actual friction increase: $F_h(\mathrm{height}_h, Ac_h) := \frac{f_h(\mathrm{height}_h, Ac_h)}{f_{h0}(\mathrm{height}_h, Ac_h)}$ $F_h(\mathrm{height}_h, Ac_h) = 5.68251$

Pressure drop:

Offset strip fin channel:

$$\Delta p_h(\mathrm{height}_h, Ac_h) := 4\cdot f_h(\mathrm{height}_h, Ac_h)\cdot\frac{\mathrm{length}_{path}(\mathrm{height}_h, Ac_h)\cdot\rho_{He}\left(P_h, \frac{T_{1i}+T_{1o}}{2}\right)\cdot u_h(Ac_h)^2}{D_h(\mathrm{height}_h)\cdot 2}$$

$$\Delta p_h(\mathrm{height}_h, Ac_h) = 4.50779 \times 10^{3}\ \mathrm{Pa}$$

Ratio to the system pressure: $\frac{\Delta p_h(\mathrm{height}_h, Ac_h)}{P_0} = 6.33117 \times 10^{-4}$

pumping power needed for the HX helium side: $\eta_p := 0.85$

puming power: $P_{pump\_h}(\mathrm{height}_h, Ac_h) := \frac{Q_h\cdot\Delta p_h(\mathrm{height}_h, Ac_h)}{\eta_p}$ $P_{pump\_h}(\mathrm{height}_h, Ac_h) = 4.50212 \times 10^{4}\ \mathrm{W}$

total pumping power:

$P_{pump}(\mathrm{height}_h, Ac_h) := P_{pump\_h}(\mathrm{height}_h, Ac_h) + P_{pump\_c}(\mathrm{height}_h, Ac_h)$ $P_{pump}(\mathrm{height}_h, Ac_h) = 4.50397 \times 10^{4}\ \mathrm{W}$

5. Summary for the heaters thermal design:

The highest pressure in helium side: $P_0 = 7.12000 \times 10^6 \,\mathrm{Pa}$

Helium channel height: $\mathrm{height_h} = 5.00000 \times 10^{-3} \,\mathrm{m}$

Total frontal area of the helium channels: $\mathrm{Ac_h} = 1.38889 \,\mathrm{m}^2$

Helium velocity: $u_h(\mathrm{Ac_h}) = 6.11230 \,\frac{\mathrm{m}}{\mathrm{s}}$

Power: $\mathrm{Power_{ihx}} = 5.00000 \times 10^7 \,\mathrm{W}$

Helium side pressure: $P_h = 7.06000 \times 10^6 \,\mathrm{Pa}$

Hot side inlet temperature: $T_{1i} = 1.27315 \times 10^3 \,\mathrm{K}$

Hot side outlet temperature: $T_{1o} = 905.15000 \,\mathrm{K}$

Cold side inlet temperature: $T_{2i} = 833.15000 \,\mathrm{K}$

Cold side outlet temperature: $T_{2o} = 1.24815 \times 10^3 \,\mathrm{K}$

LMTD : $\Delta T_m = 44.43225 \,\mathrm{K}$

Base hot side Ac parameters: $\mathrm{Ac_{h0}} := 0.5\mathrm{m}^2$

Salt side velocity: $u_c(\mathrm{height_h}, \mathrm{Ac_{h0}}) = 0.03036 \,\frac{\mathrm{m}}{\mathrm{s}}$

volumetric flow rate:

Salt : $Q_c = 0.02783 \,\frac{\mathrm{m}^3}{\mathrm{s}}$ Helium : $Q_h = 8.48930 \,\frac{\mathrm{m}^3}{\mathrm{s}}$

mass flow rate:

Salt : $\mathrm{mfr_{MS}} = 51.48800 \,\frac{\mathrm{kg}}{\mathrm{s}}$ Helium : $\mathrm{mfr_{He}} = 26.16398 \,\frac{\mathrm{kg}}{\mathrm{s}}$

total heat exchanger volume: $V_{ht}(\mathrm{height_h}, \mathrm{Ac_{h0}}) = 1.04339 \times 10^4 \,\mathrm{L}$

flow channel length: $\mathrm{length_{path}}(\mathrm{height_h}, \mathrm{Ac_{h0}}) = 2.08677 \,\mathrm{m}$

frontal area: $A_{total}(\mathrm{height_h}, \mathrm{Ac_{h0}}) = 5.00000 \,\mathrm{m}^2$

$\mathrm{width_{HX}} := \max(\mathrm{width_{MS\_p}}, \mathrm{width_{He\_p}})$

$\mathrm{width}_{HX} := \mathrm{width}_{comp\_p}$

$\mathrm{width}_{HX} = 3.33333\,\mathrm{m}$

$\mathrm{height}_{HX} := \mathrm{height}_{comp\_p}$ $\mathrm{height}_{HX} = 6.00000 \times 10^{-3}\,\mathrm{m}$

Hot side pressure loss: $\Delta p_h\left(\mathrm{height}_h, Ac_{h0}\right) = 2.01754 \times 10^4\,\mathrm{Pa}$

Cold side pressure loss: $\Delta p_c\left(\mathrm{height}_h, Ac_{h0}\right) = 444.15032\,\mathrm{Pa}$

Total helium side pressure loss: $\Delta p_h\left(\mathrm{height}_h, Ac_{h0}\right) = 2.01754 \times 10^4\,\mathrm{Pa}$ $\dfrac{\Delta p_h\left(\mathrm{height}_h, Ac_{h0}\right)}{P_0} = 2.83362 \times 10^{-3}$

total HX weight: $m_{ht}\left(\mathrm{height}_h, Ac_{h0}\right) = 1.05305 \times 10^4\,\mathrm{kg}$

hot side pumping power: $P_{pump\_h}\left(\mathrm{height}_h, Ac_{h0}\right) = 2.01500 \times 10^5\,\mathrm{W}$

cold side relative pumping power: $P_{pump\_c}\left(\mathrm{height}_h, Ac_{h0}\right) = 14.54271\,\mathrm{W}$

hot side convective heat transfer coefficient: $h_h\left(\mathrm{height}_h, Ac_{h0}\right) = 1.81035 \times 10^3\,\dfrac{\mathrm{kg}}{\mathrm{K}\cdot\mathrm{s}^3}$

cold side convective heat transfer coefficient: $h_c\left(\mathrm{height}_h, Ac_{h0}\right) = 1.24040 \times 10^3\,\dfrac{\mathrm{kg}}{\mathrm{K}\cdot\mathrm{s}^3}$

Hot channel heat tranfer augmentation: $E_h\left(\mathrm{height}_h, Ac_{h0}\right) = 1.29440$

Hot channel friction increase: $F_h\left(\mathrm{height}_h, Ac_{h0}\right) = 4.28403$

Cold side channel heat transfer augmentation: $E_c\left(\mathrm{height}_h, Ac_{h0}\right) = 4.74376$

Cold channel friction increase: $F_c\left(\mathrm{height}_h, Ac_{h0}\right) = 0.96335$

flow area goodness factor for hot side channel: $\mathrm{goodness}_h\left(\mathrm{height}_h, Ac_{h0}\right) = 0.13733$

flow area goodness factor for cold side channel: $\mathrm{goodness}_c\left(\mathrm{height}_h, Ac_{h0}\right) = 0.16501$

Heat exchanger compactness (overall average):
London gave 656 m^2/m^3 as compact HX lower value $\mathrm{compactness}\left(\mathrm{height}_h, Ac_{h0}\right) = 178.24074\,\dfrac{1}{\mathrm{m}}$

Thermal density: $\dfrac{\mathrm{Power}_{ihx}}{V_{ht}\left(\mathrm{height}_h, Ac_{h0}\right)} = 4.79208 \times 10^6\,\dfrac{\mathrm{W}}{\mathrm{m}^3}$

Appendix B

Table of thermo-physical properties for high-pressure helium

Temperature (K)	Pressure (MPa)	Density (kg/m3)	Cp (J/g*K)	Viscosity (Pa*s)	Therm. Cond. (W/m*K)	Phase
800	7	4.1691	5.1889	3.95E-05	0.31208	Supercritical
850	7	3.9267	5.1892	4.12E-05	0.32539	Supercritical
900	7	3.7108	5.1894	4.29E-05	0.33847	Supercritical
950	7	3.5174	5.1896	4.46E-05	0.35135	Supercritical
1000	7	3.3432	5.1897	4.62E-05	0.36402	Supercritical
1050	7	3.1854	5.1899	4.79E-05	0.37651	Supercritical
1100	7	3.0418	5.1901	4.94E-05	0.38883	Supercritical
1150	7	2.9106	5.1902	5.10E-05	0.40098	Supercritical
1200	7	2.7902	5.1903	5.26E-05	0.41298	Supercritical
1250	7	2.6794	5.1905	5.41E-05	0.42484	Supercritical
1300	7	2.577	5.1906	5.57E-05	0.43655	Supercritical

Source: http://webbook.nist.gov/

Appendix C

One-dimensional steady-state temperature distribution using the effectiveness-NTU method

Eugenio Urquiza

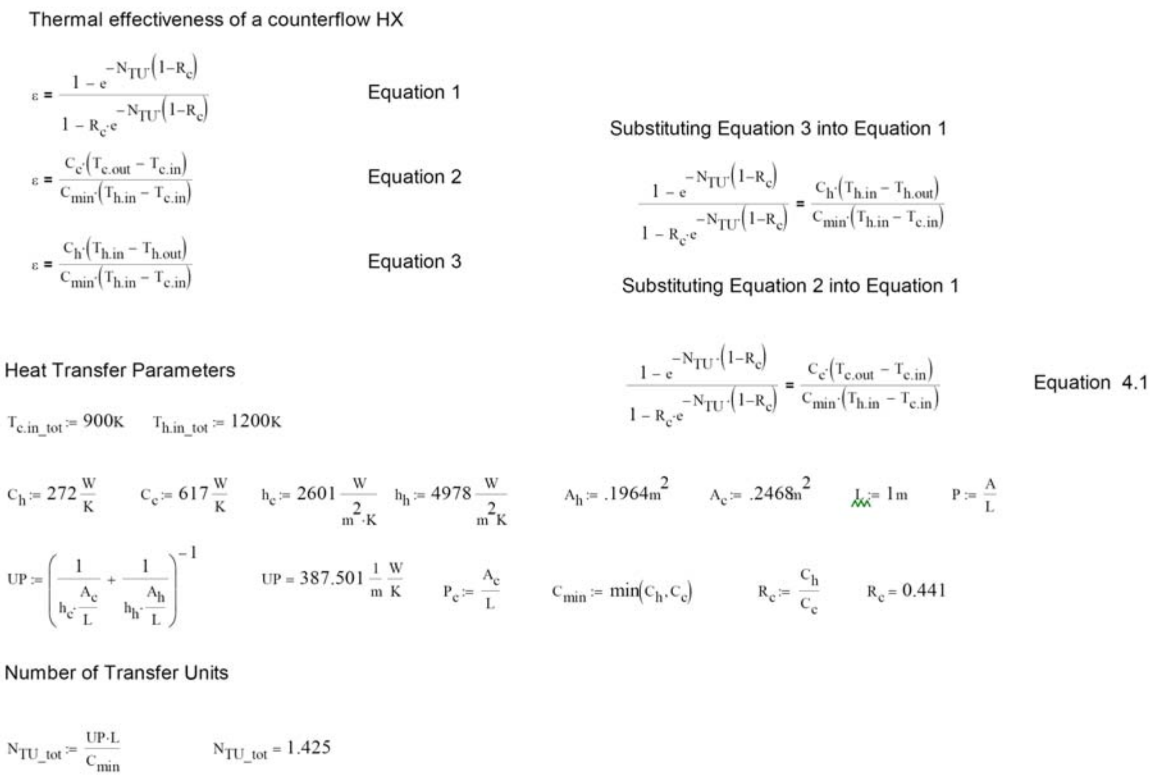

Thermal effectiveness of a counterflow HX

$$\varepsilon = \frac{1 - e^{-N_{TU}\cdot(1-R_c)}}{1 - R_c\cdot e^{-N_{TU}\cdot(1-R_c)}}$$ Equation 1

$$\varepsilon = \frac{C_c\cdot(T_{c.out} - T_{c.in})}{C_{min}\cdot(T_{h.in} - T_{c.in})}$$ Equation 2

$$\varepsilon = \frac{C_h\cdot(T_{h.in} - T_{h.out})}{C_{min}\cdot(T_{h.in} - T_{c.in})}$$ Equation 3

Substituting Equation 3 into Equation 1

$$\frac{1 - e^{-N_{TU}\cdot(1-R_c)}}{1 - R_c\cdot e^{-N_{TU}\cdot(1-R_c)}} = \frac{C_h\cdot(T_{h.in} - T_{h.out})}{C_{min}\cdot(T_{h.in} - T_{c.in})}$$

Substituting Equation 2 into Equation 1

$$\frac{1 - e^{-N_{TU}\cdot(1-R_c)}}{1 - R_c\cdot e^{-N_{TU}\cdot(1-R_c)}} = \frac{C_c\cdot(T_{c.out} - T_{c.in})}{C_{min}\cdot(T_{h.in} - T_{c.in})}$$ Equation 4.1

Heat Transfer Parameters

$T_{c.in\_tot} := 900\text{K}$ $T_{h.in\_tot} := 1200\text{K}$

$C_h := 272\,\frac{W}{K}$ $C_c := 617\,\frac{W}{K}$ $h_c := 2601\,\frac{W}{m^2\cdot K}$ $h_h := 4978\,\frac{W}{m^2 K}$ $A_h := .1964m^2$ $A_c := .2468m^2$ $L := 1m$ $P := \frac{A}{L}$

$UP := \left(\frac{1}{h_c\cdot\frac{A_c}{L}} + \frac{1}{h_h\cdot\frac{A_h}{L}}\right)^{-1}$ $UP = 387.501\,\frac{1}{m}\,\frac{W}{K}$ $P_c := \frac{A_c}{L}$ $C_{min} := \min(C_h, C_c)$ $R_c := \frac{C_h}{C_c}$ $R_c = 0.441$

Number of Transfer Units

$N_{TU\_tot} := \frac{UP\cdot L}{C_{min}}$ $N_{TU\_tot} = 1.425$

Solving for T.c.out from Equation 4.1 yields:

$$T_{c.out\_tot} := \frac{(-C_{min})\cdot T_{h.in\_tot} + C_{min}\cdot T_{c.in\_tot} + C_{min}\cdot e^{N_{TU\_tot}\cdot(R_c-1)}\cdot T_{h.in\_tot} - C_{min}\cdot e^{N_{TU\_tot}\cdot(R_c-1)}\cdot T_{c.in\_tot} - C_c\cdot T_{c.in\_tot} + C_c\cdot T_{c.in\_tot}\cdot R_c\cdot e^{N_{TU\_tot}\cdot(R_c-1)}}{C_c\cdot\left[(-1) + R_c\cdot e^{N_{TU\_tot}\cdot(R_c-1)}\right]}$$

Equation 4.2

$T_{c.out\_tot} = 990.641\,K$

The number of Transfer Units expressed for the Hot Fluid (Flowing in the positive x direction)

$C_{min} = 272\,\frac{W}{K}$

The number of Transfer Units expressed for the Cold Fluid (Flowing in the negative x direction)

$N_{TU}(x) := \frac{UP\cdot x}{C_{min}}$ Equation 5

$N_{TU2}(x) := \frac{UP\cdot(L-x)}{C_{min}}$

Equation 4.3

$$T_{c.in}(x) := \frac{(-C_{min})\cdot T_{h.in\_tot} + C_{min}\cdot e^{N_{TU}(x)\cdot(R_c-1)}\cdot T_{h.in\_tot} + C_c\cdot T_{c.out\_tot} - C_c\cdot T_{c.out\_tot}\cdot R_c\cdot e^{N_{TU}(x)\cdot(R_c-1)}}{(-C_{min}) + C_{min}\cdot e^{N_{TU}(x)\cdot(R_c-1)} + C_c - C_c\cdot R_c\cdot e^{N_{TU}(x)\cdot(R_c-1)}}$$

Substituting Equation 3 into Equation 1

$$\frac{1 - e^{-N_{TU}\cdot(1-R_c)}}{1 - R_c\cdot e^{-N_{TU}\cdot(1-R_c)}} = \frac{C_h\cdot(T_{h.in} - T_{h.out})}{C_{min}\cdot(T_{h.in} - T_{c.in})}$$

Equation 6.1

Solving for T.h.out from Equation 6.1 yields:

$$T_{h.out\_tot} := \frac{C_{min}\cdot T_{h.in\_tot} - C_{min}\cdot T_{c.in\_tot} - C_{min}\cdot e^{N_{TU\_tot}\cdot(R_c-1)}\cdot T_{h.in\_tot} + C_{min}\cdot e^{N_{TU\_tot}\cdot(R_c-1)}\cdot T_{c.in\_tot} - C_h\cdot T_{h.in\_tot} + C_h\cdot T_{h.in\_tot}\cdot R_c\cdot e^{N_{TU\_tot}\cdot(R_c-1)}}{C_h\cdot\left[R_c\cdot e^{N_{TU\_tot}\cdot(R_c-1)} - 1\right]}$$

Equation 6.2

$T_{h.out\_tot} = 994.392\,K$

Solving Equation 6.1 for T.h.in gives:

$$T_{h.in}(x) := \frac{-\left[C_{min}\cdot T_{c.in\_tot} - C_{min}\cdot e^{N_{TU2}(x)\cdot[(-1)+R_c]}\cdot T_{c.in\_tot} - C_h\cdot T_{h.out\_tot} + C_h\cdot T_{h.out\_tot}\cdot R_c\cdot e^{N_{TU2}(x)\cdot[(-1)+R_c]}\right]}{(-C_{min}) + C_{min}\cdot e^{N_{TU2}(x)\cdot[(-1)+R_c]} + C_h - C_h\cdot R_c\cdot e^{N_{TU2}(x)\cdot[(-1)+R_c]}}$$

Equation 7

$$T_s(x) := \frac{h_h\cdot A_h\cdot T_{h.in}(x) + h_c\cdot A_c\cdot T_{c.in}(x)}{h_h\cdot A_h + h_c\cdot A_c}$$

Equation 8

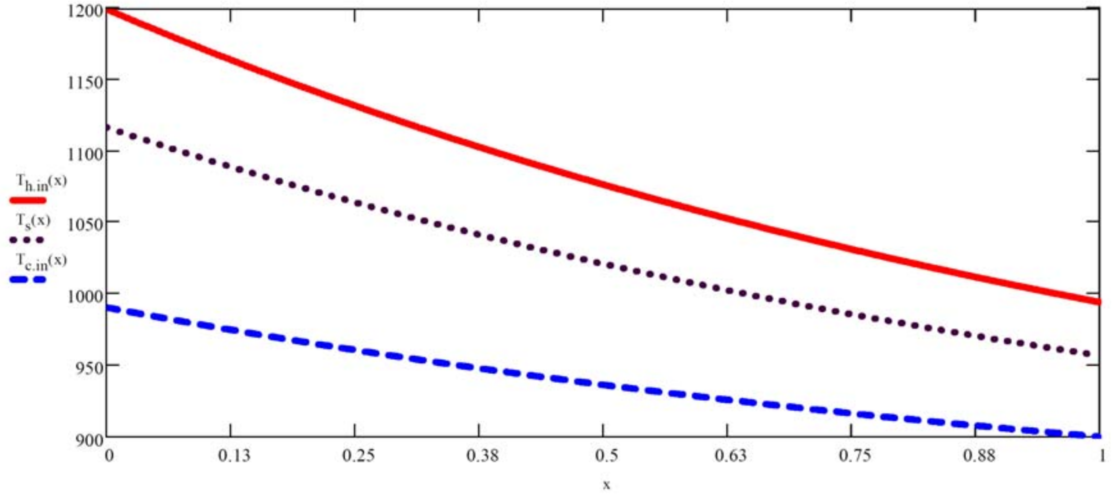

Appendix D

Effective Mechanical Properties

Kenneth Lee

Appendix D.1: Orthotropicity

The solid mechanics equations, including the relation between stress and strain, are derived from the Cauchy approximation that atoms in a material behave like springs in accordance to Hooke's Law: $F = ku$. The solid mechanics equivalent of Hooke's Law is $\sigma = \mathrm{E}\varepsilon$. The inverse is written in matrix notation as

$$\begin{Bmatrix} \varepsilon_{xx} \\ \varepsilon_{yy} \\ \varepsilon_{zz} \\ \varepsilon_{xy} \\ \varepsilon_{yz} \\ \varepsilon_{xz} \end{Bmatrix} = \begin{bmatrix} C_{11} & C_{12} & C_{13} & C_{14} & C_{15} & C_{16} \\ C_{21} & C_{22} & C_{23} & C_{24} & C_{25} & C_{26} \\ C_{31} & C_{32} & C_{33} & C_{34} & C_{35} & C_{36} \\ C_{41} & C_{42} & C_{43} & C_{44} & C_{45} & C_{46} \\ C_{51} & C_{52} & C_{53} & C_{54} & C_{55} & C_{56} \\ C_{61} & C_{62} & C_{63} & C_{64} & C_{65} & C_{66} \end{bmatrix} \begin{Bmatrix} \sigma_{xx} \\ \sigma_{yy} \\ \sigma_{zz} \\ \sigma_{xy} \\ \sigma_{yz} \\ \sigma_{xz} \end{Bmatrix}$$

where σ is stress, C_{ij} is the material constant in the compliance matrix, and ε is the strain.

The matrix notation above is the most generalized form of Hooke's Law, encompassing any imaginable elastic material. The stiffness matrix has 36 different elastic constants, meaning the material behaves differently in each direction.

However, most elastic engineering material are orthotropic, meaning there are at least two orthogonal planes of symmetry. A plane of symmetry in solid mechanics denotes a plan in which the material constant is the same whether the material is compressed and tensioned normal to the plane. When a material is orthotropic, the 36 elastic constants simplify to nine independent moduli: 3 elastic moduli (*E*), 3 Poisson's ratios (*v*), and 3 shear moduli (*G*). Hooke's Law for orthotropic materials is as follows

$$\begin{Bmatrix} \varepsilon_{xx} \\ \varepsilon_{yy} \\ \varepsilon_{zz} \\ \varepsilon_{xy} \\ \varepsilon_{yz} \\ \varepsilon_{xz} \end{Bmatrix} = \begin{bmatrix} \frac{1}{E_x} & -\frac{\nu_{xy}}{E_x} & -\frac{\nu_{xz}}{E_x} & 0 & 0 & 0 \\ -\frac{\nu_{yx}}{E_y} & \frac{1}{E_y} & -\frac{\nu_{yz}}{E_y} & 0 & 0 & 0 \\ -\frac{\nu_{zx}}{E_z} & -\frac{\nu_{zy}}{E_z} & \frac{1}{E_z} & 0 & 0 & 0 \\ 0 & 0 & 0 & \frac{1}{2G_{xy}} & 0 & 0 \\ 0 & 0 & 0 & 0 & \frac{1}{2G_{yz}} & 0 \\ 0 & 0 & 0 & 0 & 0 & \frac{1}{2G_{xz}} \end{bmatrix} \begin{Bmatrix} \sigma_{xx} \\ \sigma_{yy} \\ \sigma_{zz} \\ \sigma_{xy} \\ \sigma_{yz} \\ \sigma_{xz} \end{Bmatrix}$$

where $\frac{\nu_{xy}}{E_x} = \frac{\nu_{yx}}{E_y}$, $\frac{\nu_{yz}}{E_y} = \frac{\nu_{zy}}{E_z}$, and $\frac{\nu_{xz}}{E_x} = \frac{\nu_{zx}}{E_z}$.

Also, $G_{xy} = G_{yx}$, $G_{yz} = G_{yz}$, and $G_{xz} = G_{zx}$

Appendix D.2: Solving "Effective Normal Moduli"

Appendix D.2.1: Using a Two-Test Method

From Hooke's Law in Appendix A, the normal moduli are defined by nine different variables (three Young's Moduli and six Poisson's Ratios) in three equations:

$$\begin{Bmatrix} \varepsilon_{xx} \\ \varepsilon_{yy} \\ \varepsilon_{zz} \end{Bmatrix} = \begin{bmatrix} {}^{1}\!/_{E_x} & {}^{-\nu_{xy}}\!/_{E_x} & {}^{-\nu_{xz}}\!/_{E_x} \\ {}^{-\nu_{yx}}\!/_{E_y} & {}^{1}\!/_{E_y} & {}^{-\nu_{yz}}\!/_{E_y} \\ {}^{-\nu_{zx}}\!/_{E_z} & {}^{-\nu_{zy}}\!/_{E_z} & {}^{1}\!/_{E_z} \end{bmatrix} \begin{Bmatrix} \sigma_{xx} \\ \sigma_{yy} \\ \sigma_{zz} \end{Bmatrix}.$$

or

$$\begin{Bmatrix} \varepsilon_{xx} \\ \varepsilon_{yy} \\ \varepsilon_{zz} \end{Bmatrix} = \begin{bmatrix} i_{11} & i_{12} & i_{13} \\ i_{21} & i_{22} & i_{23} \\ i_{31} & i_{32} & i_{33} \end{bmatrix} \begin{Bmatrix} \sigma_{xx} \\ \sigma_{yy} \\ \sigma_{zz} \end{Bmatrix}$$

The 9x9 matrix above is the compliance matrix. Due to the orthotropic constitutive equations, only six of the nine variables are actually independent:

$$\frac{\nu_{xy}}{E_x} = \frac{\nu_{yx}}{E_y}, \qquad \frac{\nu_{yz}}{E_y} = \frac{\nu_{zy}}{E_z}, \qquad \frac{\nu_{xz}}{E_x} = \frac{\nu_{zx}}{E_z} \text{ or } i_{12} = i_{21},\ i_{13} = i_{31}, \text{ and } i_{23} = i_{32}$$

With six equations and nine unknowns, another set of three equations are needed. Therefore, a minimum of two sets of stress and strain are needed to solve this system of equations.

Assume two tests, Test A and Test B, are run with arbitrarily chosen strains $\{\varepsilon_{Ax}, \varepsilon_{Ay}, \varepsilon_{Az}\}$ and $\{\varepsilon_{Bx}, \varepsilon_{By}, \varepsilon_{Bz}\}$. The results from FEM analysis produce a corresponding $\{\sigma_{Ax}, \sigma_{Ay}, \sigma_{Az}\}$ and $\{\sigma_{Bx}, \sigma_{By}, \sigma_{Bz}\}$. By substituting in the orthotropic constitutive equations, the resulting six equations are (*i* is used to denote the stiffness matrix elements for simplicity):

$$\begin{aligned} \varepsilon_{Ax} &= i_{11}\sigma_{Ax} + i_{12}\sigma_{Ay} + i_{13}\sigma_{Az} & \varepsilon_{Bx} &= i_{11}\sigma_{Bx} + i_{12}\sigma_{By} + i_{13}\sigma_{Bz} \\ \varepsilon_{Ay} &= i_{12}\sigma_{Ax} + i_{22}\sigma_{Ay} + i_{23}\sigma_{Az} & \varepsilon_{By} &= i_{12}\sigma_{Bx} + i_{22}\sigma_{By} + i_{23}\sigma_{Bz} \\ \varepsilon_{Az} &= i_{13}\sigma_{Ax} + i_{23}\sigma_{Ay} + i_{33}\sigma_{Ay} & \varepsilon_{Bz} &= i_{13}\sigma_{Bx} + i_{23}\sigma_{By} + i_{33}\sigma_{Bz} \end{aligned}$$

$$\begin{aligned} \varepsilon_{Ax} &= i_{11}\sigma_{Ax} + i_{12}\sigma_{Ay} + i_{13}\sigma_{Az} \\ \varepsilon_{Ay} &= i_{21}\sigma_{Ax} + i_{22}\sigma_{Ay} + i_{23}\sigma_{Az} \\ \varepsilon_{Az} &= i_{31}\sigma_{Ax} + i_{32}\sigma_{Ay} + i_{33}\sigma_{Ay} \end{aligned}$$

Rearranging the matrices in order to solve for $\{i\}$ yields:

$$\begin{Bmatrix} \varepsilon_{Ax} \\ \varepsilon_{Ay} \\ \varepsilon_{Az} \\ \varepsilon_{Bx} \\ \varepsilon_{By} \\ \varepsilon_{Bz} \end{Bmatrix} = \begin{bmatrix} \sigma_{Ax} & 0 & 0 & \sigma_{Ay} & 0 & \sigma_{Az} \\ 0 & \sigma_{Ay} & 0 & \sigma_{Ax} & \sigma_{Az} & 0 \\ 0 & 0 & \sigma_{Az} & 0 & \sigma_{Ay} & \sigma_{Ax} \\ \sigma_{Bx} & 0 & 0 & \sigma_{By} & 0 & \sigma_{Bz} \\ 0 & \sigma_{By} & 0 & \sigma_{Bx} & \sigma_{Bz} & 0 \\ 0 & 0 & \sigma_{Bz} & 0 & \sigma_{By} & \sigma_{Bx} \end{bmatrix} \begin{Bmatrix} i_{11} \\ i_{22} \\ i_{33} \\ i_{12} \\ i_{23} \\ i_{13} \end{Bmatrix}$$

Attempts to solve for $\{i\}$ have been unsuccessful due to problems inverting $[\sigma]$. Investigation into this reveals that $[\sigma]$ has an extremely high condition number, meaning the $[\sigma]$ matrix is highly irregular in its eigenvalues.

Matrices with high condition numbers are relatively more difficult to manage in matrix algebra. Conveniently, a three-test method involves more manageable matrices.

Appendix D.3: Using a Three-Test Method

Assume three tests, Test A, Test B, and Test C, are run with arbitrarily chosen strains {ε_{Ax}, ε_{Ay}, ε_{Az}}, {ε_{Bx}, ε_{By}, ε_{Bz}}, and {ε_{Cx}, ε_{Cy}, ε_{Cz}}. The results from FEM analysis produce a corresponding {σ_{Ax}, σ_{Ay}, σ_{Az}}, {σ_{Bx}, σ_{By}, σ_{Bz}}, and {σ_{Cx}, σ_{Cy}, σ_{Cz}}. Neglecting the orthotropic constitutive equations, the resulting nine equations are (*i* is again used to denote the stiffness matrix elements for simplicity):

$$\begin{array}{lll}
\varepsilon_{Ax} = i_{11}\sigma_{Ax} + i_{12}\sigma_{Ay} + i_{13}\sigma_{Az} & \varepsilon_{Bx} = i_{11}\sigma_{Bx} + i_{12}\sigma_{By} + i_{13}\sigma_{Bz} & \varepsilon_{Cx} = i_{11}\sigma_{Cx} + i_{12}\sigma_{Cy} + i_{13}\sigma_{Cz} \\
\varepsilon_{Ay} = i_{12}\sigma_{Ax} + i_{22}\sigma_{Ay} + i_{23}\sigma_{Az} & \varepsilon_{By} = i_{12}\sigma_{Bx} + i_{22}\sigma_{By} + i_{23}\sigma_{Bz} & \varepsilon_{Cx} = i_{11}\sigma_{Cx} + i_{12}\sigma_{Cy} + i_{13}\sigma_{Cz} \\
\varepsilon_{Az} = i_{13}\sigma_{Ax} + i_{23}\sigma_{Ay} + i_{33}\sigma_{Ay} & \varepsilon_{Bz} = i_{13}\sigma_{Bx} + i_{23}\sigma_{By} + i_{33}\sigma_{Bz} & \varepsilon_{Cx} = i_{11}\sigma_{Cx} + i_{12}\sigma_{Cy} + i_{13}\sigma_{Cz}
\end{array}$$

With three sets of data, different matrix equations can be created which could not be done with only two sets:

$$\begin{Bmatrix} \varepsilon_{Ax} \\ \varepsilon_{Bx} \\ \varepsilon_{Cx} \end{Bmatrix} = \begin{bmatrix} \sigma_{Ax} & \sigma_{Ay} & \sigma_{Az} \\ \sigma_{Bx} & \sigma_{By} & \sigma_{Bz} \\ \sigma_{Cx} & \sigma_{Cy} & \sigma_{Cz} \end{bmatrix} \begin{Bmatrix} i_{11} \\ i_{12} \\ i_{13} \end{Bmatrix} \qquad \begin{Bmatrix} \varepsilon_{Ay} \\ \varepsilon_{By} \\ \varepsilon_{Cy} \end{Bmatrix} = \begin{bmatrix} \sigma_{Ax} & \sigma_{Ay} & \sigma_{Az} \\ \sigma_{Bx} & \sigma_{By} & \sigma_{Bz} \\ \sigma_{Cx} & \sigma_{Cy} & \sigma_{Cz} \end{bmatrix} \begin{Bmatrix} i_{21} \\ i_{22} \\ i_{23} \end{Bmatrix}$$

$$\begin{Bmatrix} \varepsilon_{Az} \\ \varepsilon_{Bz} \\ \varepsilon_{Cz} \end{Bmatrix} = \begin{bmatrix} \sigma_{Ax} & \sigma_{Ay} & \sigma_{Az} \\ \sigma_{Bx} & \sigma_{By} & \sigma_{Bz} \\ \sigma_{Cx} & \sigma_{Cy} & \sigma_{Cz} \end{bmatrix} \begin{Bmatrix} i_{31} \\ i_{32} \\ i_{33} \end{Bmatrix}$$

In all three cases, the [σ] is an easy and manageable 3x3 matrix. These matrices can be easily solved for the three sets of {i}. Since each i_{ij} corresponds to a term in the stiffness matrix, the individual terms for Young's Modulus and Poisson's Ratios are solved. A secondary confirmation can be performed to check if the constitutive equations: $i_{12} = i_{21}$, $i_{13} = i_{31}$, and $i_{23} = i_{32}$ still holds. For all unit cells, these equations still held.

Madenci, E. and I. Guven. *The Finite Element Method and Applications in Engineering Using ANSYS®*. New York: Springer Science+Business Media, Inc., 2006.

Boresi, A.P. and R.J. Schmidt. *Advanced Mechanics of Materials*. USA: John Wiley & Sons, Inc., 2003.

Appendix D.4: Effective Thermal Conductivity

Procedure:

In calculating the "effective thermal moduli," the unit cell of each region is assumed to have thermal conductivities in three orthogonal directions *x*, *y*, and *z*. The conduction rate equation (or Fourier's Law) can be written on in matrix form as the following:

$$\begin{Bmatrix} q_x / A_x \\ q_y / A_y \\ q_z / A_z \end{Bmatrix} = -\begin{bmatrix} k_x & 0 & 0 \\ 0 & k_y & 0 \\ 0 & 0 & k_z \end{bmatrix} \begin{Bmatrix} \Delta T_x / l_x \\ \Delta T_y / l_y \\ \Delta T_z / l_z \end{Bmatrix}$$

The thermal conductivities are defined by four unknowns in three equations. To solve for the "effective thermal moduli" of each unit cell, the geometry, temperature difference, and corresponding heat flux must be known. FEM analysis is used to determine the corresponding heat flux for a given temperature difference.

Given any unit cell, a known temperature difference (arbitrarily chosen at 100K) is applied to one set of opposing Cartesian faces. The remaining faces are kept insulated. The resulting heat on the temperature-induced faces can be divided the total unit cell face area in order to get the corresponding heat flux. The heat flux is divided by the temperature per unit length to solve for the heat conductivity in a certain Cartesian direction.

Alloy 617 is the material used to model the IHX unit cells. The isotropic heat conductivity at 800ºC is set at 25.5 W*m/K (*High Temp Metals* www.hightempmetals.com).

Findings:

Same lengths of each unit cell and corresponding effective areas.
Chosen temperature difference: 100K (1100K-1000K)

Thermal Conductivities

Heat transferred calculated from ANSYS [W]

	x-direction	*y*-direction	*z*-direction
Unit Cell A	5.181600	5.181600	5.181600
Unit Cell B	1.347378	0.8270602	0.4800920
Unit Cell C	40.49833	61.18080	33.01654
Unit Cell D	156.6633	9.062221	29.30785

Corresponding thermal conductivities: $k = q''l/\Delta T$ [W/mK]

	x-direction	*y*-direction	*z*-direction
Unit Cell A	25.5000	25.5000	25.5000
Unit Cell B	11.2277	11.8704	8.8532
Unit Cell C	11.2495	16.9947	11.6949
Unit Cell D	9.6706	11.3278	9.1587

Observation: Since Unit Cell A is a cube, there is no variation in the geometry. The resulting material properties which are solved should match the input material properties (25.50W/mK), as in this analysis. Therefore we can be confident in these results. The slight deviations are the result of the approximations and rounding uncertainties used in the FEM code.